Templated quantum dots and optimized photonic crystal cavities

by

Timothy William Saucer

A dissertation submitted in partial fulfillment
of the requirements for the degree of
Doctor of Philosophy
(Physics)
in the University of Michigan
2013

Doctoral committee:

Assistant Professor Vanessa Sih, Chair
Professor Rachel S. Goldman
Professor Roberto D. Merlin
Professor Joanna M. Millunchick
Professor Duncan G. Steel

Dedication

I dedicate this dissertation to my loving wife, April Zeoli, who has supported me through the many trials we have endured over these past six years. I also dedicate this work to our wonderful children, Ian and Simon, who have brought me incredible joy in the most turbulent times.

Acknowledgements

This dissertation represents the culmination of countless hours of labor, study, critical review, and thoughtful discussion. It has been an incredible journey toward becoming an effective researcher. I could not have completed it without the support of my colleagues, friends, and family.

I would like to thank the members of the Sih Research Group, who have made huge contributions to this work. Benjamin Norman and Christopher Trowbridge, the other two founding members of our group, helped build our laboratory. The two people I worked most closely on this project, Jieun Lee and Marta Luengo-Kovac, constructed, improved, and collected data for many of the experiments used in this work. Without their tireless efforts we could not have made so much progress in so little time.

I am gratefully indebted to my colleague and friend Andrew Martin from the Millunchick Research Group. As an expert in molecular beam epitaxial growth, he created most of the samples included in this dissertation. I cannot recount how many times he worked for days on end to grow materials, even when they had no direct impact on his own research agenda.

My committee members have given valuable advice, guidance, and critiques to this work. Professor Roberto Merlin has given advice on direction your effort and provided much needed critical feedback on our article drafts. Professor Duncan Steel gave thoughtful insight to our research agenda and provided me with personal and career advice. Professor Rachel Goldman pushed me to provide the best possible analysis and clear explanations for our data. In

doing so she made me become a much more effective researcher. Other than my advisor, Professor Joanna Millunchick was the faculty member who affected this work the most. Her keen insight in material growth has been invaluable. She forged an excellent collaboration between our research groups which has been extremely productive and mutually beneficial.

I would especially like to thank my advisor, Vanessa Sih. She has been an incredibly considerate and helpful mentor and supervisor. She encouraged me to seek new directions for our group's research trajectory and gave me the academic freedom to look beyond our known and tested methods. It is due to this approach to academia that we were able to conceive, implement, and get exciting results from an entirely new area of study. Additionally, she regularly provided guidance and suggestions for setting up and improving our experiments. She taught us to see beyond the data collection and focus on the underlying physics.

On a personal note, I would like to thank my friends and my family for their love and support in this endeavor. My closest friend and most steadfast ally, Charles Robles, has kept me grounded in the most trying times. His good humor and keen insight have been invaluable during this process. David Homyak provided advice and support during some of the most difficult times in my life. I would especially like to thank my children, Ian and Simon, for bringing joy and happiness into my life regardless of the circumstances.

Most importantly, none of this could have been possible without the continual love and support of my wonderful wife, April Zeoli. Words cannot express how indebted I am to her.

Although many people have contributed to the research and analysis in this dissertation, any errors are my responsibility alone.

Contents

List of Figures

List of Tables

List of Appendices

Abstract

One of the most exciting areas of current physics research revolves around the physical implementation of quantum computing. Proposals exist to embed quantum dots within photonic crystal cavities and couple the quantum dot states with the cavity modes. With the proper controls, it may be possible to use these systems as a basis for quantum information processing.

Semiconductor quantum dots have recently attracted a great deal of research interest. Due to their macroscopic size, researchers can optically access individual dots and observe their nonclassical nature. However the applicability of quantum dots can be limited by their random size and placement using typical growth techniques. In our work we demonstrate our ability to control the spatial positioning of InAs/GaAs quantum dots though an *in vacuo* fabrication procedure. By characterizing their growth and optical properties, we demonstrate our ability to create optically active quantum dots and to achieve 100% site placement fidelity.

Photonic crystal cavities are novel devices which enable us to tailor the optical response of a material. Improving the quality of these cavity designs can strongly influence our ability to couple them to embedded emitters, such as quantum dots. Optimizing the cavity configuration is a problem involving many variables which cannot be fully explored using traditional techniques. We employ a nature inspired search algorithm to discover novel cavity arrangements that exceed existing methods.

Establishing the coupling efficiency between a quantum dot and the photonic crystal cavity surrounding it is an important step to using these as a platform for further investigations. A variety of techniques exist to demonstrate this property, each with its advantages. We explore the method of luminescence intensity autocorrelation to determine the exciton lifetime of a single quantum dot and the influence of its cavity coupling. We demonstrate this method in the Purcell regime and find the Purcell factor for a weakly coupled quantum dot.

Chapter 1

Introduction

Realizing the physical implementation of a quantum computer or quantum information processing platform is the current goal of many research agendas. The ability to access new algorithms and methods of data processing may usher in a new era in scientific discovery and industrial innovation. Work has been limited by the need to have macroscopic access to single quantum states and controlled interactions between states. The most developed systems for these studies lack the necessary scalability that practical implementation requires.

A semiconductor quantum dot (QD) is a novel heterostructure composed of two dissimilar semiconductors. Due to differences in their properties they can be suitably arranged to create quantum confinement in all spatial dimensions. This leads to discrete, atom-like states in a macroscopic object. Proposals exist to use the state of a single electron inside a quantum dot as the basis for quantum computing. This is an excellent combination of well defined quantum state (such as the spin of the electron) and larger dimensions. Additionally, quantum dots are an extremely scalable system. Once a system has been developed using a few QDs, we can then expand the application to include hundreds or thousands of dots.

One of the other criteria for building a quantum computer is the need to create interactions between two different quantum states. Using two quantum dots embedded within

an optical cavity, we may be able to perform such an operation by using the cavity mode to mediate the interaction. Rather than using traditional optical devices, photonic crystal cavities have been a preferred medium.

A photonic crystal cavity is a metamaterial with unusual optical properties. By periodically varying the media used, we can change the optical density of states for the overall structure. This allows us to make mirrors, waveguides, and cavities in a material that would be otherwise transparent. We can tailor their optical properties by varying the amounts of materials used and their arrangement.

Embedding quantum dots inside photonic crystal cavities does not guarantee their successful interaction. The coupling between the two elements must be established. The strength of the interaction between the two can rely on a variety of factors, some of which cannot be controlled after the sample has been created. A careful study of the quantum dot–cavity interaction is necessary to verify the usefulness of this device for further studies.

1.1 Spatially controlled quantum dots

Quantum dots have a myriad of applications. They have been used in diverse fields such as imaging in live cells [76], solar cell improvements [50], and near field imaging [29]. The optical and electronic properties of the QDs influence their applicability in various systems. In Chapter 2, we discuss various heterostructure types and a brief introduction to their associated quantum mechanics.

Semiconductor QDs are typically grown using the epitaxial methods discussed in Chapter 3. In a typical growth, the dots form at random locations and with a wide range of dimensions. Details on how these dots typically are grown are given in Section 3.1. For some applications, we desire to predetermine the position of the QDs. This cannot be accomplished with usual methods. Instead we turn to a patterning process. We modify the growth

surface of the QDs. In doing so, we create sites where QDs prefer to form. In Section 3.2 we give details and show results from our patterning techniques. In Section 3.3, we study our spatial control for differing growth conditions, and in Section 3.4 we show optical studies of our quantum dots.

1.2 Photonic crystal cavity designs

Photonic crystals are marvelous devices. From their inception in 1987 [33, 77], they have been used widely in practical applications [64] and fundamental research [32]. To gain insight into how their unique properties arise, we first review the theory associated with their operation in Chapter 4. In Section 4.1 we review the affects of applying periodic material parameters into Maxwell's Equations. Then, we discuss their effects in one, two, and three dimensions in Sections 4.2, 4.3, and 4.4, respectively. We also discuss the idea of scale invariance as it applies to photonic crystals in Section 4.5.

For our application, we are most interested in planar photonic crystal cavities, which are described in Chapter 5. We consider the two main types of cavity configurations used and analyze their properties. In Section 5.1, we discuss hexagonal cavities, and in Section 5.2, we explore linear cavities. We then show how these cavities have been optimized in Section 5.3.

In Chapter 6, we seek to improve our cavity optimization. However this problem cannot currently be solved using traditional optimization methods. In Section 6.1 we describe a nature inspired algorithm that we employ to enhance our cavity response. We discuss details of the simulations needed to characterize our cavities in Section 6.2 and we give our final results in Section 6.3. The outcome is an unusual, non-intuitive design. We give our physical interpretation of how it works in Section 6.4.

1.3 Coupling quantum dots and photonic crystal cavities

Demonstrating the coupling between a quantum dot and its surrounding photonic crystal can be challenging. Coupling can be indicated through demonstration of photoluminescence anti-crossing between the cavity and the dot [78] or through changes to the quantum dot's autocorrelation [19]. Directly probing the exciton dynamics gives an excellent measure of the coupling; however, the necessary equipment is not always available[28]. Instead, we use luminescence intensity autocorrelation which enables us to probe the exciton lifetime similar to time resolved photoluminescence and observe cavity effects.

Chapter 7 discusses our approach to measuring the cavity, dots, and the interaction of the two. As an independent measure of the cavity quality, we use the methods described in Section 7.1. Then, in Section 7.2 we discuss our new method and demonstrate cavity coupling in our samples.

Chapter 2

Semiconductor Heterostructures

One of the simplest examples of quantum mechanics producing nonclassical results is that of the finite square well in one dimension. In one dimension if there exists some region of potential lower than the surrounding region, we find unique solutions to Schrödinger's equation. At energies below the difference between the two potential levels, discrete states exist [26].

2.1 Finite potential wells

Suppose we have a finite potential well as shown in Figure 2.1. We consider three regions to which we apply Schrödinger's equation. On the left the potential is at some V_0 to which we have a solution ψ_{left}. In the center, the potential is zero so our solution, ψ_{ctr} consists of just

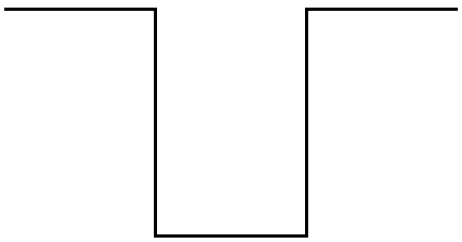

$$V(x) = \begin{cases} 0 & |x| < L/2 \\ V_0 & \text{otherwise} \end{cases} \tag{2.1}$$

Figure 2.1: Potential diagram for a one dimensional finite square well.

sine and cosine functions. On the right we have a similar situation to the left with solutions ψ_{right}.

$$-\frac{\hbar^2}{2m}\frac{\partial^2}{\partial x^2}\psi_{\text{left}} = (E - V_0)\,\psi_{\text{left}} \qquad -\frac{\hbar^2}{2m}\frac{\partial^2}{\partial x^2}\psi_{\text{right}} = (E - V_0)\,\psi_{\text{right}} \tag{2.2}$$

We only concern our analysis for the bound states in which $E < V_0$. These fit the form $e^{\pm\alpha x}$. Considering boundary conditions as x goes to $\pm\infty$ we have one possible solution for each region.

$$\psi_{\text{right}} = Ce^{-\alpha x} \qquad \psi_{\text{left}} = De^{\alpha x} \qquad \alpha = \frac{\sqrt{2m(V_0 - E)}}{\hbar} \tag{2.3}$$

$$\psi_{\text{ctr}} = A\sin(kx) + B\cos(kx) \qquad k = \frac{\sqrt{2mE}}{\hbar} \tag{2.4}$$

If we apply our boundary conditions at $x = \pm L/2$ that ψ and $\partial\psi/\partial x$ must both be continuous we arrive at two possible combinations of these equations. Either $A = 0$ and $C = D$ (the symmetric case) or $B = 0$ and $C = -D$ (the anti-symmetric case). With suitable combinations of the boundary conditions we arrive at a relationship between α and k.

$$\alpha_{\text{sym}} = k\tan\left(\frac{kL}{2}\right) \qquad \alpha_{\text{anti}} = -k\cot\left(\frac{kL}{2}\right) \tag{2.5}$$

Going back to our definitions of α and k we realize they both depend on the energy. Instead we shift to the dimensionless units $u = \alpha L/2$ and $v = kL/2$. We also define $u_0 = mL^2V_0/2\hbar^2$. Making the proper substitutions into our definitions of α and k we find the relationship $u^2 = u_0^2 - v^2$.

$$\sqrt{u_0^2 - v^2} = \begin{cases} v\tan v & \text{(symmetric)} \\ -v\cot v & \text{(anti-symmetric)} \end{cases} \tag{2.6}$$

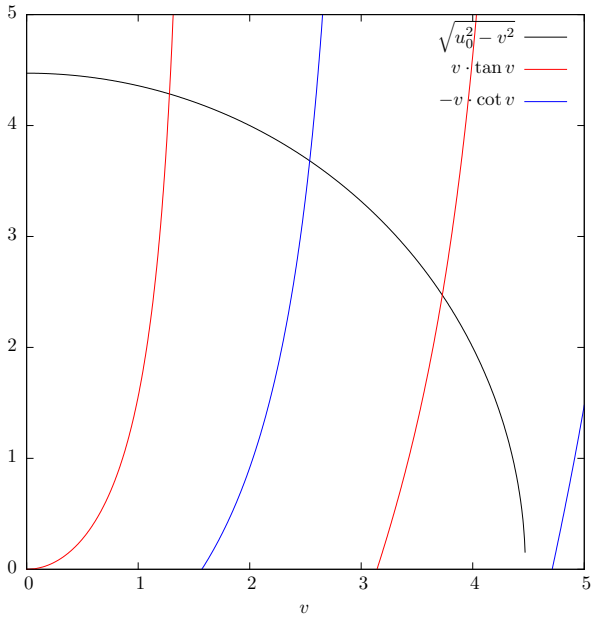

Figure 2.2: Origins of the discrete solutions to the finite potential well show up as solutions to the transcendental Equation 2.6.

The variable u_0 gives us a dimensionless relationship between the quantum well's width and height. To perform any further analysis we must assume a value. Here we pick $u_0^2 = 20$. We see that these are transcendental equations. As such they will only have discrete solutions. This is important because this is what gives us quantized behavior of a finite potential well at energies lower than the well depth.

Solutions to the transcendental equations can be found either numerically or using approximation methods [4]. For this choice of u_0^2 we have $v_1 = 1.28$, $v_2 = 2.54$, and $v_3 = 3.73$. No other solutions exist. We also see from our previous definition of k and v that we can relate the energy of the wave function to this result.

$$E_n = \frac{2\hbar^2 v_n^2}{mL^2} \tag{2.7}$$

We find that the energy of the solutions scales as $1/L^2$. Thinner wells lead to higher energy states due to greater confinement. Deeper wells do not affect the energy of the states,

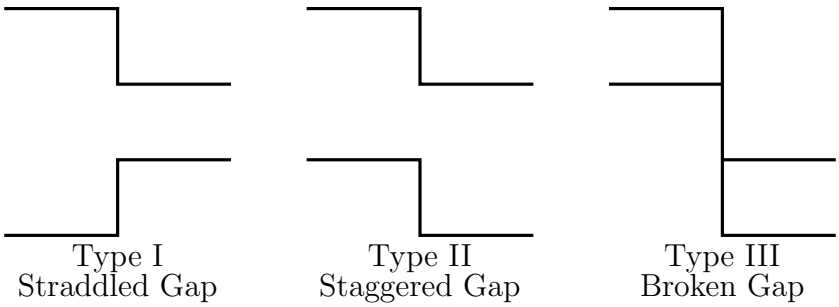

Figure 2.3: Types of band offsets at the interface between two semiconductors.

but they do affect the number of discrete states that can exist. These are extremely useful results and we will see them appear experimentally in Chapter 3.

2.2 Heterostructures as finite potential wells

The simple finite potential well system provides analytic solutions. However its usefulness is limited since such ideal systems do not typically exist in nature. Instead we must engineer a system using available materials for study. One such way is by creating heterostructures – combinations of dissimilar materials, such as a stack of layered Indium Arsenide (InAs) and Gallium Arsenide (GaAs).

For semiconductors we can define their energy levels according to a few basic parameters. Each material has a conduction band and valence band, with energy E_C and E_V respectively. When one material is adjacent to another the order in which the conduction and valence bands line up can fall into one of the three types shown in Figure 2.3. Each of these band alignments can serve different purposes. For our work, we are more interested in Type I band alignment. Here the second material has a higher valence band and lower conduction band than the first material. In such cases, electrons in the conduction band will tend to "fall into" the lower potential of the second material. Correspondingly, any holes in the material will move into the higher potential of the same material. Thus the electron-hole pairs can become trapped in one material. If we sandwich the smaller gap material on both sides with

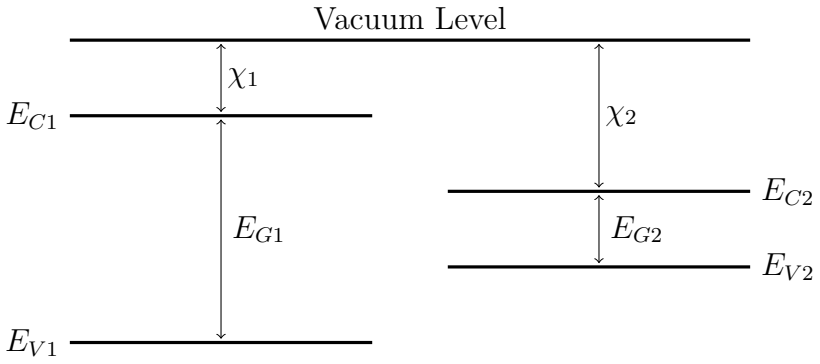

Figure 2.4: This diagram represents the energy levels and material parameters at the interface of two materials. E_C and E_V are the conduction and valence band levels. χ is the electron affinity and E_G is the material band gap.

Material	χ	E_G	E_C	E_V
InAs	4.9	0.35	-4.9	-5.25
GaAs	4.07	1.42	-4.07	-5.49
AlAs	3.5	2.17	-3.5	-5.67

Table 2.1: Band properties for various materials. All values are listed in eV.

the larger gap material, we can create finite potential wells in one dimension.

To determine what types of band alignment two materials will have, we turn to the material parameters shown in Figure 2.4. For each material the conduction band lies some energy χ, known as the electron affinity, away from the vacuum level. The difference between the conduction and valence bands is the band gap of the material, E_G. Knowing the electron affinity and band gap for any two materials we can often determine their band alignment using Anderson's Rule [3]. For InAs embedded within GaAs we form a Type I band alignment, suitable for creating a potential well for both electrons and holes[9].

2.3 Quantum wells and wires

By creating a structure that contains a thin plane of InAs embedded within GaAs or GaAs within AlAs, we will form a finite potential well in the direction perpendicular to the plane.

However in the plane of the InAs we have no such confinement. An electron inside the InAs would have a continuum of possible energy levels it could inhabit. If we decompose the electron's wave function into a combination of the wave function in the plane (x and y directions) and the wave function out of plane (z direction) then the possible energy levels would be a combination of the continuum solutions and the discrete solutions [27]. This structure is referred to as a quantum well.

$$\Psi(x, y, z) = \Phi(x, y) \cdot \psi(z) \qquad E_{\text{total}} = E_{x,y} + E_z \tag{2.8}$$

If the quantum well is sufficiently thin, then the electrons will be mostly confined to two dimensional motion. This two dimensional limitation leads to a modified electron density of states which has distinct steps rather than a smooth square root curve [80]. This leads to these materials performing better in applications such as diode lasers and infrared sensors.

If we take a quantum well and etch away most of the low potential material along a line, we can form a structure known as a quantum wire. Here we have confinement in two dimensions. Since there is only one direction in which the electrons can travel, the density of states for these materials more closely represents delta functions [80]. This greater confinement can lead to further improved optical performance [36].

2.4 Quantum dots

If we can form material that is confined in all three dimensions we form a quantum dot. These structures are unique from those previously described since their confinement in all spatial dimensions leads to discrete energy levels. This means we have unique solutions to Schrödinger's equation, just as atoms have unique solutions. For this reason quantum dots are sometimes referred to as "artificial atoms." This is particularly useful since we can create

a macroscopic object ($10^4 - 10^5$ atoms) that has atom-like behavior.

Quantum dot growth is discussed in Section 3.1. Based on the growth mechanism we use, the dots typically form discs with heights 5–20 nm and diameters of approximately 40–100 nm. If we consider the solutions to this problem to be separable as in Section 2.3, then we can consider it as a 1D finite potential well in one direction (z) and a 2D finite well in the perpendicular direction (x and y). Since the thickness of the dot is much smaller than the diameter, we expect the energy levels due z direction confinement to be much greater than the in x and y direction. At low energy, we can expect electrons to lie in the lowest possible z energy. This leaves us with a circular finite potential well, which has simple harmonic oscillator solutions [10].

These properties of quantum dots have led researchers to study their potential application in quantum computing. Some of the criteria necessary for a practical implementation of a quantum computer is that we have well defined, accessible quantum states [18]. Since QDs are relatively large in dimension we can access a single dot optically. The discretized nature of the electron wave function gives us a clearly defined quantum state that we can manipulate to form our quantum bit of information.

Chapter 3

Site controlled quantum dots

Quantum dots present exciting new opportunities both for pure scientific interest and practical applications [11]. Industrial applications include low threshold lasers [41], higher sensitivity detectors [74], and improved solar cell efficiency [16, 47, 50]. They have also advanced physics research by providing single photon sources [14] and may serve as a platform for quantum information processing [22]. For our interests, one of the main limitations of semiconductor QDs is that they tend to nucleate at random positions during growth. Our work seeks to refine growth techniques to enable placement of a single QD at a predefined location and to suppress dot formation elsewhere.

3.1 Epitaxial growth

From Chapter 2, we find that quantum dots can be created by surrounding one material with another. To do this we wish to have dimensions sufficiently small to have confinement effects but large enough for optical access. For InAs embedded within GaAs, the most common method of creating these dots is molecular beam epitaxy (MBE).

In a MBE chamber, we can control the growth of our materials, often down to the level

of a single layer of adatoms [25]. During the deposition process, one of three growth modes is typically present. If the adatom-adatom interaction is stronger than the adatom-surface interaction, then the deposited material will tend to form 3 dimensional islands or clumps. This process is known as Volmer-Weber growth [54]. At the other extreme is Frank-van der Merwe growth, in which the adatom-surface interaction is strongest. In this type growth we have smooth layering [54]. The intermediate regime is Stranski-Krastanov (S.K.) growth. In S.K. growth the deposited layer initially forms a layer as with the Frank-van der Merwe growth. After some critical thickness, the deposited layer transitions to island structures [59, 57]. The critical thickness depends on many factors, such as the materials' lattice parameters and surface energies.

We consider S.K. growth in terms of the strain on the deposited layer [52, 55]. For small amounts of material, the strain due to the atom mismatch is small. As the layer thickness is increased, the strain energy accumulates. After the critical thickness, the cumulative strain causes the adatom-surface interaction to be weaker than that of the adatom-adatom. It will be energetically favorable at this point to form islands instead of smooth layers. InAs and GaAs are zinc blende semiconductors with lattice parameters 0.606 nm and 0.565 nm, respectively. This lattice mismatch creates the in-plane strain necessary for the S.K. growth.

An interesting phenomena occurs when there are local regions of curvature on substrate. Deformations in the starting surface of the growth influence the strain on the wetting layer. These regions will have a lower effective critical thickness due to the added strain. Islands may preferentially form at these sites of additional strain. This has been demonstrated by deforming the substrates with lasers, electron beam lithography, and focused ion beam patterning [5, 69, 70, 45].

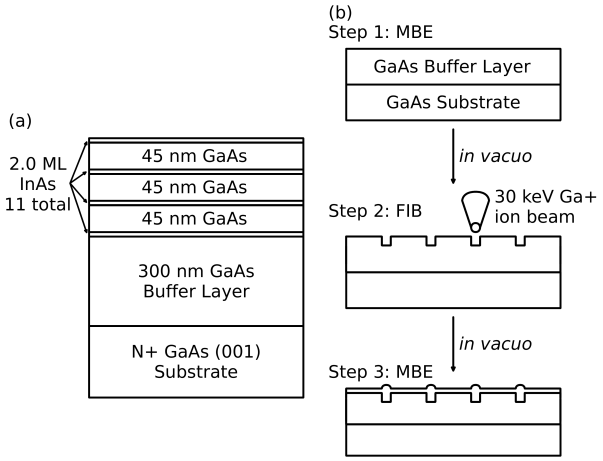

Figure 3.1: FIB induced QD nucleation schematic.

3.2 Focused ion beam induced dot nucleation

One significant disadvantage with S.K. grown quantum dots is the lack of control over the dot placement and size. While some methods have been used to create uniformly sized dots [39, 73], they still suffer from lack of spatial control. Many approaches to deterministic dot placement have been used [5, 45, 69]. One such method is to use a focused ion beam (FIB) to induce dot nucleation at predetermined coordinates. We do this by growing a sample in such a manner that QDs will not typically form. Then we create nucleation sites using the FIB.

We grow the sample below the critical thickness for dot formation. In this regime there is insufficient stress in the layer of InAs to form quantum dots. We then induce additional stress at predetermined locations by changing the surface topology. By using a FIB we can mill circular holes in the GaAs substrate to create QD nucleation sites [45, 67, 48].

Figure 3.1 shows the method we use to form our quantum dots [67]. Beginning with a GaAs substrate we grow 300 nm of GaAs at $T_{\text{sub}} = 590°C$, $R_{\text{Ga}} = 1.01\text{ML/s}$, and $R_{\text{As}} = 2.8\text{ML/s}$. In these conditions, we have As overpressure, so the rate of growth of GaAs is determined by the Ga deposition rate, R_{Ga}. The sample is transferred *in vacuo* to the FIB

where it is irradiated with a 9.2pA, 30 keV Ga+ ion beam. The FIB was allowed to dwell on each site for either 1 or 3 ms. We created square arrays $40\mu\text{m} \times 40\mu\text{m}$ large with pattern spacing of $0.25, 0.5, 1.0,$ or 2.0 μm. The samples were moved back *in vacuo* to the MBE growth chamber. There, 2.0 ML of InAs was deposited and covered with 45 nm of GaAs at $T_{\text{sub}} = 485°C$, $R_{\text{Ga}} = 1.0$ML/s, $R_{\text{In}} = 0.11$ML/s, and $R_{\text{As}} = 2.7$ML/s. All substrate temperatures were measured by optical pyrometer. This was repeated for 11 total layers of InAs with the last layer uncapped [67]. These samples were grown by Andrew Martin.

To determine the optical quality of our quantum dots, we performed photoluminescence measurements. The sample was cooled to 10 K and irradiated with a 633 nm Helium-Neon laser operating at $7.5\mu W$. Using an infinity corrected 100X microscope objective, the laser spot was focused onto a spot with approximately 30μm diameter. To further increase our signal to noise ratio we collected data through the same objective using a confocal microscope setup [58]. Data was collected from a region approximately 20μm in diameter as measured by imaging and comparing to a calibration sample. Data was detected with a 0.75 m spectrometer using a 150 G/mm reflection grating and single channel, liquid nitrogen cooled InGaAs detector. PL data from these samples were collected by Andrew Martin and myself.

In Figure 3.2, we see the photoluminescence from the eight regions of our sample irradiated by the FIB. Also shown is a representative sample of the luminescence from a region that was not FIB patterned. We see three distinct peaks located at 1.24, 1.38, and 1.50 eV. The 1.50 eV peak is well established as the bulk GaAs emission [23]. This comes from both the substrate and the 45 nm of GaAs between the InAs layers. We attribute the 1.38 eV peak to the thin layer of InAs that remains after the quantum dots have formed [51]. This is referred to as the "wetting layer." The 1.24 eV peak is from the quantum dots. We expect the wetting layer to have a higher energy than the QD peak because it has greater confinement. This is due to the wetting layer thickness of about two monolayers (1.2 nm),

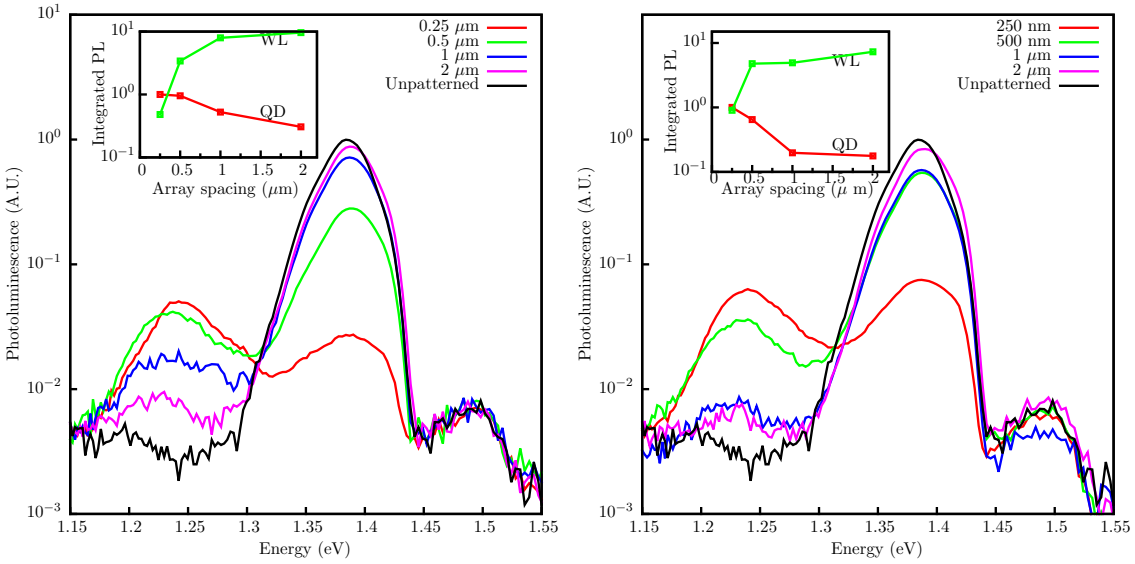

Figure 3.2: Photoluminescence measurements of site controlled QD arrays for 1ms (left) and 3ms (right) dwell times and various pattern spacings. The inset shows the integrated PL peaks for the QD and wetting layer. A representative region of the sample without FIB irradiation is shown in black. Data was taken at 30 K.

whereas the quantum dots are often 10 nm thick [45]. A smaller feature size leads to greater confinement and higher energy, as shown in Chapter 2.

The unpatterned area of the sample shows no emission at 1.24 eV. This is important since it verifies that we are growing below the critical thickness for dot formation. It is also evident that we have modified this material's optical properties with sub micron spatial control.

The QD emission shows the general trend that as the pattern spacing increases the luminescence decreases. This can be mostly attributed to the number of dots formed. For each region we have the same collection area. However, larger pattern spacings have fewer FIB sites. Additionally since smaller FIB spacings lead to a greater QD density, less InAs remains for wetting layer formation. We would thus expect the wetting layer emission to decrease as the QD density increases. We see this trend in Figure 3.2.

To further study the quantum dots we measured the temperature dependence of the QD photoluminescence, shown in Figure 3.3. The 0.25 μm pattern spacing with 1 ms FIB dwell

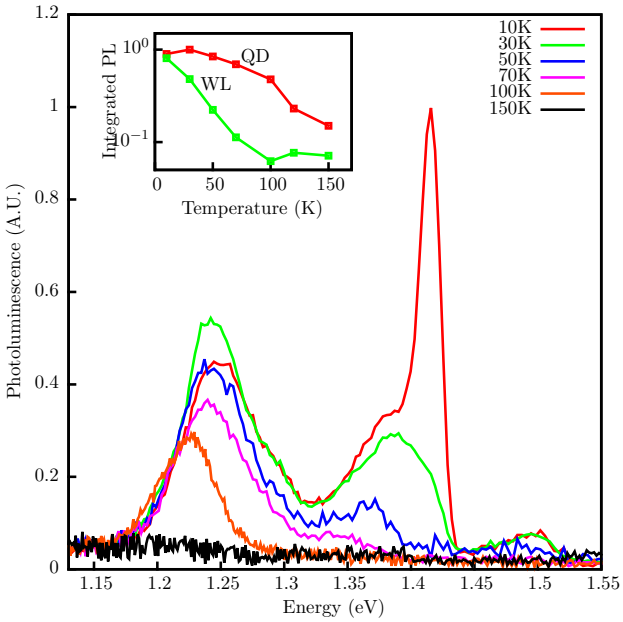

Figure 3.3: Temperature dependence of the photoluminescence for the 0.25 μm pattern spacing, 1 ms dwell time region.

time sample was chosen due to its bright QD peak and narrow line width [67]. The inset shows the integrated PL intensity from the quantum dots and wetting layer as a function of temperature.The wetting layer signal drops much more rapidly than does the QD signal. Dots have discrete densities of states due to their confinement in all 3 dimensions. The wetting layer has a continuum of states in two dimensions, so non radiative recombination (thermal quenching) becomes significant at lower temperatures [40].

From this study, we conclusively showed our ability to engineer quantum dot energies and formation. The ability to spatially control the formation of QDs can lead to new sensor designs and other industrial applications. For most physics research involving QDs, we are also concerned with the placement accuracy of our technique. For this we conducted a series of sample growths and characterizations using imaging techniques and optical studies.

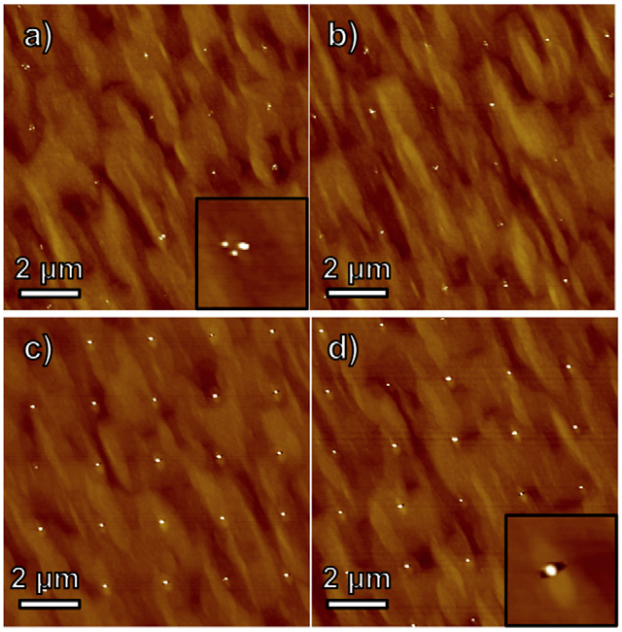

Figure 3.4: AFM images of the surface of the 6^{th} layer of InAs. All regions are patterned with a FIB spacing of 2 μm. Images are for (a) 1, (b) 3, (c) 6, and (d) 9 ms FIB dwell times.

3.3 Spatial control

3.3.1 Many layer samples

Having demonstrated we can form quantum dots with certain regions and suppress it elsewhere we sought to study and improve our QD spatial placement. Andrew Martin and I grew a series of samples with 6 and 26 layers of InAs. This allowed us to study two regimes of dot growth – near the FIB milled holes and after many layers where the pattern may become lost due to planarization [48]. These samples were grown similar to those in Section 3.2 with a few changes. The GaAs thickness between adjacent layers of InAs was decreased to 20 nm for the 6 layer sample and 18 nm for the 26 layer sample. By changing to thinner layers of GaAs we expect more pronounced effects of the dot stacking. The FIB dwell times were extended to include 6 and 9 ms.

In Figure 3.4 we see the Atomic Force Microscopy (AFM) images for the 2 μm pattern

spacing at each dwell time for the 6 layer sample collected by Andrew Martin. The insets are magnified images of a single site showing either single or multiple dot formation. We see in these images that we have excellent pattern retention, particularly for the longer dwell times. In Figure 3.5 we report the statistics for QD dimensions and placement fidelity as a function of dwell time. As the ion dose increases we see the QD and hole diameters increase. This is as we should expect since longer FIB irradiation will consume more of the substrate, leading to larger holes. Larger holes should fill in with more InAs leading to larger QD diameters. As the dwell time increases, we see the hole depth increasing (shown as a negative height above the surface) and the QD height increasing. These are consistent with the overall dot size changes.

We define the fidelity as the ratio of the number of sites which contain a QD to the total number of sites in the sample. For single QD formation, we find that the longer dwell times are significantly better at single dot formation, reaching 100% fidelity at 6 and 9 ms FIB dwell times. We expect that large ion doses lead to very steep hole edges. As layers of InAs and GaAs are added to the sample, it begins to become planarized and the holes are filled in. Those with deeper and steeper holes are less likely to fill in completely [45]. This can be seen in the inset images in Figure 3.4. Less planarization should lead to more likely dot formation [45].

In Figure 3.6 we show AFM images of the 9 ms dwell time for various pattern spacings and analysis of the QD dimensions. In the magnified inset images, we see the FIB hole remains apparent regardless of the pattern spacing. As the pattern spacing increases, the QD diameter increases linearly until 1 μm spacing. Then it remains constant. Also, the height increases nearly linearly with pattern spacing up to the 1 μm spacing. We believe the constant dimensions after 1 μm occur because the QD has used all of the InAs available to it. The wetting layer material is used to form the QDs, and it is only 2 monolayers thick. There must exist some distance between FIB sites where the material available to the QD

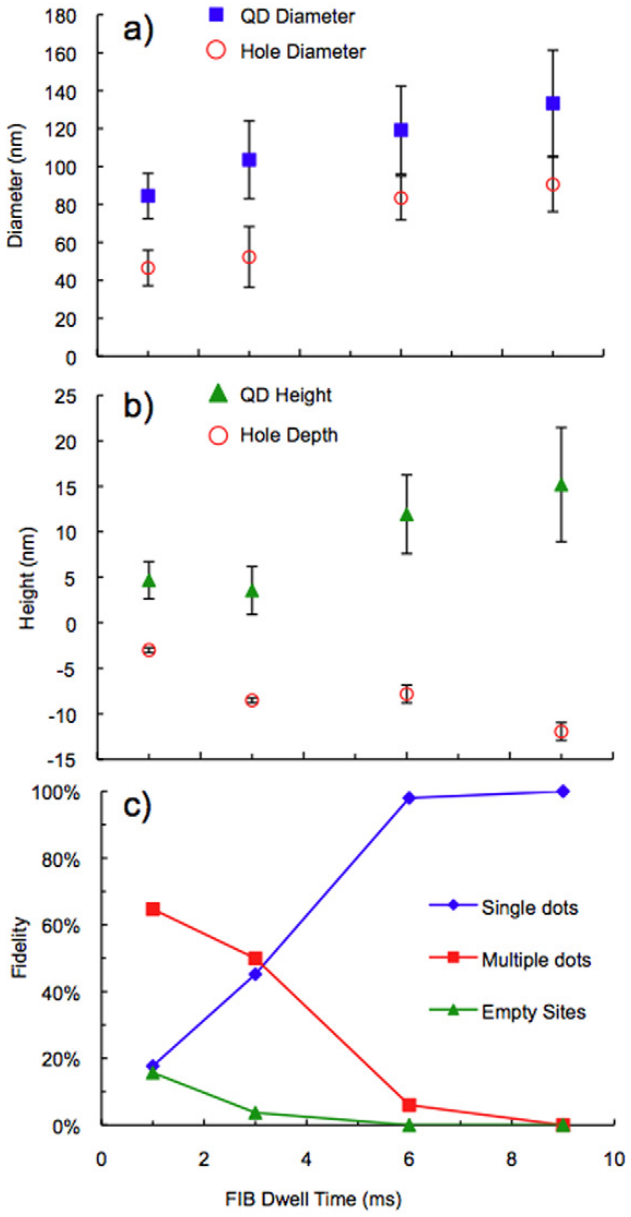

Figure 3.5: Plots of QD and FIB hole (a) diameter, (b) height/depth, and (c) fidelity for various FIB well times All data are taken for a 2 μm FIB pattern spacing based on AFM from the uncapped 6^{th} InAs layer.

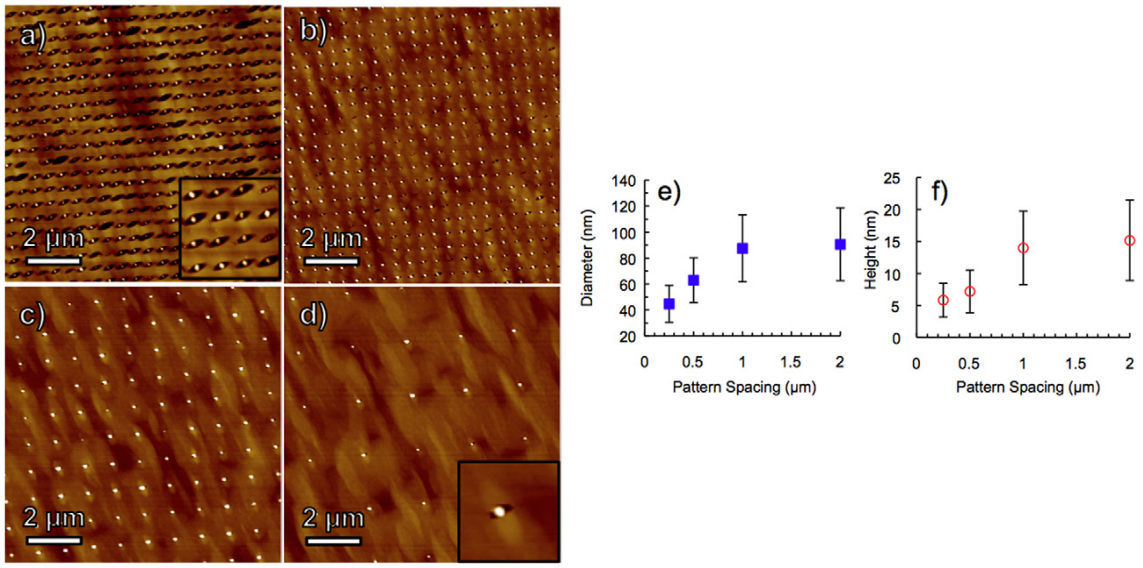

Figure 3.6: AFM images of the uncapped 6th layer of InAs QDs. Pattern spacings are (a) 0.25, (b) 0.5, (c) 1, and (d) 2 μm. QD (e) diameter and (f) height for each spacing. All data are for 9 ms FIB dwell times.

formation no longer interferes with the adjacent sites [48]. This may be varied by increasing the substrate temperature to increase the atom diffusion length [49]. Beyond this distance the effects of our process at each site is independent of the other sites. In general, we should be able to extend the distance between sites further without changing the QD dimensions.

Analyzing the 26 layer sample shows significant differences from those shown for the 6 layer sample. Here, we have grown so much material on top of our patterned substrate that the FIB holes are completely filled in. In Figure 3.7 we see AFM images and statistical data for the 9 ms FIB dwell time at various pattern spacings. The differences between the 26 layer sample and the previous 6 layer sample are striking. For the closer spacings of 0.25 and 0.5 μm the FIB pattern is completely lost. However the 1 and 2 μm samples still show pattern remnants.

In the 26 layer sample, the large pattern spacings have now formed mounds elongated along the GaAs fast diffusion direction, [1$\bar{1}$0] [48]. They are approximately 800–1000 nm long and about half as wide. As can be seen in the insets images in Figure 3.7, the QDs

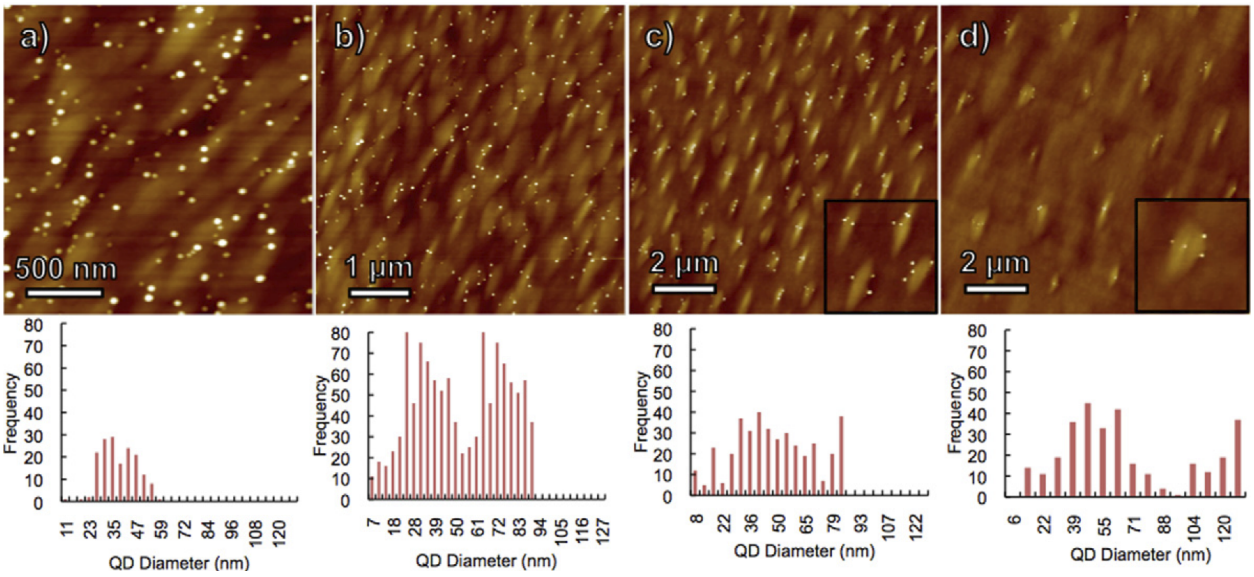

Figure 3.7: AFM images of the 26$^{\text{th}}$ layer of InAs QDs for 9 ms FIB dwell times at pattern spacings of (a) 0.25, (b) 0.5, (c) 1.0, and (d) 2.0 μm. In (c) and (d) the inset shows a higher magnification image to clearly see dot formation on the mound edges.

tend to form on the edges and very top of these mounds. These are the regions where the surface of the material is changing the most rapidly, which could increase the local stress on the InAs layer [48]. This additional strain, much like the surface deformation from the FIB hole, provides a nucleation site for the QDs. However we find that the QDs are no longer placed at FIB sites. Rather, they are located on the mound edges which may move them spatially by up to 1 μm.

Since the mound formation reproduces the underlying FIB patterning, we believe this is a deterministic effect [48]. We know the FIB pattern is retained at the 6 layer sample for these long dwell times. As layers of InAs and GaAs are placed on the sample, mounding begins to occur due to the starting surface deformation [37]. As the layers build up, the effects accumulate until mounds form. This might have potential applications in devices where we need to create many QDs yet still have reasonable spatial control.

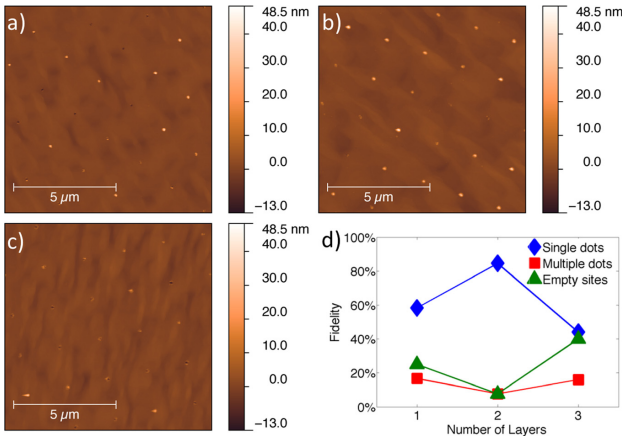

Figure 3.8: AFM images from samples with (a) 1, (b) 2, and (c) 3 layers of InAs. (d) QD fidelity as a function of of number of layers of InAs. FIB pattern spacing is 2 μm and dwell time is 3 ms.

3.3.2 1, 2, and 3 layer samples

We were also interested in the process of growing only a few layers and how the sample morphology changes as new layers are added. Andrew Martin and I grew a series of three samples with one, two, and three layers of InAs. The growth parameters were the same as in Section 3.1 with the following exceptions. The FIB operated at 10 pA and had dwell times of 1, 3, 6, and 9 ms. The spacing between the layers of InAs was decreased from 45 nm to 10 nm to get better QD stacking [46]. Pattern spacing of 1 and 2 μm were used. In Figure 3.8 we show AFM images from the 3 layer samples for the 2 μm pattern spacing and 3 ms dwell time as collected by Marta Luengo-Kovac.

We are interested in the stacking fidelity of this procession, in which a perfect sample would then have a fidelity of placing a single QD as 100% [46]. In Figure 3.8 we show the our fidelity statistics for these three regions as a function of the number of layers of InAs. We find that these regions show the best single dot fidelity for 2 layers. As the third layer is added we begin to form more multiple dots, decreasing the single dot fidelity.

Encouraged by these results we sought to explore the other parameters of interest – the FIB dwell time and pattern spacing. In Figure 3.9 we show the fidelity for all of these regions.

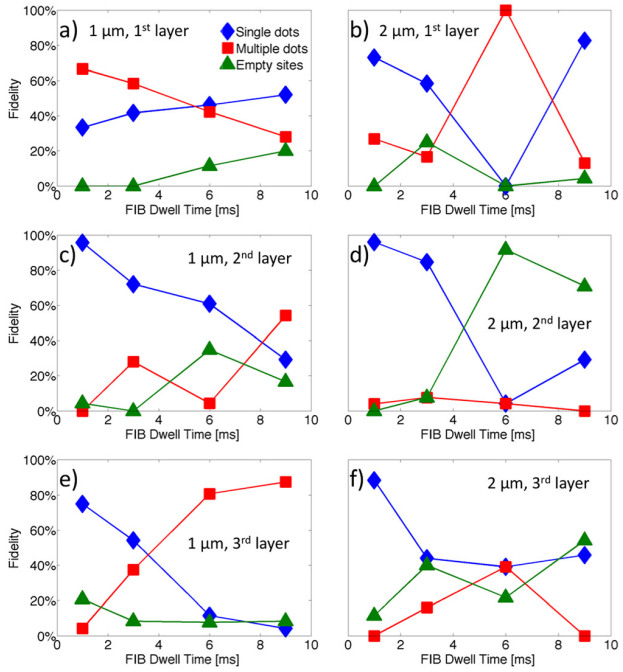

Figure 3.9: Fidelity as a function of FIB dwell times. Plots are labelled with pattern spacing (1 or 2 μm) and layers of InAs (1, 2, or 3).

Each plot is labelled with the pattern spacing (1 or 2 μm) and number of layers of InAs. It is clearly evident that the best single dot fidelities occur for the lower FIB doses. The single layer sample is an exception. We expect that the surface of the sample was damaged by the FIB leading to poor dot formation [45]. As is usual with these systems, we expect the single layer samples to have poor optical quality, so we neglect these regions henceforth [69].

Achieving the best fidelity by using low dwell times seems a sharp contrast to the results shown for the 6 and 26 layer samples in Section 3.3.1. There, we found large ion doses led to the best fidelities. If we want to keep pattern retention after a large amount of material is placed on our substrate, we will need larger surface deformations to begin with. However for these few layer samples with very thin layers of GaAs we are not working in that regime. Here, smaller doses are sufficient to nucleate QDs. The final application of the sample should dictate which regime is best to operate in. For studies of individual QDs it may be best to work with only two or three QD layers to best isolate the layer of interest. For applications

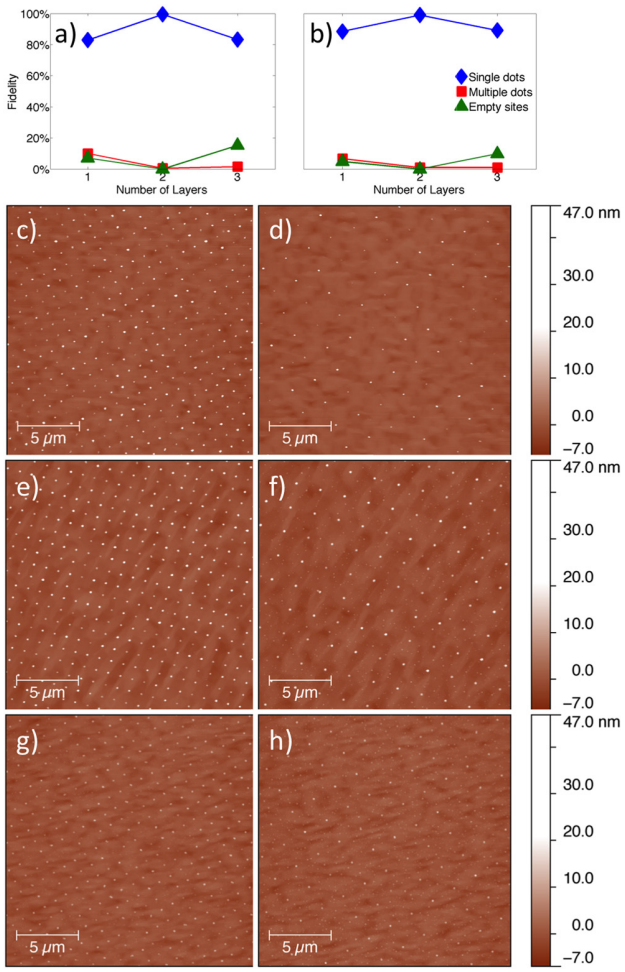

Figure 3.10: Fidelity plots as a function of the number of InAS layers and the associated large area AFM images. (a), (c), (e), and (g) are for 1 μm pattern spacing while (b), (d), (f), and (h) are for 2 μm spacing. (c-d), (e-f), (g-h) correspond to 1, 2, and 3 layers of InAs respectively.

such as quantum cascade lasers we may prefer higher QD densities, suggesting longer FIB dwell times and many layers as preferable.

Having determined that the low FIB doses lead to better single dot fidelity for these samples, we performed larger scale measurements of the 1 ms dwell time samples. By measuring an area $20\mu\text{m} \times 20\mu\text{m}$ we were able to collect statistics for 400 FIB sites for the 1 μm spacing and 100 sites for the 2 μm spacing. Figure 3.10 shows the AFM images of these surfaces as well as their fidelity statistics. The trend follows that of Figure 3.8 as we would expect. What is perhaps most interesting is that for both pattern spacings we achieve 100%

single dot fidelity of single dots for the second InAs layer [46].

It is remarkable that the distance between the FIB sites plays no effect on the QD placement. This has huge implications for device manufacturing and incorporating QDs in further research. One difficulty in accessing or addressing a single dot is due to the high areal QD density in many samples [44]. Using the FIB induced nucleation method, researchers may be able predetermine specific sites for QD nucleation many microns away from one another leading to compete optical isolation. Additionally this method allows us to create extremely uniform arrays of dots for later integration into devices such as photonic crystals.

3.4 Optical studies

3.4.1 Macro photoluminescence of QD arrays

Having established our ability to place QDs at predetermined coordinates, the next step was to determine their optical quality. Since our overarching research agenda is to integrate QDs into devices, their energy levels need to be well established. The six layer sample from Section 3.3.1 had promising spatial control. We performed photoluminescence measurements on the 3, 6, and 9 ms dwell time regions.

Shown in Figure 3.11 is the data taken at 15 K collected by Andrew Martin and myself. The sample was excited using a Helium-Neon continuous wave laser operating at 633 nm and 101 μW. The laser was focused onto an area approximately 30 μm in diameter through a 0.7 numeric aperture, infinity corrected objective lens. The luminescence was collected through the same objective and dispersed by a 150 G/mm reflection grating in a 0.75 m spectrometer. Data was collected using a liquid nitrogen cooled CCD detector [49]. Also shown for reference is data from a region of the sample without FIB patterning.

For each of the patterned regions we see three distinct emission peaks. The peak at 1.48 eV is the GaAs substrate emission which is relatively unchanged by the patterning process.

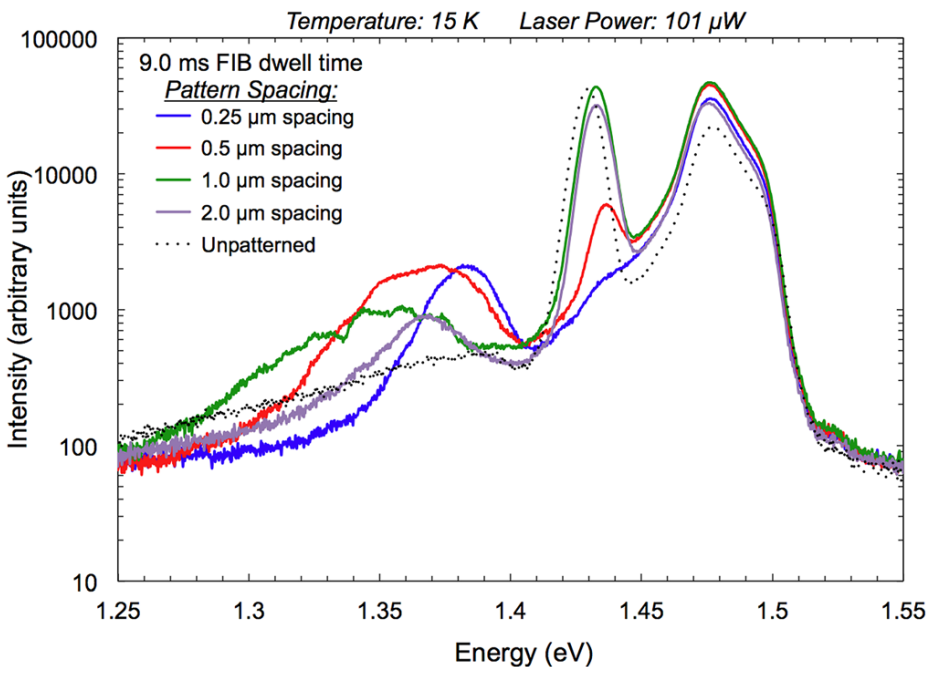

Figure 3.11: Photoluminescence measurements for pattern spacings of 0.25, 0.5 1.0, and 2.0 μm. FIB dwell time was 9 ms, and data was collected at 15 K.

This follows expectation since it is a bulk material and should not be significantly affected by patterning or InAs deposition. Any differences in the GaAs peak are small and can be attributed to the layers of GaAs between the InAs layers. We attribute the peaks between 1.43–1.45 eV to the InAs wetting layer. We see that as the pattern spacing decreases the wetting layer intensity decreases and shifts to higher energy The last peaks range from 1.34 to 1.39 eV and correspond to the InAs QDs. These trends are more difficult to visually identify. Instead we analyze the peak positions and intensities separately.

In Figure 3.12 we show the peak emission energy for the wetting layer and QD peaks. As the pattern spacing increases, the wetting layer energy decreases monotonically. For larger spacing, less of the InAs wetting layer material is consumed in the QD formation. However this stops after the 1 μm pattern spacing. As we see in the wetting layer emission the energy remains constant after 1 μm. This is in excellent accord with the AFM measurements of the QD sizes from Section 3.3.1. At smaller pattern spacings, the FIB sites compete for

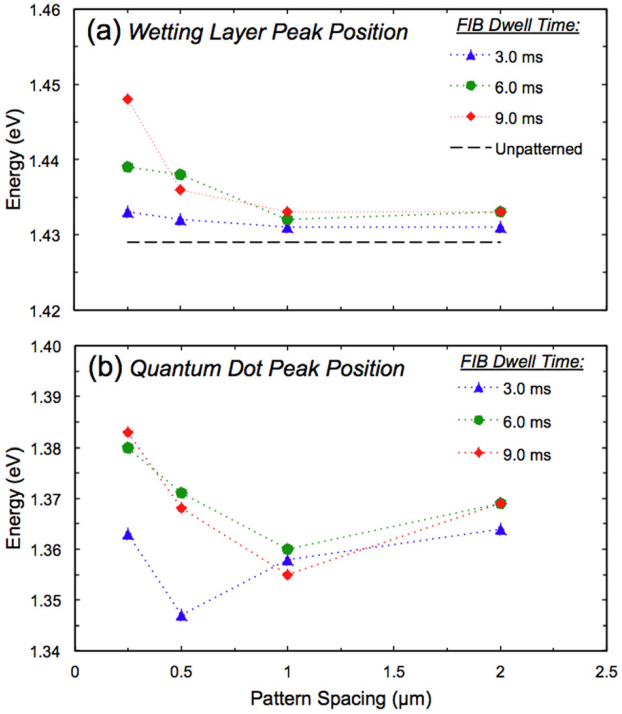

Figure 3.12: (a) Wetting layer and (b) quantum dot photoluminescence peak energy for various pattern spacings and dwell times.

InAs material to form QDs. This leads to a decrease in the thickness of the remaining InAs wetting layer since material is used up in the QD formation. Thinner wetting layers lead to higher confinement energies since it is simply a quantum well as described in Section 2.1.

For the QD peak energies we have more complicated trends. From 0.25 – 1.0 μm pattern spacing, the QD energy decreases. This is likely due to the changes in the dimensions of the QD. We know the QDs continue to increase in size as the pattern spacing increases since more InAs is available at each site for dot formation. Larger dots lead to less confinement and thus lower energy. At the higher pattern spacings of 1–2 μm we see the energy increases. We know from our AFM analysis in Section 3.3.1 that the size of these QDs when uncapped are relatively constant [48]. During the capping process, GaAs deposition creates strain on the wetting layer. Some of the InAs from the QDs may dissolve to decrease the strain during this deposition. As the distance between the FIB sites increases there is more GaAs material

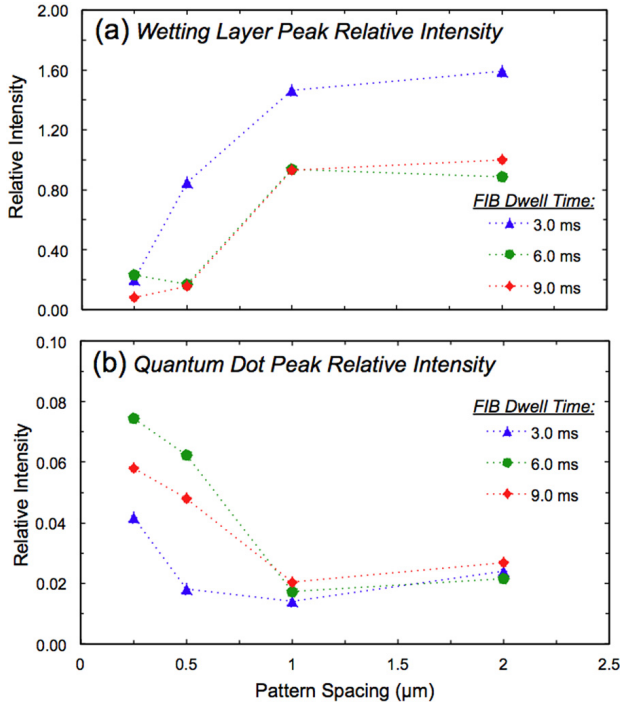

Figure 3.13: Photoluminescence intensity of the (a) wetting layer and (b) quantum dot peak for various dwell times and pattern spacings.

available per site for dissolution into the QD upon capping. This would lead to small final QD sizes, which would tend to increase the QD energy [49].

In Figure 3.13, we show the changes in the photoluminescence intensity for various pattern spacings. These graphs are scaled such that the peak intensity of the 9 ms dwell time, 2 μm pattern spacing region has relative intensity 1.0. As the pattern spacing increases from 0.25–1.0 μm, the wetting layer intensity increases. Since more material is available to the wetting layer, it follows there is more emission at higher spacing. As previously found, the wetting layer is not appreciably used more from 1–2 μm so the intensity remains relatively constant. For the quantum dot emission we find the inverse trend. The intensity decreases as pattern spacing increases. This is primarily due to the fact that few dots are formed due to the lower areal density of FIB sites. At the 2 μm pattern spacing, we have an increase in emission. We suspect this is due to the greater confinement of these QDs serving as better "traps" for the excitons prior to recombination.

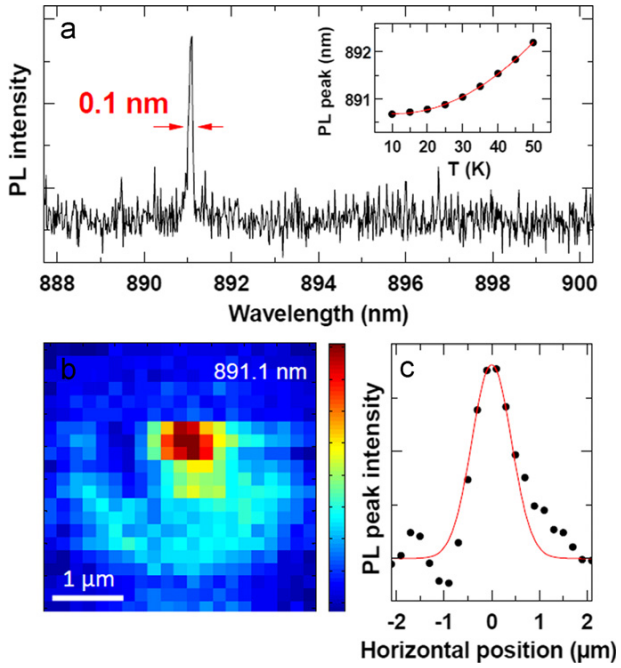

Figure 3.14: (a) Photoluminescence spectra of a single quantum dot with the scanning incident beam on the position of peak intensity. (b) Spatial map at 891.1 nm in the vicinity of the QD peak. (c) Horizontal intensity line scan through the QD peak demonstrating 1 μm spatial resolution.

3.4.2 Single QD measurements

Our success with optical measurements of ensembles of patterned QDs led us to investigate the optical properties of the individual dots. We used a slightly different sample from the previous studies in which the InAs thickness was decreased to 1.5 monolayers and the GaAs thickness was increased to 45 nm. 11 layers of InAs were grown and the surface was left uncapped. We cooled the sample to 30 K and used a 1200 G/mm reflection grating in the same 0.75 m spectrometer. Figure 3.14 shows the photoluminescence of a single QD with line width of only 0.1 nm (160 μeV)[44].

Jieun Lee and Deborah Tien collected this data using a confocal microscope setup [44]. The excitation laser passes through a beam splitter and off a steerable mirror prior to entering the objective. The emission is collected through the same objective, mirror, and beam splitter. It then passes through a pair of matched lenses separated by two focal lengths. At

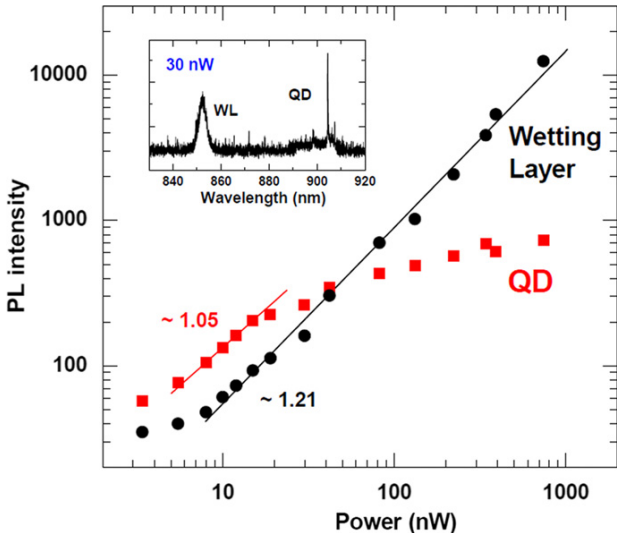

Figure 3.15: Photoluminescence intensity dependence on pump power intensity for a single QD and the wetting layer. Spectra of the QD and wetting layer are shown in the inset for 30 nW pump power.

the beam waist, we positioned a 150 μm pinhole. In this configuration, any rays entering the lens pair that are not from the focal point of the objective will be blocked by the pinhole. Rays that are allowed to pass are then collimated by the second lens. Theoretically, this system should have a diffraction limited resolution of 0.6 μm [58].

In Figure 3.14, we used a steerable mirror to scan the beam across a $5\mu\text{m} \times 5\mu\text{m}$ area of our sample using step sizes of 0.2 μm. The intensity map is shown as well as a horizontal line scan through the peak emission. Based on the full width at half maximum of the emission, we find this system has a lateral resolution of 1 μm, very close to the diffraction limit [58].

In Figure 3.15, we see the power dependence of the wetting layer and a single QD. Across nearly the entire power range the wetting layer shows a power law dependence with slope 1.2. However the QD shows linear dependence at low power and saturation at higher power. This is consistent with emission from a single photon emitter and evidence of the quantum nature of this emission. Measurements of multiple QDs at different locations all showed the same trend [44].

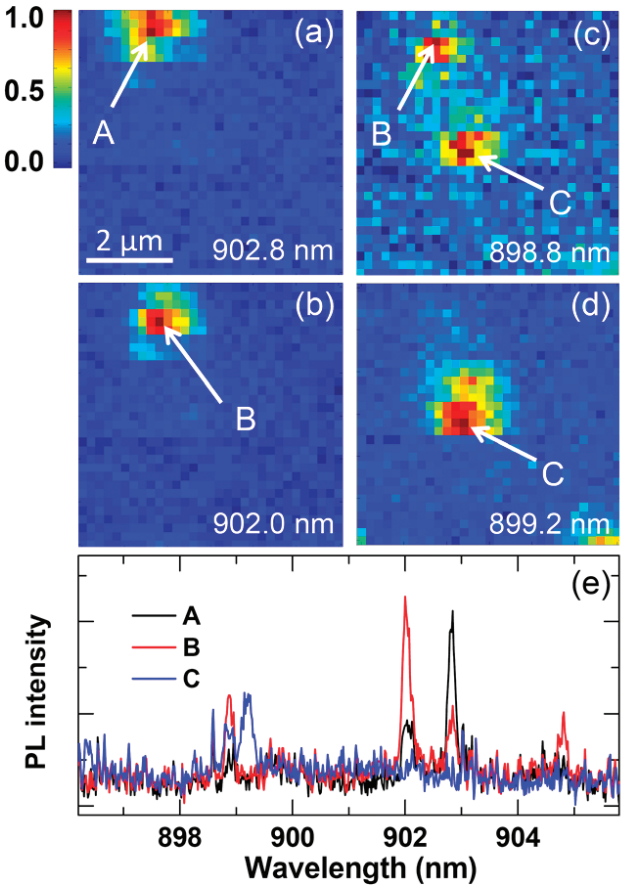

Figure 3.16: Photoluminescence intensity maps at (a) 902.8 nm, (b) 898.8 nm, (c) 902.0 nm, and (d) 899.2 nm. Each map is scaled relative to the maximum intensity at that wavelength. Letters A, B, and C represent the same spatial location for each map. (e) Spectra at positions A, B, and C.

3.4.3 Mapped multiple QD photoluminescence

Having measured single dot luminescence and determined our optical resolution, we sought to determine the optical quality and placement of multiple dots within our patterned regions. Figure 3.16 shows the photoluminescence intensity at four different wavelengths for the same spatial region collected by Jieun Lee and Deborah Tien. Also shown is the luminescence as a function of wavelength for the three positions labelled in the maps. From map (c) we see the spacing between site B and C is 2 μm, which corresponds very well to our FIB pattern separation [43].

We also performed large area scans identifying many individual dot peaks. Figure 3.17 shows a map of the peak locations for these dots. The color of the dots indicated the peak QD wavelength. AFM images from the surface of the sample show mounds similar to those in Figure 3.7. Each mound is associated with one FIB pattern site. For reference, the gray circles of Figure 3.17 represent the size of these mounds. There are two striking features of this map. First, the dots tend for form on the mound locations that are due to the FIB patterning. Second, dots of similar energy tend for form at the same locations.

Also shown in Figure 3.17 are counting statistics for the QDs. A rough estimate of the width of the QD frequency distribution correlates well with the QD photoluminescence of our previous ensembles (Figure 3.11). Defining a "site" as the gray circle shown in (a) the frequency of QDs per site is also given. Over 65% of all sites contain optically active dots. The number of dots per site is quite high due to the mound formation. Based on these optical studies and the previous image measurements, there is good reason to expect we can further improve our placement of optically active single quantum dots using low FIB dwell times and few InAs QD layers.

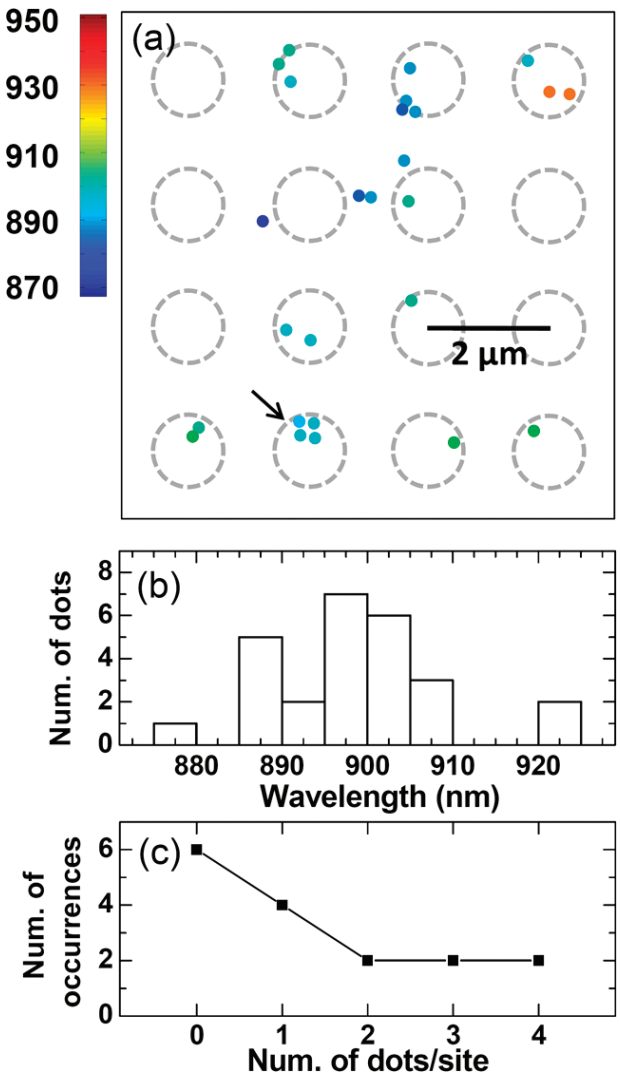

Figure 3.17: (a) Map of the spatial location of the QD peak intensity. Gray outlines show typical mound size for reference. (b) Number of dots at each peak wavelength. (c) Number of dots per mound site.

Chapter 4

Photonic crystal band structure

4.1 Maxwell's equations in periodic media

Photonic crystals are a fascinating, non-intuitive application of Maxwell's Equations to media with periodically varying permittivity. By manipulating the structure of the media in different ways, it is possible to engineer the dispersion relation of light. This enables one to build high quality "mirrors," waveguides, and cavities. There are excellent treatments of the theory behind these photonics crystals by both Sakoda [66] and Joannopoulos [31]. The subject is so rich, we only have the time to touch upon the aspects relevant to our particular study. We begin with Maxwell's equations in a medium with no sources are given in SI units [30].

$$\nabla \cdot \mathbf{D}(\mathbf{r}, t) = 0 \tag{4.1}$$

$$\nabla \cdot \mathbf{B}(\mathbf{r}, t) = 0 \tag{4.2}$$

$$\nabla \times \mathbf{E}(\mathbf{r}, t) = -\frac{\partial \mathbf{B}(\mathbf{r}, t)}{\partial t} \tag{4.3}$$

$$\nabla \times \mathbf{H}(\mathbf{r}, t) = \frac{\partial \mathbf{D}(\mathbf{r}, t)}{\partial t} \tag{4.4}$$

If we restrict ourselves to non-magnetic media, we can assume $\mathbf{B}(\mathbf{r},t) = \mu_0\mathbf{H}(\mathbf{r},t)$, where μ_0 is the permeability of free space. We can also relate the electric displacement vector to the electric field by $\mathbf{D}(\mathbf{r},t) = \epsilon_0\epsilon(\mathbf{r})\mathbf{E}(\mathbf{r},t)$. Here we explicitly show that the relative permittivity, $\epsilon(\mathbf{r})$, has spatial dependence.

$$\nabla \cdot [\epsilon(\mathbf{r})\mathbf{E}(\mathbf{r},t)] = 0 \tag{4.5}$$

$$\nabla \cdot \mathbf{H}(\mathbf{r},t) = 0 \tag{4.6}$$

$$\nabla \times \mathbf{E}(\mathbf{r},t) = -\mu_0 \frac{\partial \mathbf{H}(\mathbf{r},t)}{\partial t} \tag{4.7}$$

$$\nabla \times \mathbf{H}(\mathbf{r},t) = \epsilon_0\epsilon(\mathbf{r}) \frac{\partial \mathbf{E}(\mathbf{r},t)}{\partial t} \tag{4.8}$$

Combining these equations gives a wave equation at any point in space. It is important to note that solutions to these differ from the standard solutions to the wave equation due to the spatial dependence of $\epsilon(\mathbf{r})$. We substitute one equation into the other to get a differential operator for just $\mathbf{H}$ or $\mathbf{E}$.

$$\nabla \times \left[\frac{1}{\epsilon(\mathbf{r})} \nabla \times \mathbf{H}(\mathbf{r},t) \right] = \epsilon_0 \nabla \times \frac{\partial \mathbf{E}(\mathbf{r},t)}{\partial t} \tag{4.9}$$

$$= \epsilon_0 \frac{\partial}{\partial t} \left[\nabla \times \mathbf{E}(\mathbf{r},t) \right] \tag{4.10}$$

$$= -\epsilon_0\mu_0 \frac{\partial^2}{\partial t^2} \mathbf{H}(\mathbf{r},t) \tag{4.11}$$

Using the fact that the speed of light in vacuum can be related to the permittivity and permeability of free space by $c^2 = 1/\mu_0\epsilon_0$, we arrive at the following differential equations which are closely related to the standard wave equation.

$$\nabla \times \left[\frac{1}{\epsilon(\mathbf{r})} \nabla \times \mathbf{H}(\mathbf{r},t) \right] = -\frac{1}{c^2} \frac{\partial^2}{\partial t^2} \mathbf{H}(\mathbf{r},t) \tag{4.12}$$

This differential equation is what Joannopoulos refers to as the "master equation" [31]. If we treat the electric and magnetic field vectors as being separable (spatially vs. temporally), we can assume that the right hand side of the equation has solutions of the form $\mathbf{H}(\mathbf{r},t) = \mathbf{H}(\mathbf{r})e^{-i\omega t}$.

$$\nabla \times \left[\frac{1}{\epsilon(\mathbf{r})}\nabla \times \mathbf{H}(\mathbf{r})\right] = \frac{\omega^2}{c^2}\mathbf{H}(\mathbf{r}) \tag{4.13}$$

Up to this point, we have done nothing but rewritten Maxwell's equations in non-magnetic media and assumed that the solutions were separable. If we go back to the assumption that the permittivity of the material varies periodically, we can use Bloch's Theorem to simplify the problem. To do this, we assume that since the permittivity is periodic, then the solutions to Maxwell's equations will also be periodic with the same periodicity [38].

$$\mathbf{H}(\mathbf{r}) = \sum_{\mathbf{k},n} \mathbf{H}_{\mathbf{k},n}(\mathbf{r}) = \sum_{\mathbf{k},n} \mathbf{v}_{\mathbf{k},n}(\mathbf{r})e^{i\mathbf{k}\cdot\mathbf{r}} \tag{4.14}$$

In these equations, we assume that the set $\{\mathbf{H}_{\mathbf{k},n}\}$ form a complete basis. $\mathbf{k}$ will be the wave vector and n is the order. The wave vectors $\{\mathbf{k}\}$ cover all reciprocal space, but we will find later that we need to only consider the first Brillouin zone [31]. If we expect the solutions to Maxwell's equations to be waves, we can suppose that the solutions are of the form $e^{i\mathbf{k}\cdot\mathbf{r}}$. Therefore we can simplify this problem to solving for the spatially dependent $\mathbf{v}(\mathbf{r})$, which must satisfy the conditions

$$\mathbf{v}(\mathbf{r}) = \mathbf{v}(r + \mathbf{a_i}), \qquad i = 1,2,3 \tag{4.15}$$

Here we have assumed $\{\mathbf{a}_i\}$ are the primitive lattice vectors of the photonic crystal. That is, $\epsilon(\mathbf{r}) = \epsilon(\mathbf{r} + \mathbf{a}_i)$.

Since $\mathbf{v}(\mathbf{r})$ is periodic, we can represent it using a Fourier series [4]. We set $\{\mathbf{b}_i\}$ as the reciprocal lattice vectors of the photonic crystal ($\mathbf{a}_i \cdot \mathbf{b}_j = 2\pi\delta_{ij}$), and l_i as integers. We can

move around our reciprocal vector space by any $\mathbf{G} = l_1\mathbf{b}_1 + l_2\mathbf{b}_2 + l_3\mathbf{b}_3$.

$$\mathbf{H}_{\mathbf{k},n}(\mathbf{r}) = \sum_{\mathbf{G}} \mathbf{H}_{\mathbf{k},n}(\mathbf{G}) e^{i\mathbf{G}\cdot\mathbf{r}} e^{i\mathbf{k}\cdot\mathbf{r}} = \sum_{\mathbf{G}} \mathbf{H}_{\mathbf{k},n}(\mathbf{G}) e^{i(\mathbf{G}+\mathbf{k})\cdot\mathbf{r}} \tag{4.16}$$

Now looking back at Equation 4.13, we see that we need to operate on factors of $1/\epsilon(\mathbf{r})$. Since $\epsilon(\mathbf{r})$ is periodic, so is $1/\epsilon(\mathbf{r})$. Thus we can also expand this as a Fourier series.

$$\frac{1}{\epsilon(\mathbf{r})} = \sum_{\mathbf{G}} \kappa(\mathbf{G}) e^{i\mathbf{G}\cdot\mathbf{r}} \tag{4.17}$$

$$-\sum_{\mathbf{G}} \kappa(\mathbf{G}-\mathbf{G}')(\mathbf{k}+\mathbf{G}) \times \{(\mathbf{k}+\mathbf{G}') \times \mathbf{H}_{\mathbf{k},n}(\mathbf{G}')\} = \frac{\omega_{\mathbf{k},n}^2}{c^2} \mathbf{H}_{\mathbf{k},n}(\mathbf{G}) \tag{4.18}$$

We now have an eigenvalue problem that can be solved numerically. For any given wavevector $\mathbf{k}$ and mode n we can determine the eigenvalue $\omega_{\mathbf{k},n}^2/c^2$. A variety of numerical techniques exist to determine this. Iterative eigensolvers such as MPB [35] can determine these dispersion relationships between ω and $\mathbf{k}$ for arbitrary geometries.

Since we know $\epsilon(\mathbf{r})$ we can calculate $\kappa(\mathbf{G})$. The number of vectors, $\mathbf{G}$, and modes, n, we use will determine the accuracy of our calculation. Modern computer speeds give very good convergence in solving these problems for arbitrary geometries in minutes [35].

4.2 One dimensional photonic crystals

Having the necessary theory in place to study these structures, we first look at well known phenomena. For example, distributed Bragg reflectors can be built by alternating layers of different materials with specific thicknesses [71]. We have four parameters in this case – the permittivities and thicknesses of each of the two media. We calculate ω for each $\mathbf{k}$ along the axis of media and find some interesting phenomena.

Suppose we begin with the limit of $\epsilon_{\text{hi}} = \epsilon_{\text{low}}$. This is essentially a uniform medium,

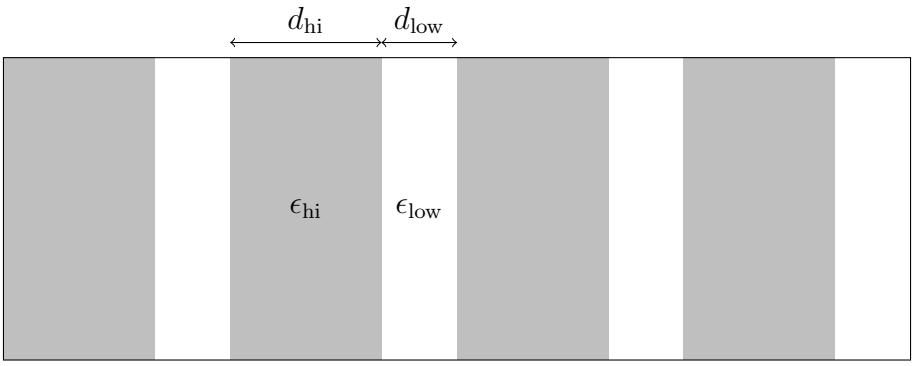

Figure 4.1: One dimensional photonic crystal schematic.

so we expect a linear dispersion relationship. That is, $\omega = ck$. In Figure 4.2, we see this relationship. If however, we begin with a large quantity of low dielectric material and add a small amount of high dielectric material, it changes the dispersion relationship significantly. We see that near the band edge ($ka/2\pi = 1/2$) there are now certain frequencies (shown in gray) that have no corresponding wave vectors. This is referred to as a "photonic band gap" since there is now a band of frequencies for which light cannot propagate through this material since there is no associated wave vector, $\mathbf{k}$.

For a physical interpretation of the origins of this band gap we can consider what is happening at the band edge since this is where the two bands separate. This occurs when the wavelength is roughly twice the lattice parameter ($ka/2\pi = a/\lambda = 1/2$). Since the unit cell has symmetry though its origin, there are only two ways to align this mode. Either the peak must be centered about either the center of the high dielectric material or the low dielectric material [31].

Low frequency modes typically concentrate their electric field energy in high permittivity regions. This can be seen roughly understood by looking at Equation 4.13. Higher ϵ should in general have lower ω solutions. So the mode centered about the high dielectric material will have more field energy in lower frequencies regions than the mode centered about the low dielectric. The first band (lower ω) near $ka/2\pi = 1/2$ will have lower frequency than

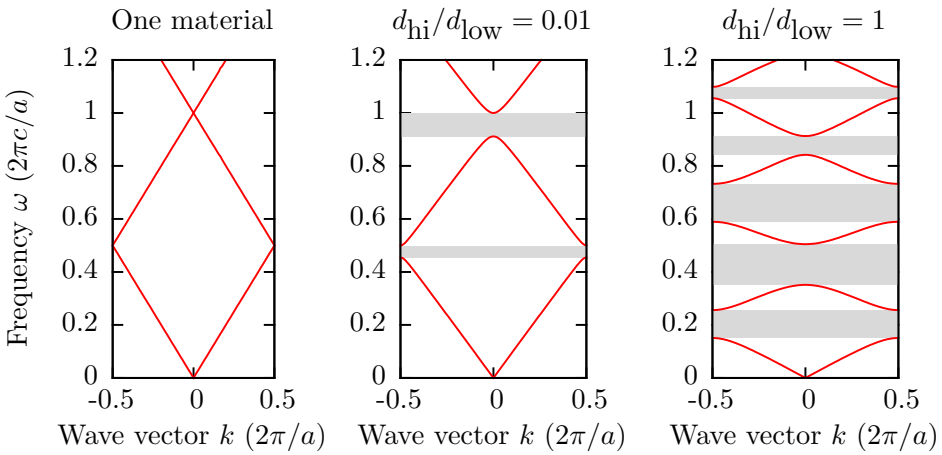

Figure 4.2: Photonic band diagrams for one dimensional multilayer crystal.

the second band near the same k. This gives rise to the separation of the two bands.

In Figure 4.2, we see that by adding a small amount of high dielectric material we have another band gap near $k = 0$ and $\omega = 0.9$. This occurs when the wavelength is roughly equal to the lattice constant (higher order modes are folded back into the first Brillouin zone). Again, the same argument can be made for the symmetry forcing one mode primarily into the high dielectric material and the other mode into the low dielectric material. At higher frequencies, we continue to see this same pattern.

To make devices, we often want to make the size of the band gap as large as possible. A useful metric to measure the size is the dimensionless quantity of the size of the band gap (in frequency) divided by the frequency at the center of the gap, $\Delta\omega/\omega_g$. The so-called "gap-mid gap ratio" indicates how effective the material rejects light in that region [31].

We approach tuning this $\Delta\omega/\omega_g$ by looking at the available parameters to vary. We expect that the best result will come from materials that have very large differences in their permittivities. This is usually limited to the materials available. In general, large differences in ϵ lead to larger band gaps. We can also see in Figure 4.2 that by varying the relative thickness of the materials we can greatly increase the band gap. With equal parts of high and low dielectric material we see many large band gaps.

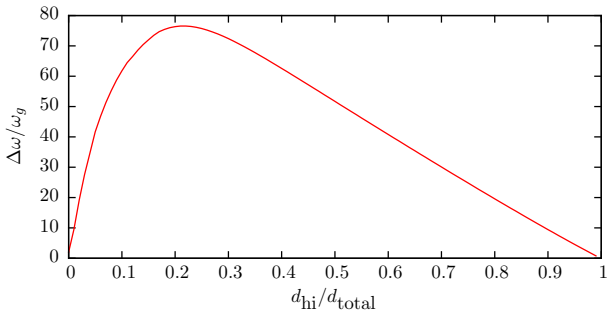

Figure 4.3: Dependance of gap-mid gap ratio for 1D multilayer crystal on material thickness.

In Figure 4.3 we calculate $\Delta\omega/\omega_g$ for the first gap as a function of the ratio $d_{\rm hi}/d_{\rm total}$. At $d_{\rm hi}/d_{\rm total} = 0$ and 1 we have no gap since it is a pure material and should have linear dispersion. For $\epsilon_{\rm hi} = 13$ and $\epsilon_{\rm low} = 1$, the largest $\Delta\omega/\omega_g$ for the first band gap occurs when $d_{\rm hi}/d_{\rm total} = 0.22$. By tuning these parameters, we are effectively tuning the dispersion relationship of this material.

This is a particularly useful example because it has a well known analytical result. To make a perfect dielectric mirror, we simply create a quarter wave plate. That is, we want one quarter of a wavelength inside each material [71]. For our optimized solution, $d_{\rm hi} = 0.22 d_{\rm total}$. The frequency at the middle of the band gap is $\omega_g = 0.3169\ 2\pi c/d_{\rm total}$. So, for the high dielectric material $\lambda_{\rm hi} = \lambda_{\rm vac}/n_{\rm hi} = 2\pi c/n_{\rm hi}\omega_g = 0.875 d_{\rm total}$. One quarter of this wavelength is $0.22 d_{\rm total}$, just as expected. For the low dielectric material, we have the same result with $\lambda_{\rm low}/4 = 3.155 d_{\rm total}/4 = .789 d_{\rm total}$.

The lessons we can learn from this simple one dimensional case can be expanded to two and three dimensions. In general, lower lying modes primarily concentrate themselves in high dielectric material. The more we can force the next modes into the low dielectric modes, the larger our photonic band gaps will be.

4.3 Two dimensional lattice of air holes in GaAs

We now extend our analysis into two dimensions. In doing so, we must also break our discussion into the differences between the transverse electric (TE) and transverse magnetic (TM) modes for our crystal. We know from studies of crystal structure that in 2 dimensions we have 5 types of lattices [38]. The two most promising candidates are the square and hexagonal lattices [31, 66]. We will consider our lattice to extend infinitely in the $\hat{\mathbf{z}}$ direction and consist of air holes ($\epsilon = 1$) inside GaAs ($\epsilon = 12.9$).

4.3.1 Square array of air holes

We begin by looking at a square array of holes. When analyzing the band structure we typically look only at the wave vectors along the edges of the first Brillouin zone. This is because minima and maxima for bands almost always lie along these lines. For a square array, the reciprocal lattice is also square. So the problem can be simplified to looking along the Γ, X, and M points. These are shown in Figure 4.4(a).

Figure 4.4(a) shows the band structure for a square array of holes with $r = .45a$. We can see that this structure has both TE and TM band gaps, but the gaps appear at very different frequencies, due to the electromagnetic boundary conditions. For the TM modes, the electric field is parallel to the interfaces of air and GaAs. Since $E_{||}$ is continuous at the interface, the energy density $\epsilon|\mathbf{E}|^2$ is much lower in the air regions [31]. This allows us to concentrate more energy in the high dielectric regions, giving lower frequencies. The next band up must be orthogonal to this band forcing more electric field energy into the air regions with higher frequency. Since the regions of high dielectric are connected, this severely limits the ability to "push" modes into the air regions. Thus we have a very small TM band gap.

For the TE modes the connected regions actually help create a large band gap. The first two modes operate very similarly to the 1D case presented before. The exception is that

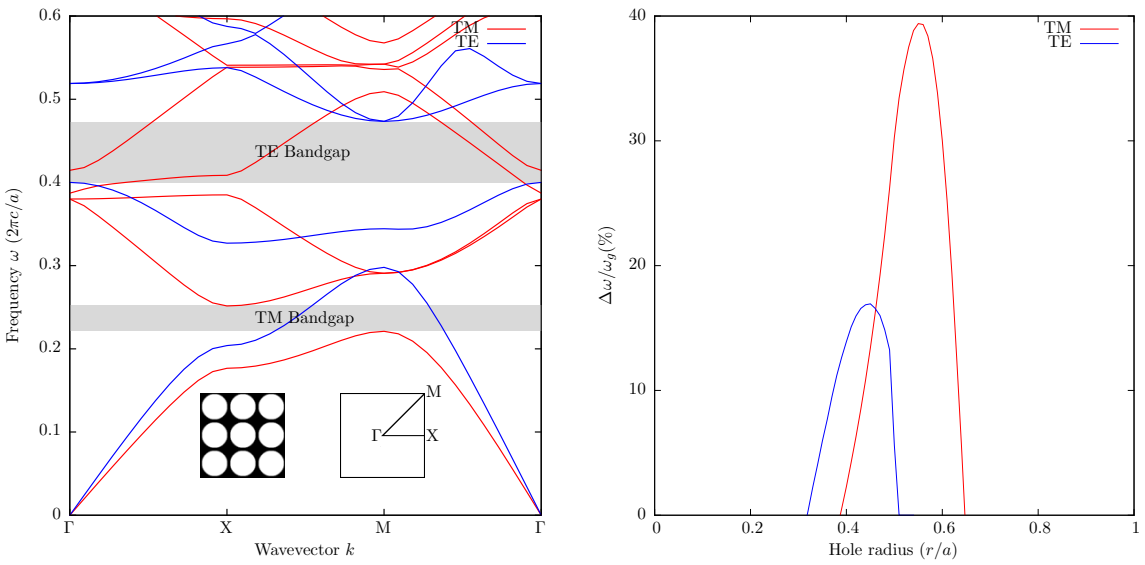

Figure 4.4: (a) Band diagram for two dimensional square array of air holes in high dielectric material. (b) Band gap dependance on hole radius for square array in two dimensions.

they now have two orthogonal paths of high dielectric material. This allows the first two bands to have low frequency. The third band must be orthogonal to the first two bands, which will be primarily in the air region. This gives the third band much higher frequencies, leading to the large TE band gap at relatively high frequency.

We look at the available tuning parameters for this structure. In Figure 4.4(b) we vary the hole radius and consider the gap/midgap ratio. We see that for TE modes, $r = 0.45a$ gives the largest gap of 17%. For TM modes, we can get nearly 40% band gap for $r = .55a$. It is important to note that this large band gap occurs when the high dielectric material is completely isolated ($r > .5a$). This prevents the second TM mode from concentrating in high dielectric regions Some work demonstrates inverted versions of these structures with high dielectric pillars in air [61]. For our purposes we are more interested in planar PC cavities.

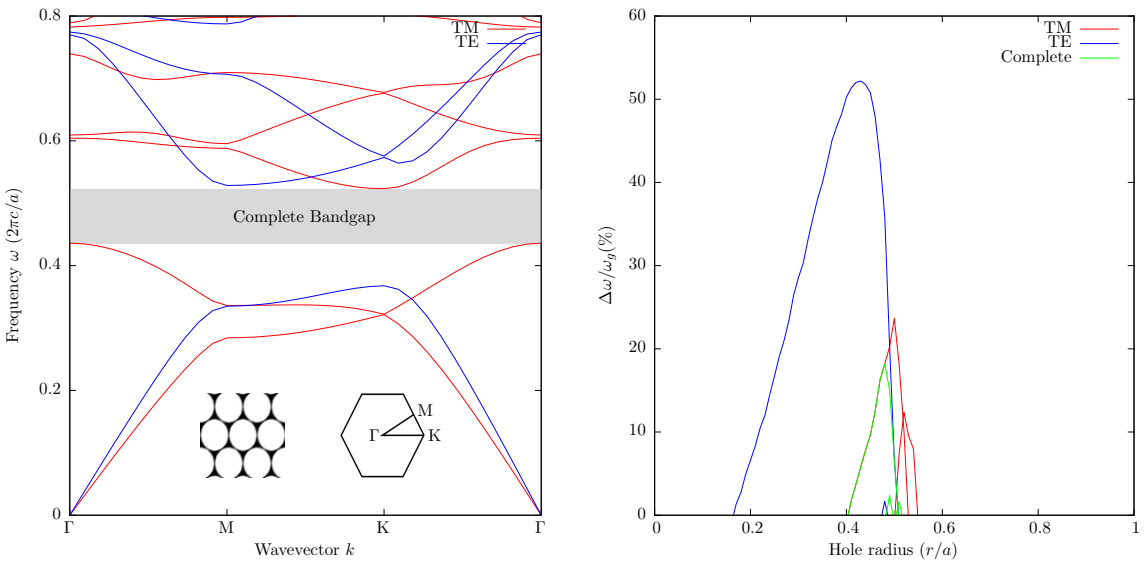

Figure 4.5: (a) Band diagram for two dimensional hexagonal array of air holes in high dielectric material. (b) Band gap dependance on hole radius for hexagonal array in two dimensions.

4.3.2 Hexagonal array of holes

We saw in the previous section that isolated regions of high dielectric material led to TM band gaps and thin veins of material led to TE gaps. As an effort to optimize a design containing both isolated regions and connected veins, we turn to hexagonal arrays. In Figure 4.5(a) we see the results for $r = 0.48a$. At this radius, the holes are almost touching with a very thin material between them. This leads to the ideal conditions for both TE and TM modes. This configuration has a complete photonic band gap, a region with overlapping TM and TE gaps. This is interesting because it tells us that a structure of this form will completely block light at those frequencies, even though both materials are optically transparent.

For two given material permittivities, this structure has one parameter to optimize – the hole radius. In Figure 4.5 we show the band gap sizes for the TE and TM modes. We see that for small r, TE polarizations can have large band gaps. We also see that TE modes with a hexagonal array give larger band gaps than TE modes in a square array. At first glance, it may appear that TM modes in square arrays are ideal, but this only occurs when

$r > 0.5a$ which means the high dielectric material is not connected. Our goals are focused on planar devices in which the high dielectric material must be continuously connected. For this reason we focus instead on the TE modes in a hexagonal array.

Creating a structure with a complete band gap can be beneficial, but there is a significant flaw in this design for use in a planar device. Eventually, we will want to create a thin slab of high dielectric material suspended in air. For $r = 0.48a$ this leads to very thin veins that provide the structural support for the high dielectric material. When building these devices, the veins are too brittle for practical purposes. So instead we switch from examining devices with a complete band gap and see how we achieve the best possible band gap while maintaining structural integrity. Additionally, we must extend our analysis to include finite slab thicknesses.

4.4 Hexagonal lattice of air holes in a GaAs slab

We turn our attention to three dimensions, since we are interested in building planar photonic crystals. Introduction of a finite slab thickness significantly alters the mode profile of our hexagonal array. The first question we ask is how thick our slab should be to get the best possible band gap. For an infinitely thin slab we will no longer have modes confined to the slab. This is simply due to the fact that all modes would have to spend a significant amount of time in the air above and below the slab resulting in higher frequencies. Higher mid gap frequency leads to smaller $\Delta\omega/\omega_g$. Also, these frequencies may lie too close to the light cone to get discrete modes in the crystal [31]. To the other extreme, as the slab thickness is increased, the modes tend to have more energy in the high dielectric material lowering the frequency of all of the modes. Higher order modes have more vertical nodes, so they are more affected than lower order modes. So as the slab thickness increases the higher order modes are "pulled down" more than the lower order modes until the gap disappears. The

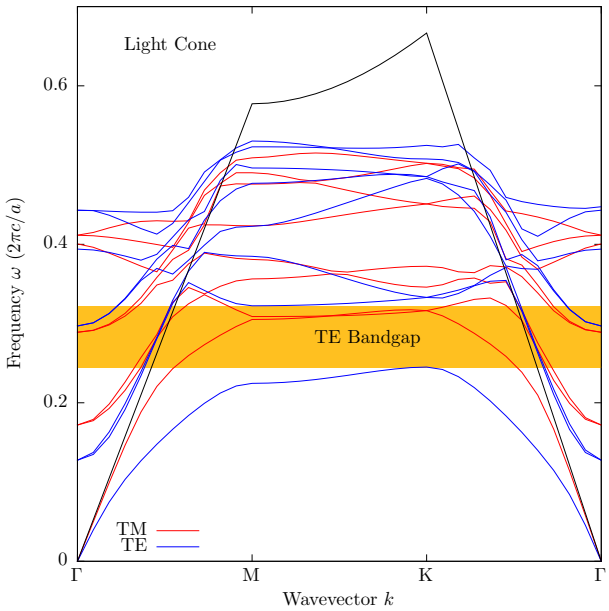

Figure 4.6: Band diagram for three dimensional slab with hexagonal air hole lattice.

optimal slab thickness is a balance of these two effects, which occurs at $d_{\text{slab}} \sim 1.2a$.

In Figure 4.6, we show the band structure for a hexagonal array slab with thickness $0.6a$ and hole radius $0.3a$. There appears to be no band gap at all. We must remember that the speed of light sets the upper limit on the $\omega(k)$ relationship. Any frequencies above the "light cone" shown cannot exist, even though they are valid solutions to our eigenvalue problem. Taking this into account, we have a TE band gap with $\omega = 0.284\ 2\pi c/a$ and $\Delta\omega/\omega = 27\%$.

4.5 Scale invariance

One of the most interesting features of Maxwell's equations is that they are scale invariant. Electromagnetic phenomena have no inherent scale. Any solution we find to our band structure will work for *all* frequencies, provided we choose our material parameters correctly. In our analysis we will define some scaling parameter of interest. For many of our materials, we use the lattice parameter, a. This is typically a feature particular to the system of interest. To express units of frequency, we use units of c/a or angular frequency $2\pi c/a$.

One very useful feature of this scale invariance is that we can design a system to have a large band gap at some scale invariant frequency. Then we can build the structure to give us any frequency of interest by setting parameters accordingly. For example, suppose we develop a photonic crystal slab with a large band gap centered around $f = 0.259c/a$. Our input parameters are that the holes are hexagonally arranged with radius $r = 0.3a$ and the slab has thickness $d = 0.6a$. If we wish to use this in a device that operates at 950 nm, we perform a few simple calculations.

$$f = \frac{c}{\lambda_0} = \frac{c}{950\text{nm}} = 0.259\frac{c}{a} \tag{4.19}$$

$$a = (0.259)(950\text{nm}) = 246\text{nm} \tag{4.20}$$

Thus we need to make the material have lattice parameter 246 nm, thickness $(0.6)(246\text{nm}) = 148\text{nm}$, and hole radius $(0.3)(246\text{nm}) = 74\text{nm}$. This is an incredibly useful feature to these calculations. Care must be taken since we have assumed the permittivity of the material is independent of frequency. In practice, this is not true. Since we often know the frequencies we are interested in working with, we can usually approximate the permittivity to good accuracy.

We must also take into account two features of the temperature dependence of our material's properties. First, the permittivity of the material does have some temperature dependance [23]. Second, as temperature changes the material will physically expand or contract which changes the size and separation of the air holes [38]. Transitioning from room temperature to 10K we have observed 2% changes in material responses simply due to these effects in our samples.

Chapter 5

Photonic crystal cavities

An interesting phenomena that occurs when creating photonic crystals is the existence of defect states in the band structure. We begin with a hexagonal lattice of air holes in a thin GaAs slab and introduce a defect by filling in one air hole. At the location of this site, we have violated the conditions of Bloch's Theorem given in Chapter 4. If we move far away from the defect site in the photonic crystal we should return to a place where the conditions are satisfied sufficiently. Intuitively, this means that frequencies which are forbidden in the crystal may exist at the defect site. However if light at that frequency exists at the defect site, it should be confined spatially since it encounters a perfect mirror when penetrating any direction into the crystal. This essentially creates an optical cavity at the defect site.

As with any optical cavity, we need to quantify how well light is confined and localized. To parameterize the confinement, we use the quality factor – the ratio of energy stored to the energy dissipated per cycle in the device [56]. For describing the light localization we refer to the mode volume of the cavity. Mode volume definitions vary depending on the process of interest. For our case, we are concerned with the Purcell enhancement (or suppression) of spontaneous emission of a quantum dot embedded within the cavity. For our purposes, the quantity of interest is the ratio of the quality factor to the mode volume (Q/V). We define

our mode volume based on Purcell enhancement [15].

$$V \equiv \frac{\int \epsilon(\mathbf{r}) \left|\mathbf{E}(\mathbf{r})\right|^2 d\mathbf{r}}{\max\left(\epsilon(\mathbf{r}) \left|\mathbf{E}(\mathbf{r})\right|^2\right)} \tag{5.1}$$

Determining these parameters cannot be done with the same frequency domain analysis used in Chapter 4. Instead, we switch to time domain analysis and use finite difference time domain (FDTD) simulations. We create a finite sized photonic crystal and simulate Maxwell's equations through the material. By seeding the cavity with a broad (frequency) Gaussian pulse at a position of low symmetry in the crystal and allow the system to decay, we can monitor the electric field. After many time cycles have passed only the cavity defect state frequencies will remain. We repeat this process using a narrower band input pulse until we are exciting only a single mode of the cavity. We can then monitor the electric field at the anti-node of the cavity to determine the quality factor. The mode volume is then calculated at the end of the simulation. Details on the procedures used can be found in Appendix A.

When discussing the mode volume of a photonic crystal, different units can be found in the literature. Some work reports findings in μm or another SI unit. This is often not a useful measure since it applies only to the specific choice of lattice scale. Since photonic crystals are scale invariant [31], a more useful measure will scale as well. In our work, we describe the mode volume in terms of the crystal lattice parameter, a. Other work uses either wavelength or half wavelength in the high dielectric material, $(\lambda_0/n)^3$ or $(\lambda_0/2n)^3$ respectively. λ_0 represents the free space wavelength. With a known central frequency, conversion between the two is simple. Suppose the mode has frequency $f = 0.26c/a$ and the high dielectric material is GaAs with $n = 3.59$.

$$\frac{\lambda_0}{n} = \frac{c}{nf} = \frac{c}{(3.59)(0.26c/a)} = 1.07a \qquad \frac{\lambda_0}{2n} = 0.54a \tag{5.2}$$

For all of the simulations shown the following parameters were assumed. The permittivity

of the GaAs slab and air were 12.9 and 1.0, respectively. The simulation was performed on a Yee grid with approximately 20 pixels per lattice parameter [53]. At least 12 air holes surround the cavity in all directions. $1.5a$ of air surrounds the slab on each side. The hole radius is $0.3a$, and the slab thickness is $0.6a$. A perfectly matched layer surrounds the simulation on all sides with thickness $1a$. The source pulse is Gaussian with $f_{\text{can}} = 0.25c/a$ and $\delta f = 0.1c/a$ initially. After finding the cavity mode frequency the results were iteratively run at narrower bandwidth until only a single mode was excited. The cavity mode is polarized with the electric field in the plane of the slab pointed in the direction perpendicular to the cavity axis (E_y) .

5.1 Hexagonal cavities

The simplest cavity can be created by removing a single hole from our lattice, known as a H1 cavity (hexagonal, one layer of holes removed). This creates a very small spatial area where the periodicity assumptions are violated. We can expect that this small spatial defect will correspond to a small mode volume. In Figure 5.1 we show the electric field mode profile superimposed on an outline of the cavity structure. Also shown are the H2 and H3 structures, which have two or three layers of holes removed, respectively.

Looking at the H1 mode profile we see the electric field is highly concentrated at the antinode at the center of the cavity and more weakly near the edges of the two holes adjacent to the cavity. This cavity has a very small mode volume of $0.32a^3$. The cavity's corresponding quality factor is only approximately 310. This cavity has excellent localization but very poor quality.

We can explain the low quality factor by looking at the limiting cases for a cavity. For an infinitely small cavity light could not exist since there would be no defect, leading to $Q = 0$. At the other extreme, suppose we had an infinitely large cavity that met a perfect photonic

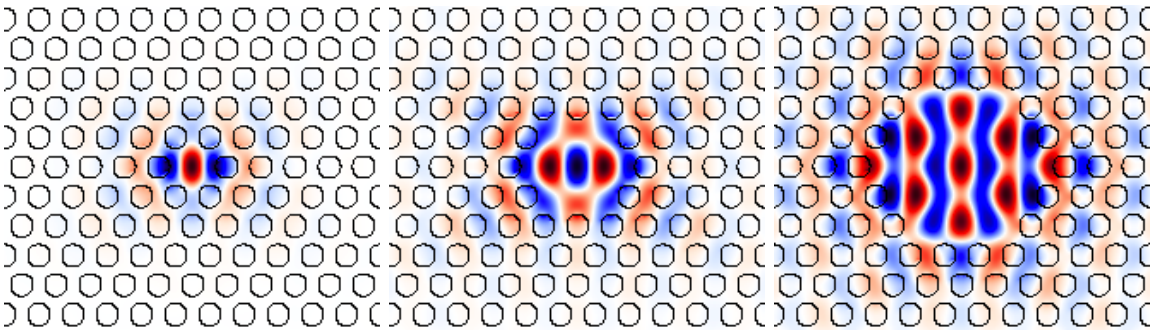

Figure 5.1: H1 (hexagonal, one layer removed), H2, and H3 cavity mode profiles, respectively.

crystal. This we would expect to give perfect reflection for light in the photonic band gap of the crystal, corresponding to $Q = \infty$. For the H1 cavity, we have a very small defect region so we have a very small quality factor. As we increase the size of our cavity we should expect the quality factor and the mode volume to increase.

By expanding to a H2 cavity we see a significant increase in both the quality factor ($Q = 2595$) and the mode volume ($V = 1.01a^3$). The mode profile in Figure 5.1 shows the electric field travels much further into the photonic crystal. By penetrating further into the crystal, the mode experiences more of the conditions of an ideal photonic crystal, reflecting the signal back toward the cavity. This leads to a higher quality factor at the expense of the mode volume. Additionally the cavity now has three strong antinodes in comparison to the one of the H1 cavity.

Extending this analysis to the H3 cavity, we find the effects are further exaggerated. The H3 cavity has $Q = 89291$ and $V = 3.32a^3$. From the mode profile, we see the localization is extremely poor. In fact the cavity now contains 7 strong antinodes and 6 weaker antinodes. From the perspective of simply considering the Q/V ratio, one might be led to consider the H3 cavity superior to the H2. We prefer our cavity to have a single point of interaction. For this reason the H3 cavity is not ideal. Table 5.1 shows a direct comparison of the hexagonal cavity parameters, as well as those of the linear cavities described in Section 5.2. These cavities do teach us an important aspect of their design. Poor spatial localization often leads

Cavity type	$f(c/a)$	Q	$V(a^3)$	$Q/V(a^{-3})$
H1	0.281	310	0.32	969
H2	0.253	2595	1.01	2381
H3	0.253	89291	3.32	26894
L3	0.260	5946	0.74	8035
L5	0.258	39098	1.16	33705

Table 5.1: Calculated parameters for various hexagonal and linear cavity designs.

to higher quality.

In Table 5.1 we also see the H1 cavity frequency is approximately 10% higher than that of the other cavity designs. This feature is unique to the extremely small cavity configuration [15]. In order to support a stable cavity mode, at least one half wavelength of the mode must exist within the cavity. For a single missing hole the typical wavelength cannot fit. Instead the mode must have a higher frequency (lower wavelength) yet still exist within the photonic band gap of the crystal. Modes closer to the band edges are less well bound, decreasing the cavity quality factor [31].

5.2 Linear cavities

An alternate approach to removing holes in a hexagonal array is to remove them linearly. By removing 3 holes linearly we have an L3 cavity, the most widely used photonic crystal in recent literature [21]. Using the same logic as with the hexagonal cavities, we expect that increasing the cavity size with increase both the mode volume and quality factor. A table of calculated parameters for all cavity styles shown is given in Table 5.1.

We see that going from a H1 to a L3 and then a L5 cavity we do increase both mode volumes and quality factors. The changes in linear cavities are very different from those of the hexagonal cavities. Going from the H1 to the H2 cavity the mode volume increase by a factor of 2.5 and the quality increases by a factor of 8.4. In contrast going from an H1

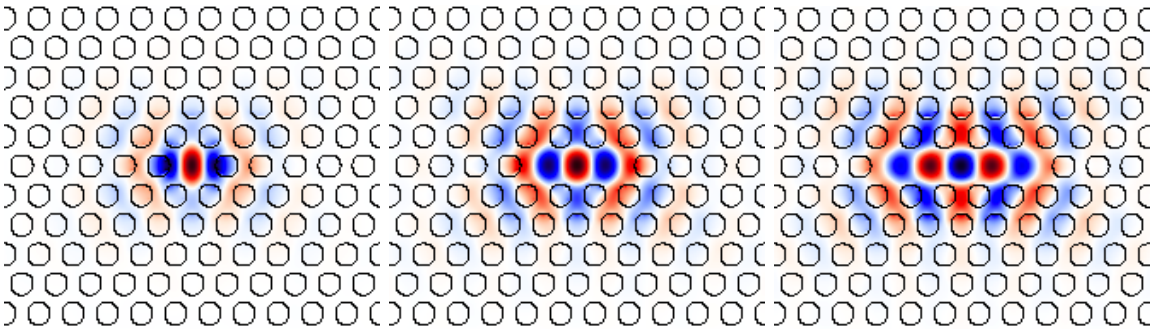

Figure 5.2: H1, L3 (linear, three holes removed), and L5 cavity mode profiles, respectively.

to a L3 cavity the mode volume increases by a factor of 2.3 and the quality factor by 19.2. The linear cavity gives better quality and mode volume than the hexagonal. The reason for this lies in the cavity mode polarization. The electric field is oriented perpendicular to the L3 cavity axis. By placing the additional holes above and below the cavity we have more thinly connected regions of high dielectric material, which we know leads to our photonic band gap. So adding these holes actually improves our quality factor by making our system more of an ideal photonic crystal. Additionally the fact that we have fewer missing holes forces the mode into a more concentrated region, lowering the mode volume.

When comparing the H3 and L5 cavities, we do not see the same trend. The L5 cavity has lower quality than the H3 cavity. Since the H3 cavity is so much larger than the L5 cavity it does have a larger quality factor. The mode volume of the L5 cavity is half that of the H3 cavity. Ultimately it has a significantly better Q/V ratio than the H3.

Since the linear cavities have much better optical responses than their hexagonal counterparts, they are encountered much more in the literature [21]. The L3 cavity is the most widely studied. Since it has high quality, low mode volume, and only 3 antinodes, it is an excellent candidate for studying light matter interactions.

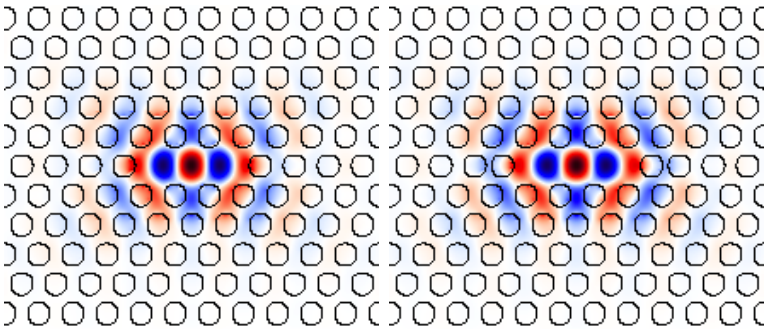

Figure 5.3: L3 cavity mode profiles for the unmodified design (left) and for the edge holes shifted by $0.19a$ (right).

5.3 Edge hole shifted L3 cavity design

In an attempt to further improve the photonic crystal cavities, researchers have tried a number of approaches to modify their design. Some have shown improved quality factors by elongating a line of holes [75] or varying the radii of a line of holes [21]. Others have modified the radii of the holes surrounding the cavity [60]. Some have even exchanged the round edge holes with very unusual designs based on an optimization procedure [24]. The most common method is that formulated by Akahane et al., in which they shift the two holes on the edge of the cavity outward [2].

In Figure 5.3 we show the mode profile for an unmodified cavity and that of one with the two holes shifted outward by $0.19a$. The profile does not appear to be significantly different. For the shifted cavities the mode volume is higher, increasing from $0.74a^3$ to $0.91a^3$. This 23% increase is detrimental for our device design. It is greatly offset by the increase in cavity quality factor from 5.9×10^3 to 1.3×10^5. These combined effects lead to an overall Q/V improvement by a factor of 17.9.

In previous work [2] it was found that a $0.15a$ shift was optimal. That was assuming the slab was composed of silicon ($\epsilon = 11.68$). For our purposes, we are more interested in GaAs ($\epsilon = 12.9$). Since GaAs has a higher permittivity the ratio of the permittivities of the two materials is greater (GaAs to air instead of silicon to air). A higher ratio leads to more

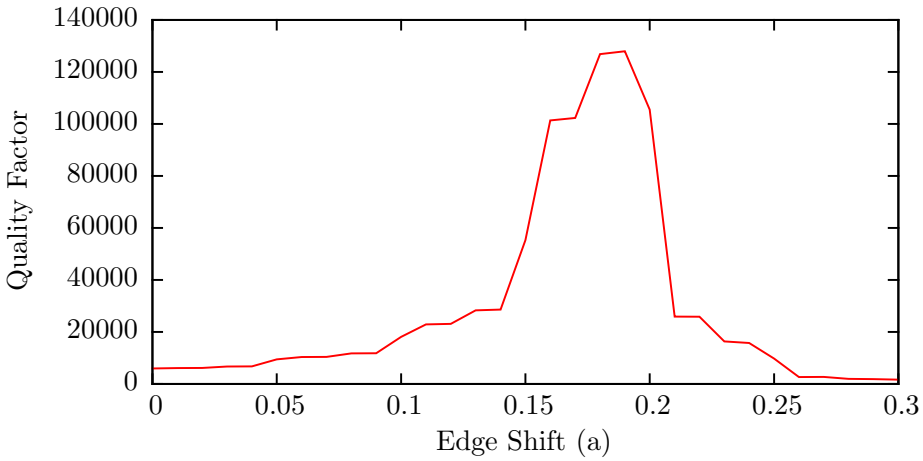

Figure 5.4: Effects of shifting edge holes outward on quality factor.

dramatic differences in material response [31]. We find that at this higher permittivity the optimal shift is $0.19a$ instead of $0.15a$. For comparison to the literature, our materials give $Q = 5.5 \times 10^4$ and $V = 0.91a^3$ for the $0.15a$ shift.

By moving the two edge holes outward we see a trend similar to that of the previous cavity designs. As we increase the size of the cavity we tend to increase both the quality factor and the mode volume. By just moving two holes rather than removing them (such as in the L5 cavity) we prevent additional antinodes from forming. Since fewer antinodes is preferable and we can achieve qualities higher than the L5, this cavity provides an excellent platform for study.

We wish to gain further insight into why we can achieve such great improvements in cavity quality with this simple hole movement. Akahane et al. assumed that an ideal cavity would fit some exact number of half wavelengths of its fundamental mode inside the cavity [2]. If we were to look at the electric field spatially this would correspond to a sinc envelope function multiplied by the fundamental mode. By Fourier transforming this spatial profile they found the sinc envelope function created large components with low wave vector. The low wave vector components lead to being able to match the leakage conditions necessary for Snell's law [2, 31]. If instead they were able to create a cavity with a Gaussian envelope

function, its transform would have very small components with low wave vector. This should lead to less leakage and thus higher quality factor.

This interpretation leads to the conclusion that the best cavities will have gentle mode profile transitions at the cavity boundaries. More gentle changes in the cavity profile should lead to the desired result. Since we cannot put an intermediate type material in the edge holes, an alternative approach must be taken. One method might be to change the size of the hole [68]. Alternately the edge shift gives the mode more space in the high dielectric material during the transition. They show the Fourier transform of their modes gives very low intensity at small wave vector. Ultimately gentle transitions from a cavity to an ideal photonic crystal lead to improved quality factors.

Chapter 6

Advanced photonic crystal cavity designs

In Section 5.3, we found that small modifications to the structure of a photonic crystal could lead to large changes in the quality factor of the cavity. The previous results only looked at varying a single parameter - the position of the two holes near the edge of the cavity. From our results of H2 and H3 cavity analysis, we anticipate that modifying the holes just above and below the cavity will affect its performance. We also know from other studies that we can create or modify cavities by adjusting the radii of the holes [2, 75].

We consider the holes labelled in Figure 6.1. We assume the holes surrounding the cavity will move along lines of symmetry to improve the cavity design. Hole "A" is allowed to move along the X direction. Holes "B" and "C" can move along the X or Y directions. All of these holes are allowed to vary in radius. Using this parameterization we have 8 parameters to vary. From Akahane, et al. [2] a shift in position of $0.05a$ made a significant difference in the calculated quality factors. For this reason, we assume the parameters may shift by up to $\pm 0.3a$ to ensure we capture the entire range of possible solutions. Using a grid size of $0.05a$, this leads to 12 data points for shifting positions. For the radius we consider a reasonable

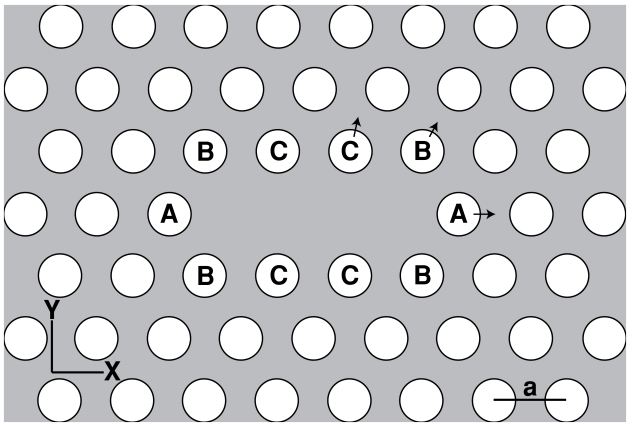

Figure 6.1: Holes to modify on the L3 design.

range to be from $0.1a$ to $0.4a$. Beyond this, we cannot successfully create such device since the material will be too thin to support the cavity. Breaking this into 10 points of interest we have a total parameter space of 2×10^8 [68].

Performing FDTD simulations at low resolution, maximally exploiting symmetry, and using parallel processing, we can perform a single calculation in 30 seconds on average using current technology. Even with this impressive speed, we can not fully explore our parameter space since the simulations would run for many years. Instead, we turn to a nature inspired search program to optimize our cavity performance, the Gravitational Search Algorithm (GSA).

GSA falls under a larger class of uninformed search algorithms. They are called as such since the current position in parameter space can give no information about the region in its vicinity. That is, we have no available heuristic to determine we which direction in parameter space we should go to continue our search. Optimizing a photonic crystal cavity is one such search. At any given point in parameter space corresponding to hole shifts and size changes, we can perform a FDTD simulation to determine the quality factor and mode volume of the cavity. However we receive no information about how changing one particular parameter in any direction will affect these figures. In effect, it is like having a deterministic function of

which we cannot determine the gradient.

A simple method to approach these problems would be to create a grid in parameter space. We select some number of divisions to apply to the parameter space and divide it equally along those lines. We perform simulations at each intersection and repeat this process until we find a converged solution. This would work extremely well for a monotonic function. Anything more complicated can easily get the search stuck in a local optimal solution.

One common approach to these problems are algorithms that search outward from some starting point in parameter space. After a certain amount of searching ("search depth") they stop and examine the best prospects. They then begin the search again using these as the new starting point and repeat this process [65]. This depth-first search has been applied to many problems, such as playing chess and traffic routing. It also suffers from the problem that if the global optimal solutions lie in a small disconnected parameter space they may never be discovered.

6.1 GSA methodology

The GSA is a new method inspired by nature. If you have a set of particles distributed randomly in space with random velocities, they will tend to form a bound object due to their mutual gravitational attraction. In general, the lowest mass particles will accelerate faster than the larger mass particles. We apply this to a search in our parameter space. We randomly place "agents" inside our eight dimensional parameter space. For each agent, we calculate its quality factor and mode volume. We then assign a "mass" to each agent scaled linearly with Q/V. Based on the position of every agent in relation to every other agent in parameter space, we allow the system to accelerate for one time step. We then repeat the FDTD simulations at the new agent positions, update their masses, and repeat the process. This continues until the system converges onto one position or we reach some

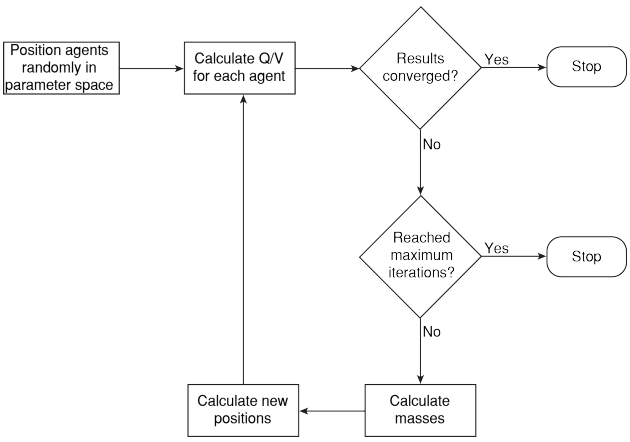

Figure 6.2: GSA schematic.

stopping criteria (such as number of iterations performed). A flow diagram of how this is performed is shown in Figure 6.2.

When implementing this search algorithm we must choose some initial bounds of our search space. Care must be taken when choosing these bounds since they can affect the program's ability to find the most optimal solution. If the boundaries are too large, the search may take steps too large to find small optimal features in parameter space. If the boundaries are too small then the system may converge on a local optimal solution rather than the global solution. For our search, we set our boundaries for the radii of our holes to be $r_{\min} = 0.1a$ and $r_{\max} = 0.5a$. For the position shifts in either the X or Y direction, we allow them to move in either direction by $0.5a$ ($\Delta x_{\min} = -0.5a$, $\Delta x_{\max} = 0.5a$). We then scale our position in coordinate space to give us dimensionless parameters. For each agent i we have a new position $\mathbf{s}_i$.

$$s_{i,1} \equiv \frac{r_A - r_{\min}}{r_{\max} - r_{\min}} \qquad\qquad s_{i,2} \equiv \frac{r_B - r_{\min}}{r_{\max} - r_{\min}} \tag{6.1}$$

Previous studies have shown the GSA can efficiently find optimal solutions in higher dimensional parameter spaces using 50 agents. To optimize use of available computer architecture we use 48 agents since processors are typically bundled in units of 4 or 8 cores. We

give these agents random initial positions and velocities in our parameter space such that $0 \leq s_{i,j} \leq 1$ for all i, j. While the agents are confined to these limits at the start of the simulation, they can and often do travel outside of these bounds. We do place hard limits on the radii in that they cannot be negative, since such a feature is unphysical.

For each agent, we perform an FDTD simulation to determine its quality factor and mode volume. The details of these simulations are given in Section 6.2. For each agent, we define a fitness function, $f(\mathbf{s}_i)$, according to its ratio of quality factor to mode volume since this is the parameter of interest [62].

$$f(\mathbf{s}_i) = \frac{\text{Quality factor (cavity } i)}{\text{Mode volume (cavity } i)} \tag{6.2}$$

With the fitness function for each agent found we assign masses to each agent. It is important to note that the mass of each agent will be updated at every iteration of the GSA. It maintains no record of the agent's previous mass (memory-less search). For each iteration, we determine the cavity with the minimum fitness function, $f_{\min}$. We also add a small mass δm to prevent the system from having massless agents, since some cavities do not support a mode [68].

$$m_i = \frac{f(\mathbf{s}_i) - f_{\min}}{\sum_j \left[f(\mathbf{s}_j) - f_{\min}\right]} + \delta m \tag{6.3}$$

$$\ddot{\mathbf{s}}_i = \sum_{j \neq i} \frac{G m_j}{|\mathbf{s}_j - \mathbf{s}_i|} \cdot (\mathbf{s}_j - \mathbf{s}_i) \tag{6.4}$$

Based on the position of each agent with relation to every other agent and their masses, we calculate the accelerations for one time step. The form of acceleration used differs from true gravitational acceleration in two significant ways. In nature, the force due to gravity decreases as the square of the distance between two particles. In GSA, the force is independent of the distance yet still points in the direction between the particles. Additionally

the gravitational constant, G, is typically assumed to be constant except on cosmological timescales [13]. In GSA, we allow G to vary over the course of the evolution. Near the beginning we wish our agents to traverse large regions of parameter space, corresponding to a large G. At the end when most agents have converged we want the agents weakly bound (small G) so they can search the parameter space near the optimized position [62]. We model the gravitational constant as a decaying exponential over the lifetime of the evolution.

$$G(t) = G_0 e^{-t/\tau} \tag{6.5}$$

By varying the two parameters G_0 and τ, we influence how quickly the system converges. If G_0 or τ is too small, the system may not converge at all. Conversely if one or both are too large, we find the system converges with little to no exploration. For our simulation, we find $G_0 = 4$ and $\tau = 15$ give good convergence.

6.2 FDTD simulation details

FDTD simulations were performed using the meep software package's c++ interface[53]. A hexagonal lattice with lattice parameter a surrounding the PC cavity consisted of air holes ($\epsilon = 1$) in a GaAs slab ($\epsilon = 12.9$). The slab thickness and hole radii were $0.6a$ and $0.3a$, respectively. For the GSA iterations, the system consisted of 8 air holes surrounding the cavity in every direction followed by a $1a$ perfectly matched layer [8]. The grid's spatial resolution was $0.1a$ and time steps were $0.05a/c$. The initial pulse was Guassian, centered at the cavity origin with central frequency $0.259c/a$ and width $0.05c/a$. After the GSA optimization was completed, the results were performed with spatial resolution $0.025a$ and temporal resolution $0.0125a/c$. The higher resolution simulations were performed with 12 holes on each side of the cavity, iteratively with narrower pulse width until a single mode

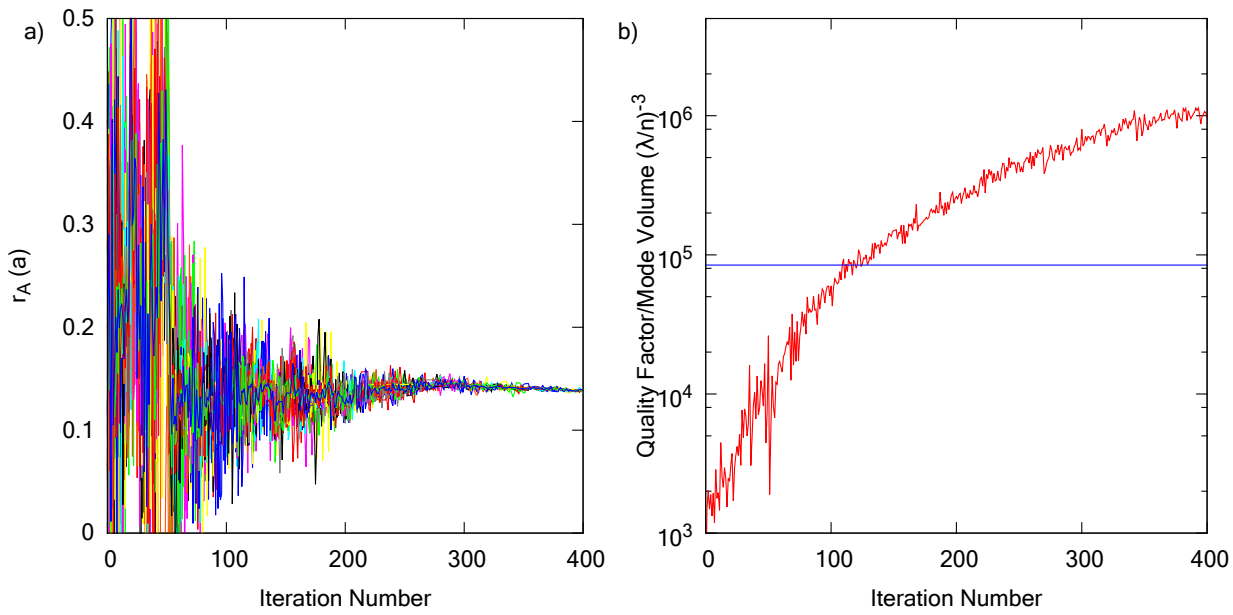

Figure 6.3: Evolution of photonic crystal design by GSA.

was excited [68].

6.3 Optimized L3 cavity results

The GSA simulation was initially allowed to run for 1000 iterations based on previous work [62]. Convergence was reached in 400 iterations and the simulation was halted. Figure 6.3 shows the evolution of one of the search parameters. Each agent is shown in a different color. Here we can see that agents do in fact travel outside our original search space. We also find that after ~ 250 iterations the agents appear to have begun converging on an optimized solution. All other parameters show similar convergence. Figure 6.3 also shows the average quality factor to mode volume ratio of all agents as a function of GSA iteration.

The horizontal line represents the results from shifting the two edge holes outwards by $0.15a$, the benchmark for our comparisons. For this configuration, the quality factor and mode volume are $68,000$ and $0.91a^3$ respectively. This gives the ratio $Q/V = 75,000a^{-3}$.

Hole	Radius (a)	$\Delta x, \Delta y$ (a, a)	Final position relative to origin x, y (a, a)
A	0.15	0.05, 0	2.05, 0
B	0.25	0.07,-0.15	1.57, 0.72
C	0.2	0.09, -0.2	0.59, 0.67

Table 6.1: Optimized L3 cavity parameters.

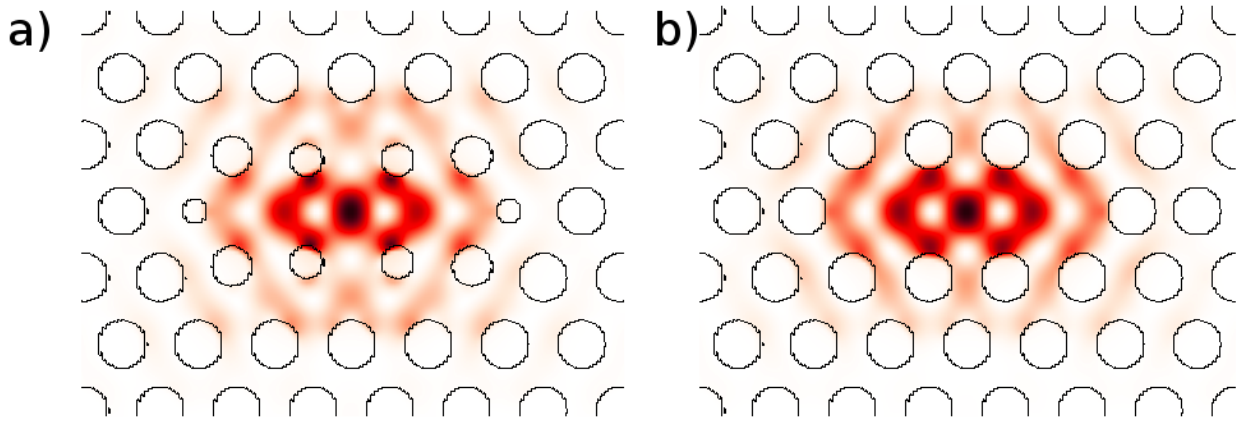

Figure 6.4: Final mode profile upon GSA completion.

The precise numbers differ from Akahane, et al. [2] since we are using a GaAs substrate and they used silicon.

After approximately 120 iterations the average Q/V for our cavities exceeds that of the benchmark. Since these simulations are run at low resolution, they may not be indicative of the actual performance of the current cavity parameters. After the system continues to evolve we find over an order of magnitude difference in the cavity performance over our benchmark. This is very promising, so we extract the final cavity parameters listed in Table 6.1. We perform these simulations at higher resolution and find that our final quality factor and mode volume are $567,000$ and $0.87a^3$. This leads to a final $Q/V = 650,000(\lambda/n)^{-3}$, nearly an order of magnitude improvement [68].

In Figure 6.4, we see the electric field energy density profile for our final parameter search

and the benchmark. We can see the mode is more strongly concentrated at the origin of the cavity. This is beneficial since coupling quantum dots to a cavity mode is strongly dependent on the spatial extent of the mode. Since there is only a 4% difference between the mode volumes, the profile does look very similar as expected.

6.4 Physical interpretation of final cavity design

We consider how the design shown in Figure 6.4 can lead to such enormous gains. There appear to be three phenomena affecting the cavity. The holes surrounding the cavity are decreasing in size, shifting outward in the X direction, and shifting inward in the Y direction. Here we consider each of these in turn to gain intuition about the cavity design.

From Akahane et al [2], we understand that shifting the edge holes of the cavity allows the mode to penetrate further into the photonic crystal structure. In doing so, the field encounters more of an ideal photonic crystal which should lead to perfect reflection back towards the cavity. This would tend to increase the quality factor but also increase the mode volume. Additionally the size of the cavity increases. As seen in Chapter 5, larger cavities typically have higher quality factors and higher mode volumes. Decreasing the radius of the holes has a similar effect on the mode. It creates a more gradual transition from the cavity to the photonic crystal. Again, we expect that the mode will penetrate further into the crystal increasing quality factor and mode volume.

In the Y dimension, the edge holes are shifted inward with the holes closer to the origin are shifted more. We expect this to oppose the changes in radius and X position. We are now creating a more abrupt border between the cavity and the photonic crystal. Since electric fields tend to concentrate in higher dielectric material, these holes are "squeezing" the mode further towards the origin.

Ultimately, we have a balance of these two competing effects. Certain parameters are

tending to increase both the quality factor and mode volume. Other parameters are doing the opposite. The key is then to find the optimal combination. There are many possible combinations that may solve these issues. For example, increasing the radii of the holes and shifting them all outward may be another solution. The parameter space for these cavities may be a very complicated multimodal space. Using an advanced search algorithm such as GSA may be the only way to explore it with current technology. As we can see, GSA definitely shows its ability to find a solution better than the existing standard.

Chapter 7

Coupling quantum dots to photonic crystal cavities

So far, we have presented two very different research projects. The ultimate goal of our agenda has been to connect these two lines of inquiry and build a strongly interacting system. Coupled QDs and photonic crystal cavities have been proposed as one possible platform for building a scalable quantum computer. Here, we show our ability to measure the coupling of a cavity to embedded quantum dots.

7.1 Cavity quality factor measurements

As we found in Chapter 5 a cavity's quality factor is one of its most significant parameters for optical studies. Fortunately this is a feature which can be relatively easily determined experimentally. The quality factor of a cavity can be related to its resonant frequency and full width at half maximum intensity. This can be measured through reflection, transmission, or luminescence.

$$Q = \frac{f_0}{\Delta f} \tag{7.1}$$

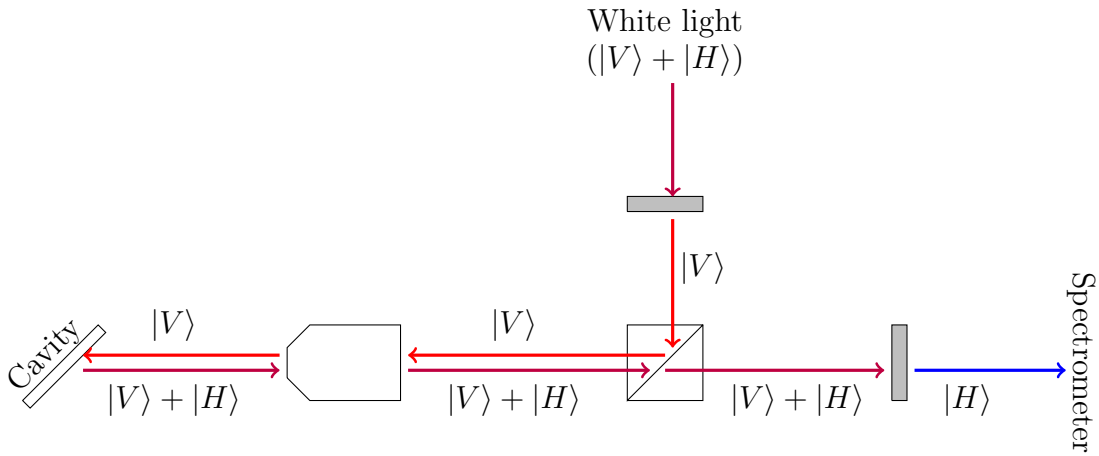

Figure 7.1: Cross polarization experimental setup.

For L3 slabs we have the electric field mode in the plane of the material. This sometimes makes measurements of the cavity difficult since we need an in plane field to measure. If we have optical emitters embedded within the cavity, such as quantum dots, we can use them to excite the cavity mode. If we have cavities with no active media we will need an alternate approach. Some studies use evanescent coupling from a fiber [72] or in plane waveguides [6].

An alternate approach is to construct a cross polarization reflection (or transmission) measurement [63, 17]. A schematic of the experimental setup is shown in Figure 7.1. An unpolarized white light source passes through a linear polarizer oriented vertically. This light passes through a beamsplitter and objective lens before encountering the photonic crystal cavity. We orient the cavity axis 45° off vertical. For frequencies that are not in the photonic band gap of the crystal, the vertical light is reflected back maintaining its vertical polarization. This light encounters another linear polarizer oriented horizontally. The signal is blocked and does not pass through to the spectrometer.

Light at the cavity mode frequency responds differently. We decompose the light into two polarizations depending on the angle between the cavity axis and vertical, θ.

$$\mathbf{E}_Y(\omega) = \mathbf{E}_0(\omega)\cos\theta \qquad \mathbf{E}_X(\omega) = \mathbf{E}_0(\omega)\sin\theta \tag{7.2}$$

Here $\mathbf{E}_Y$ is in reference to the orientation of the cavity. For an E_y mode in the cavity the $\mathbf{E}_Y$ component of the incident light can exist in the cavity and the $\mathbf{E}_X$ cannot. The $\mathbf{E}_X$ component reflects just as the frequencies which are not in the photonic band gap of the crystal. Since the $\mathbf{E}_Y$ component can exist in the cavity, it exists within the cavity before being reemitted out of the cavity plane. This light encounters the second linear polarizer. Since the cavity is oriented at θ with respect to the initial vertical polarizer, it is at the complementary angle to the horizontal polarizer. Thus the $\mathbf{E}_Y$ from the cavity is projected through the second polarizer.

$$\mathbf{E}_{\text{out}}(\omega) = \mathbf{E}_Y(\omega) \sin\theta \tag{7.3}$$

For cavity modes we can measure the intensity of the light emitted in this manner.

$$I_{\text{out}}(\omega) = |\mathbf{E}_{\text{out}}(\omega)|^2 = |\mathbf{E}_0(\omega)|^2 \cos^2\theta \sin^2\theta \tag{7.4}$$

To get the best measure of the cavity mode quality we need $\theta = 45°$. Within $\pm 22°$ the final intensity is within a factor of 2 of the maximal intensity. The measurement of the cavity quality factor is unaffected so long as signal can be detected. In practice we estimated the orientation of the cavity by imaging the cavity onto a camera using alignment markers. The polarizers can be adjusted to give an approximately 45° angle. After signal is attained the orientation can be fine tuned to give the best possible signal. In Figure 7.2 we show example data for a L3 cavity with the edge holes shifted outward by $0.15a$.

Ideally measurements off the sample will show zero reflection signal at all wavelengths. Since the linear polarizers do not have perfect attenuation this cannot be achieved. Any wavelength dependence of the optics will affect the reference signal as well. In practice we record data off the sample region at the wavelength of interest. We optimize the alignment such that we get minimal transmission to the spectrometer at that wavelength. This can be aligned to give a linear response. We then record data on the sample. Optimizing the

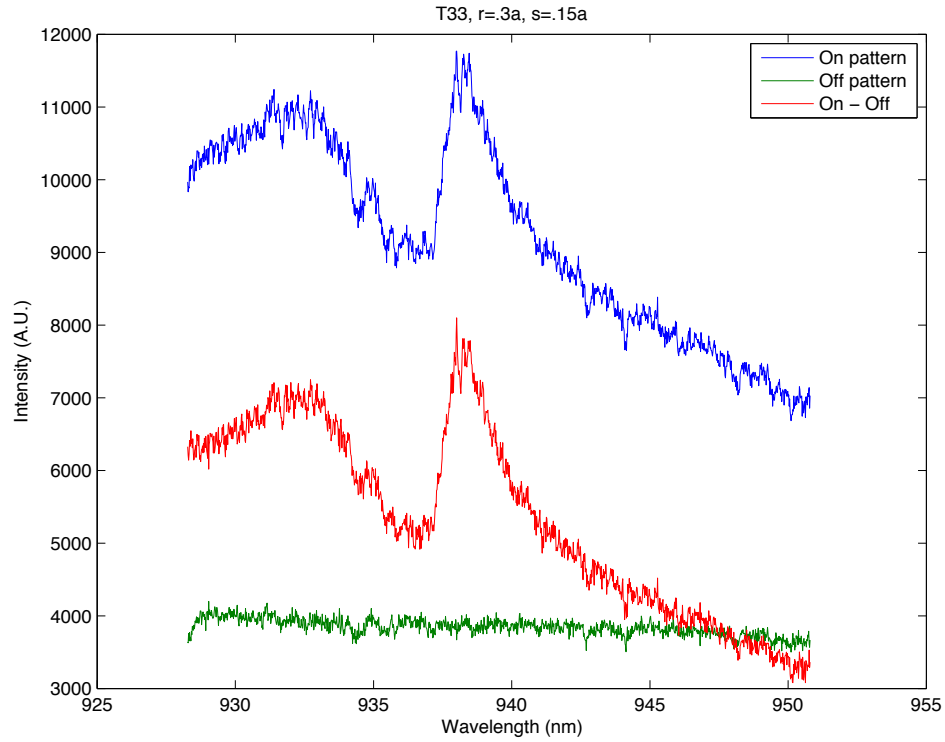

Figure 7.2: Cross polarization data for an L3 cavity. The difference between the reflection on the sample and off the sample is due to the cavity interaction.

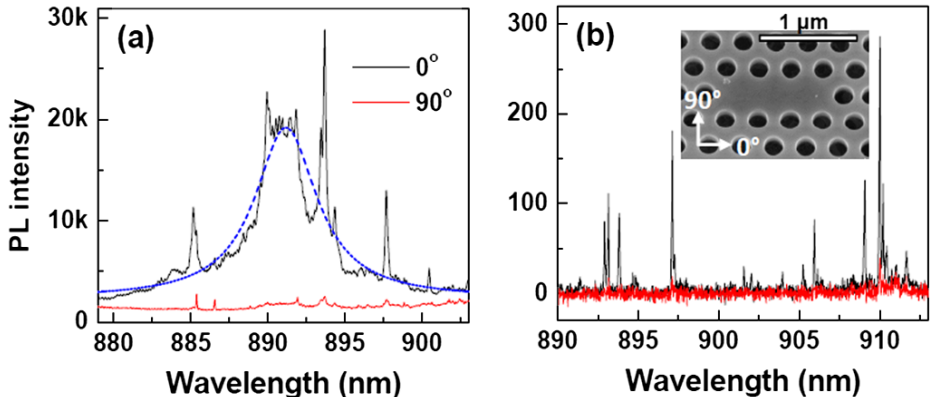

Figure 7.3: Polarization dependent photoluminescence measurements of QDs embedded within a L3 cavity for (a) 190 μW and (b) 0.28 μW. Data in black have the electric field oriented along the cavity axis and data in red are off axis. Inset in (b) is an SEM image tilted by 20°.

collection system on the cavity has significant problems since the patterning of the crystal causes diffraction and additional reflection at unpredictable angles. These tend to increase the signal through the second linear polarizer and make finding the cavity mode difficult. For these reasons, it is best to establish a reference on the unpatterned surface.

7.2 Coupling single QD to cavities

Once the quality factor of the cavity has been determined, the next goal is to couple an active emitter to that cavity. In our case, we wish to couple individual InAs QDs to a photonic crystal cavity and study the interaction effects of the two. Ideally we would use the FIB patterning process demonstrated in Chapter 3. For our first studies we used self assembled dots due to their high areal density [42]. Andrew Martin grew a single layer of InAs QDs in the middle of a 150 nm thick GaAs layer. A L3 photonic crystal cavity with the edge holes shifted out by $0.15a$ was created using electron beam lithography and chemical etching. With our growth conditions, the sample has a QD areal density of approximately $500/\mu m^2$ as determined by analysis of a similar uncapped sample [42].

Using a Titanium Sapphire mode locked laser operating at 780 nm Jieun Lee measured the

photoluminescence of our sample with two perpendicular polarizations shown in Figure 7.3. This data clearly shows the polarization dependence of the emission. This can arise from either polarization dependence of the QDs or of the cavity. From AFM images of similarly grown samples, the QDs formed have no significant elongation. Without elongation the dots will not have polarization dependance. As such, the polarization dependence is expected to be due to interaction with the cavity. We see this enhanced emission for both low (0.28μW) and high (190μW) power excitations.

Fitting the cavity emission to a Lorentzian profile [20], we have a quality factor of 190. While this is relatively, low we see there is an distinct difference between the PL from the two incident beam polarizations. This demonstrates coupling exists between the cavity and some of the QDs in the sample. To determine how the strength of the interaction, we constructed an experiment known as luminescence intensity autocorrelation (LIA) [79]. A schematic of the experiment can be seen in Figure 7.4. Pulses from the Ti:S laser are passed through two different paths before realigning spatially. By varying the distance along one path we can vary the time at which the pulses arrive on the sample. The remaining experiment is similar to our other confocal photoluminescence experiments from Chapter 3.

We model the events that occur during the LIA experiment. When the first laser pulse arrives at the sample it creates an exciton that non-radiatively falls into the QD (or is created in the QD). After some characteristic lifetime of the QD, the exciton will decay, giving off the luminescence detected by the spectrometer. If the second pulse arrives after the exciton has decayed, a new exciton is created, which then decays and gives another detection event. If the second pulse arrives before the exciton has had an opportunity to decay, another exciton cannot exist in the QD. For the time being, we neglect biexciton formation. Thus, only a single detection event will occur. As we map the intensity as a function of delay time, we can thus determine the QD lifetime. To see the cavity effects we can perform these measurements in the cavity and in the regions of the sample without a cavity.

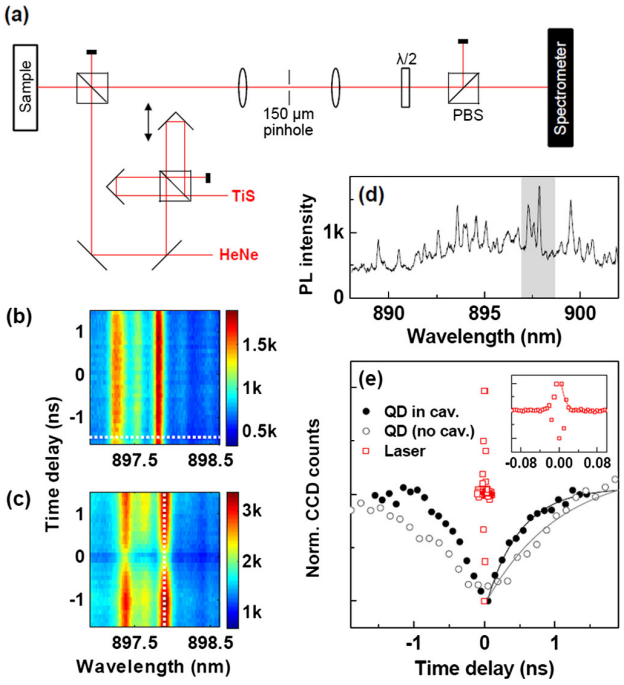

Figure 7.4: (a) Luminescence intensity autocorrelation experimental setup. PL intensity as a function of delay line position with the fixed arm (b) blocked and (c) unblocked. (d) Spectra at long delay time indicated by white dashed line in (b). (e) PL intensity as a function of delay line for QDs inside and outside the cavity. Also shown is the pump laser autocorrelation, also magnified in the inset.

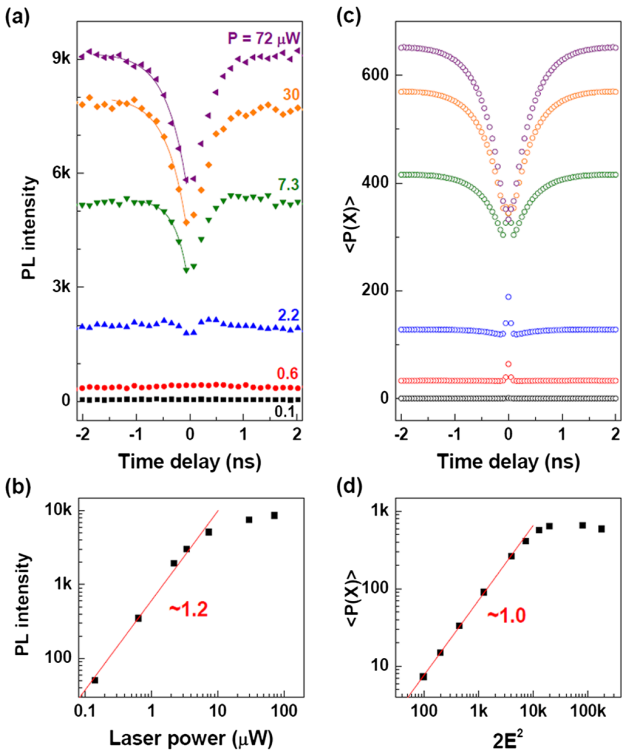

Figure 7.5: (a, c) Photoluminescence intensity as a function of pulse delay for pump powers from 0.1–72 μW. (b, d) Intensity as a function of laser power for a single pulse. (a) and (b) are experimental data and (c) and (d) are from simulations.

In Figure 7.4, we show sample data for our experiment. With the fixed path blocked we see the intensity is constant for the majority of the delay length. This shows the excellent optical alignment of the experiment, which may be a significant source of error. With the fixed path unblocked, we see a clear trend around the zero delay where the signal decreases to about half of the maximum. Plotting the intensity of a single dot inside the cavity as a function of delay time shows the significant decrease in QD lifetime. Fitting this we find the cavity lifetime is approximately half that of a dot outside the cavity [42].

Our explanation of the LIA assumes that the QD is fully excited by the first laser pulse. In our experiment we use identical pulses, though this is not necessary. To ensure we are operating in the saturation regime, we performed the experiment at multiple laser powers and measured LIA and the PL intensity. Figure 7.5 shows our data as well as theoretical

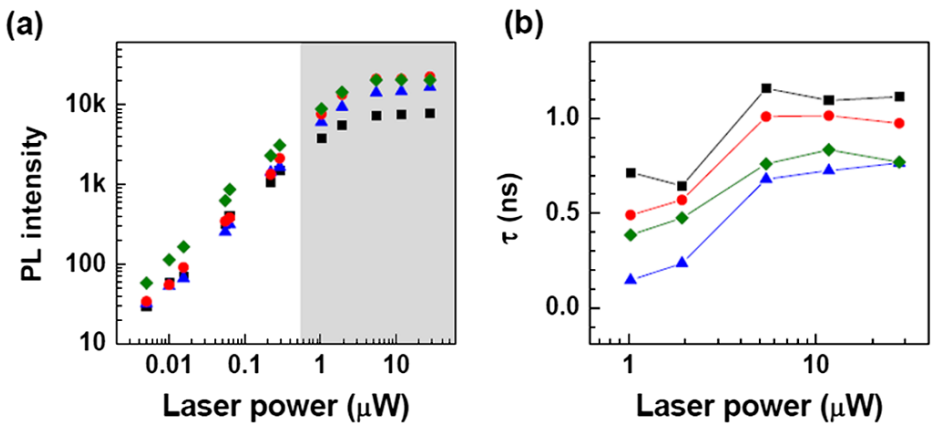

Figure 7.6: (a) Photoluminescence intensity of four QDs embedded within a photonic crystal cavity as a function of laser power. (b) Exciton lifetime for the same for QDs, extracted from LIA data.

simulations. The two are in excellent agreement. We see that our PL intensity has a linear dependence at low power, which we expect for excitons. At higher power, the QDs become saturated and the emission levels off. For the data in Figure 7.4, we were operating at 36μW, well within the saturation region.

To see how the cavity quality can effect the nonlinear dynamics of the system, we performed similar measurements in a higher quality cavity with Q=680. Data is shown in Figure 7.6 where we have the luminescence intensity and exciton lifetime as a function of incident laser power. The exciton lifetime is only determined above QD saturation powers. It is important to note that this cavity has saturation onset at much lower laser powers. This shows there is a correlation between cavity quality and photon density of states of these emitters.

We expect biexcitons to have similar dynamics to that of single excitons in regard to the cavity interaction at high power. Data is shown in Figure 7.7. There is a significant difference at low power. Here, we actually see an increase in emission near zero time delay. We suspect this is due to the fact that we can now create additional excitations from the second pulse that form biexcitons. Power dependence of this emission shows it scales as the second power of the laser power as expected. At high power we see the same dynamics as

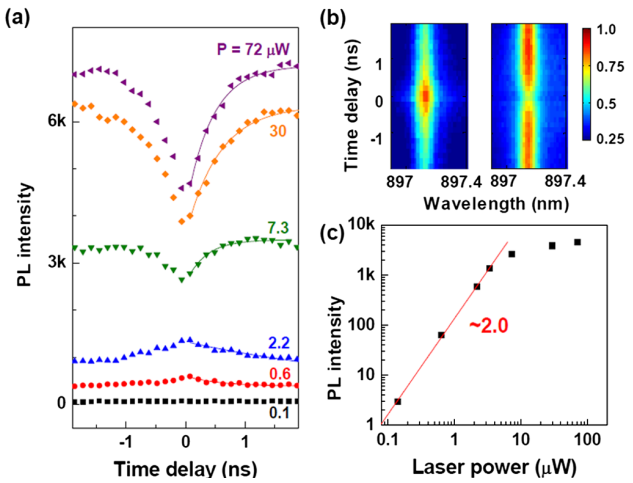

Figure 7.7: (a) Photoluminescence intensity as a function of pulse delay for biexciton peaks for various laser powers. (b) Intensity as a function of emission wavelength and time delay for the fixed path blocked and unblocked, respectively. (c) Biexciton intensity as a function of laser power.

those of single excitons.

Chapter 8

Summary and suggestions for future work

This work we have attempted to further our understanding of the physics of quantum dots and photonic crystal cavities. As is the case with many areas of academia, it has opened more doors for further investigation. We have two distinct main lines in our investigations – spatial placement of InAs/GaAs quantum dots and photonic crystal cavity optimizations. In each of these areas, there are exciting opportunities for further work. Ultimately, the combination of these two areas should lead to even more fruitful endeavors and hopefully open the door a little wider toward realization of a practical, scalable quantum computing platform.

8.1 Site controlled QD formation

We have demonstrated a FIB patterning technique for inducing InAs/GaAs quantum dot formation at specific locations while suppressing dot formation elsewhere [67]. By careful tuning of our patterning and epitaxial growth we have created square arrays with a single

quantum dot at every array site [46, 48]. Our FIB process shows potential for better spatial positioning over ex-situ techniques and optical homogeneity similar to other techniques [67, 46]. We have found a regime in which we can arbitrarily change the spacing between the quantum dot nucleation sites without affecting the dot growth and characterization. We have further shown through optical studies our ability to investigate a single quantum dot with spatial optical resolution near the diffraction limit [43, 44].

Our work demonstrated our ability to create layers of quantum dots with 100% single dot placement fidelity. However, we have not yet been able to optically characterize these dots. These may be created modifying the parameters of the capping process – the deposition rate, substrate temperature, and annealing time. For applications such as quantum computing, we wish to interact with a single dot placed at the center of a photonic crystal cavity. This will require a careful aligning of the FIB process to the electron beam lithography. Careful use of alignment markers may be required to complete this process. Further work is ongoing to establish the precise growth techniques necessary to form a single layer of spatially controlled, optically active quantum dots.

8.2 Photonic crystal cavity optimization

Our application of a new search algorithm has found non-intuitive photonic crystal cavity designs which have improved quality factors and mode volumes over traditional L3 cavities [68]. By moving the holes surrounding a cavity and changing their radii, we have a more concentrated electric field mode profile. Our final Q/V ratio shows nearly an order of magnitude improvement over existing designs. This demonstrates that shifting from more conventional approaches of cavity design toward advanced algorithms can provide new avenues of study with interesting results. Additionally, this work demonstrates the importance of considering all of the holes surrounding the cavity rather than only those along the cavity axis.

The gravitational search algorithm employed in this study has some limitations. By setting the initial boundaries of the parameter space we may introduce bias to the search. Further work should be done to determine how robust this solution is to changes to the initial parameter space. Additionally, other algorithms exist that could in principle replace the GSA in our study. Determining the best approach to this type of study could prove useful in further experiments.

Additionally, the work on our improved cavity designs has been theoretical. Prototyping and measuring the quality factor of the design must be completed to demonstrate its performance above standard designs. This work is currently in progress.

8.3 Coupling quantum dots and photonic crystal cavities

The combination of our two main areas of research is the most promising, yet least explored area of this work. We have demonstrated our ability to independently study our cavities and quantum dots. We have demonstrated a technique for studying QD exciton lifetimes using a simple experiment. We have further shown how the interaction of the two can affect the QD states [42].

The penultimate goal of this work would be to build an ultrahigh quality cavity around a prepositioned single quantum dot. To do this we must develop techniques to incorporate our FIB milling techniques and our lithographic alignment. We should then be able to use our improved cavity designs to demonstrate strong coupling between a single dot and our cavity. This could be performed using our spatially mapped photoluminescence and luminescence intensity autocorrelation experiments.

The longer range goals would be to place two or more quantum dots at different cavity antinodes and use the cavity mode to mediate interaction between the two. Once we have

established our ability to couple a single dot we can attempt this process. Coupling two QDs via a cavity mode could enable two quantum state interactions, one of the requirements for building a physical quantum computer [18].

Appendix A

FDTD simulations in meep

Here we describe the methodology used to simulate a photonic crystal cavity using the open source FDTD electromagnetic simulator, meep [53]. We demonstrate building an L3 photonic crystal cavity. Starting with our results from Section 4.4 we know that a TE mode with frequency $0.25c/a$ will not propagate in a thin slab of GaAs containing a hexagonal array of holes. To achieve reasonable results from an FDTD simulation we need at least 8 pixels per wavelength in the high dielectric material [34]. For GaAs with a permittivity of $\epsilon = 12.9$ the index of refraction is 3.59. The wavelength of interest in GaAs would therefore be $1.11a$.

$$\lambda_{\text{high}} = \frac{\lambda_0}{n} = \frac{c}{nf} = \frac{c}{(3.59)(0.25c/a)} = 1.11a \tag{A.1}$$

The spatial resolution in meep is set as the number of pixels per unit length, where the lattice constant a will be our unit length. For eight pixels per wavelength, the maximum pixel size is $1.11a/8 = 0.14a$. The minimum resolution we can use is 8 pixels per lattice constant, corresponding to a pixel size of $0.125a$. Higher resolutions will give more accurate results at a time cost that scales as $(\text{resolution})^4$, since we have three spatial dimensions and one temporal dimension.

To find the cavity mode parameters, we will first define the structure of the material.

We then create an electromagnetic pulse. After the pulse ends we monitor the electric field as some point in the material. We expect a cavity mode to exist as a sine wave with some decay. Since multiple modes may exist in the cavity, we model the electric field as a sum of multiple modes.

$$\mathbf{E}(\mathbf{r},t) = \mathbf{A}_1(\mathbf{r})e^{i(\omega_1+i\gamma_1)t} + \mathbf{A}_2(\mathbf{r})e^{i(\omega_2+i\gamma_2)t} + \cdots \tag{A.2}$$

Once we find a mode of interest we modify our initial pulse with a narrow bandwidth and run the simulation again. Provided a narrow enough pulse is chosen a single mode may be excited. When exciting a single mode on resonance we can evaluate the cavity most accurately.

A.1 Finding the cavity mode profile

Code in meep is written using a Scheme script [1]. Typically the code is written in a text file and executed via the command line. We begin our demonstration with setting the basic parameters for our simulation.

```
(reset-meep)
(define-param res 8)
(define-param edge-shift 0.15)
(define-param tdecay 300)
(define-param pad-holes 8)
(define-param pad-air 1.5)
(define-param eps-gaas 12.9)
(define-param hole-radius 0.3)
(define-param slab-thickness 0.6)
(define-param dpml 1)
(define-param fcen 0.25)
(define-param df 0.1)
(set! eps-averaging? false)
```

Most of these parameters should be self explanatory. The `edge-shift` parameter is to move the two holes adjacent to the cavity out by $0.15a$, as explained in Section 5.3. We also disable sub-pixel permittivity averaging (`eps-averaging`) for two reasons. First, we are attempting to get a general idea of the mode profile and frequency. Second, meep introduces numerical errors when it is enabled and maximal symmetry is exploited (as of version 1.2.1). We must now define the simulation space. We need it to be sufficiently large to encompass the cavity as well as our perfectly matched layer thickness. This we will need to double since there will be PML on both sides of each spatial dimension. We also locate our GaAs slab at the origin of the grid.

```
(define sx (+ 2 (* 2 pad-holes) (* 2 dpml)))
(define sy (+ (* (sin (/ pi 3)) 2 pad-holes) (* 2 dpml)))
(define sz (+ slab-thickness (* 2 pad-air) (* 2 dpml)))
(set! geometry-lattice (make lattice (size sx sy sz)))
(set! pml-layers (list (make pml (thickness dpml))))
(set-param! resolution res)
(set! geometry
   (list (make block
      (center 0 0 0)
      (size infinity infinity slab-thickness)
      (material (make dielectric (epsilon eps-gaas))))))
```

In this program any materials that overlap give priority to those listed last in the script. We can create our cavity by simply adding infinitely tall air cylinders through the GaAs slab. We exploit some built in functions of meep to make coding simpler.

```
(set! geometry (append geometry
   ; even rows above
   (geometric-objects-duplicates
      (vector3 0 (* 2 (sin (/ pi 3))) 0) 1 (/ pad-holes 2)
      (geometric-object-duplicates
         (vector3 -1 0 0) 0 (+ 2 (* 2 pad-holes))
         (make cylinder
```

```
         (center (+ 1 pad-holes) 0) (radius hole-radius)
         (height infinity) (material air))))
; even rows below
(geometric-objects-duplicates
   (vector3 0 (* 2 (sin (/ pi 3))) 0) (/ pad-holes -2) -1
      (geometric-object-duplicates
         (vector3 -1 0 0) 0 (+ 2 (* 2 pad-holes))
         (make cylinder
            (center (+ 1 pad-holes) 0) (radius hole-radius)
            (height infinity) (material air))))
; odd rows
(geometric-objects-duplicates
   (vector3 0 (* 2 (sin (/ pi 3))) 0) (/ pad-holes -2)
      (- (/ pad-holes 2) 1)
      (geometric-object-duplicates
         (vector3 -1 0 0) 0 (+ 1 (* 2 pad-holes))
         (make cylinder
            (center (+ pad-holes 0.5) (sin (/ pi 3))) (height infinity)
            (radius hole-radius) (material air))))
; middle row
(geometric-object-duplicates
   (vector3 -1 0 0) 0 (- pad-holes 2)
      (make cylinder
         (center -3 0 0) (radius hole-radius)
         (height infinity) (material air)))
(geometric-object-duplicates
   (vector3 1 0 0) 0 (- pad-holes 2)
      (make cylinder
         (center 3 0 0) (radius hole-radius)
         (height infinity) (material air)))
; the offset cells
(list
   (make cylinder
      (center (+ 2 edge-shift) 0 0) (radius hole-radius)
      (height infinity) (material air))
   (make cylinder
      (center (- -2 edge-shift) 0 0) (radius hole-radius)
      (height infinity) (material air)))))
```

A profile through $z = 0$ of our permittivity function can be seen in Figure A.1. We now create our sources. For this cavity we do not know what the mode will look like. If we were

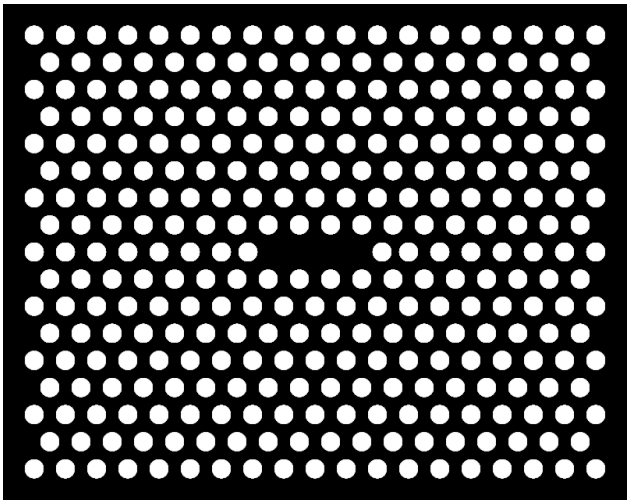

Figure A.1: Cavity permittivity profile.

to place an electromagnetic source or monitoring point at a cavity node, the response will not accurately depict the cavity's performance. The electric field would quickly decay into the crystal. We place both our source and monitoring point at positions of low symmetry since we expect nodes to exist along symmetry axes. We have the program output the electric field at the end of the simulation to locate the nodes and antinodes.

```
(set! sources (list (make source
   (src (make gaussian-src
      (frequency fcen) (fwidth df)))
      (component Ey) (center 1 1 0.2))))
(run-sources+ tdecay
   (at-beginning output-epsilon)
   (after-sources (harminv Ey (vector3 0.2 0.1 0.05) fcen df))
   (at-end output-efield-y))
```

This simulation gives two significant results. First, we can see the mode profile in Figure A.2 has its primary antinode at the center of the cavity (the origin of the simulation). There appears to be a tilt in the mode profile. This is an artifact of the location of our source and the low resolution used. Additionally our harmonic analysis of the electric field after the source has turned off reports the four modes listed in Table A.1.

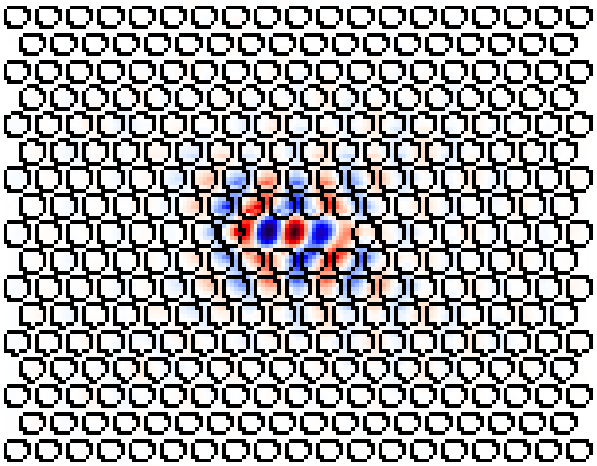

$f(c/a)$	Quality	Amplitude	Rel. error
0.250	-9861.09	0.113	1.55e-5
0.263	4565.01	0.020	6.82e-5
0.266	173.71	0.014	5.65e-4
0.286	1399.84	0.001	1.33e-4

Figure A.2 & Table A.1: L3 cavity mode profile and harmonic analysis. The initial pump pulse and field monitoring point were located at different points of low symmetry.

A.2 Isolating the cavity mode

Ideally we would determine just a single mode for our cavity. However we know from our previous experience in Chapter 4 with photonic band structures that multiple modes may exist. Additionally since we have run the simulation at such a low resolution it is possible that some of these are numerical artifacts and not actual cavity modes. The mode at $f = 0.25$ looks promising since it has the largest amplitude and lowest error. We can be reasonably certain this is a real mode. However the negative quality factor is not possible.

This can be attributed to the method in which we calculate the mode quality factor. The harmonic analysis package assumes that the electric field at the monitoring point can be decomposed into the sum of many sine waves multiplied by a decaying exponential and some amplitude. Hence the mode with the largest amplitude is *probably* the mode of interest. However since we have multiple modes interfering with each other constructively or destructively it is difficult to get an accurate value for the decay constant. This is partially due to our resolution and partially due to the length of time the system is allowed to decay for.

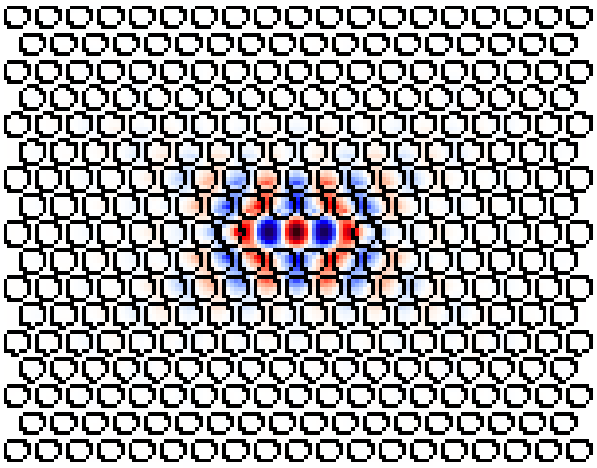

$f(c/a)$	Quality	Amplitude	Rel. error
0.226	115.57	0.002	2.56e-4
0.241	116.18	0.011	9.63e-6
0.250	45234.76	0.497	5.90e-8
0.286	1175.57	0.0449	2.00e-7

Figure A.3 & Table A.2: L3 cavity mode profile and harmonic analysis for initial pulse source located at the origin of the cavity.

Suppose you have a signal that is the combination of two sine waves with very similar frequencies. There would appear to be one sine wave with a superimposed beat frequency. A similar phenomena is occurring in this analysis but with much more complex waves. If the system does not run long enough there can not be a good fit to the data with our simple model. This can result in an inaccurate, sometimes negative measure of the decay constant. This is unphysical and it must be resolved in our subsequent simulations.

We move the source and harmonic analysis point to the origin, `(vector3 0 0 0)` and rerun the simulation. The mode calculation is much improved, as shown in Table A.2. At this point we wish to increase the resolution of the simulation to improve our results. Additionally we only wish to excite a single mode to get the best possible measure of the quality. To do this we will need to pump the cavity with a narrow band source. From Fourier analysis we expect a narrow frequency pump to rise and decay slowly. This will lead to a longer simulation time. For these reasons we exploit symmetry by adding a few lines in our script before the source.

```
(set! symmetries (list
   (make mirror-sym (direction X) (phase 1))
   (make mirror-sym (direction Z) (phase 1))
   (make mirror-sym (direction Y) (phase -1))))
```

The phase flip on the Y direction symmetry is due to the fact that we are using an E_y pulse. This means that the magnetic field will be in either the X or Z direction. Since the magnetic field is a pseudovector, it requires a phase flip under mirror symmetry [31]. With these additions we now excite only three modes at $f = 0.241, 0.250, 0.286$. The mode profile is also unchanged, which is an important consistency check for our symmetry additions. We now wish to excite only a single mode to prevent interference between the modes from contributing to error. By passing the script a narrower band using the command line code `df=0.01` we find that we only have one mode with frequency $f = 0.250c/a$, $Q = 55337$ and relative error 8.14e-13.

A.3 Increasing resolution to improve results

We increase the resolution of our simulation by 25% with simply passing the parameter `res=10` on the command line and find that the mode at $f = 0.25$ has shifted to $f = 0.262$. To determine the minimum resolution necessary to perform our simulations we perform the simulations at continually higher resolution until convergence is met. It is also important at each step to rerun the simulation shifting `fcen` so we excite on resonance.

As we found in the previous section, changing our initial pulse width significantly affected our final calculations. In Figure A.4 we show the calculated quality factor for the same crystal with differing pulse widths. This is performed for various resolutions. For all resolutions, the Q converges for $\delta f \leq 0.05c/a$. At larger pulse widths ($\delta f > 0.05c/a$) we get unphysical results due to the finite run time of the simulation. This sets our upper limit on δf we can use in our simulation and get meaningful results. Fortunately for all pulse widths the center

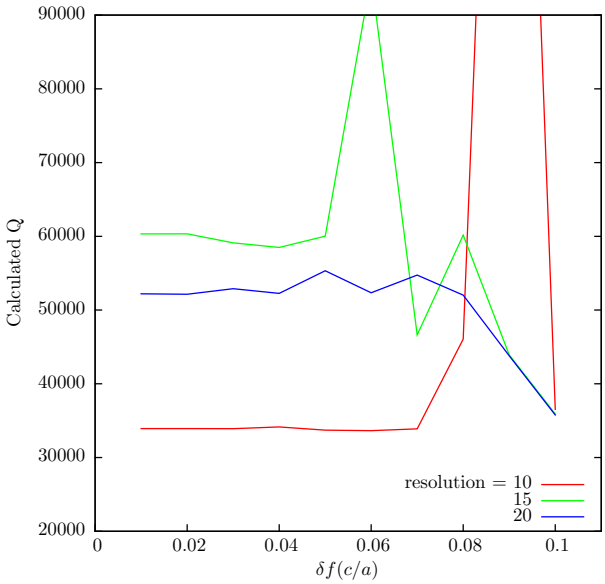

Figure A.4: Calculated quality factor as a function of pulse width.

frequency calculated does not shift. This allows the operator to use a broad source to locate the mode and immediately jump to a narrow source on resonance.

The final check to find the cavity parameters is to increase the resolution until convergence is met. Figure A.6 shows the final result of our simulation at a resolution of 40 pixels per lattice parameter. In Figure A.5 we show the calculated frequency and quality factor of the cavity. We see no general trend to the frequency calculation. However it is important to note that the calculated frequencies are all within 2% of one another. For the quality factor we find that resolutions of 20 pixels per lattice parameter or higher converge to within about 10%. In general, when performing the FDTD simulations it is helpful to double the resolution of your final result to ensure there are no significant differences. In most cases doing so will require exploitation of multiple processors or cores within one processor. In meep this can be performed using the MPI functionality [7].

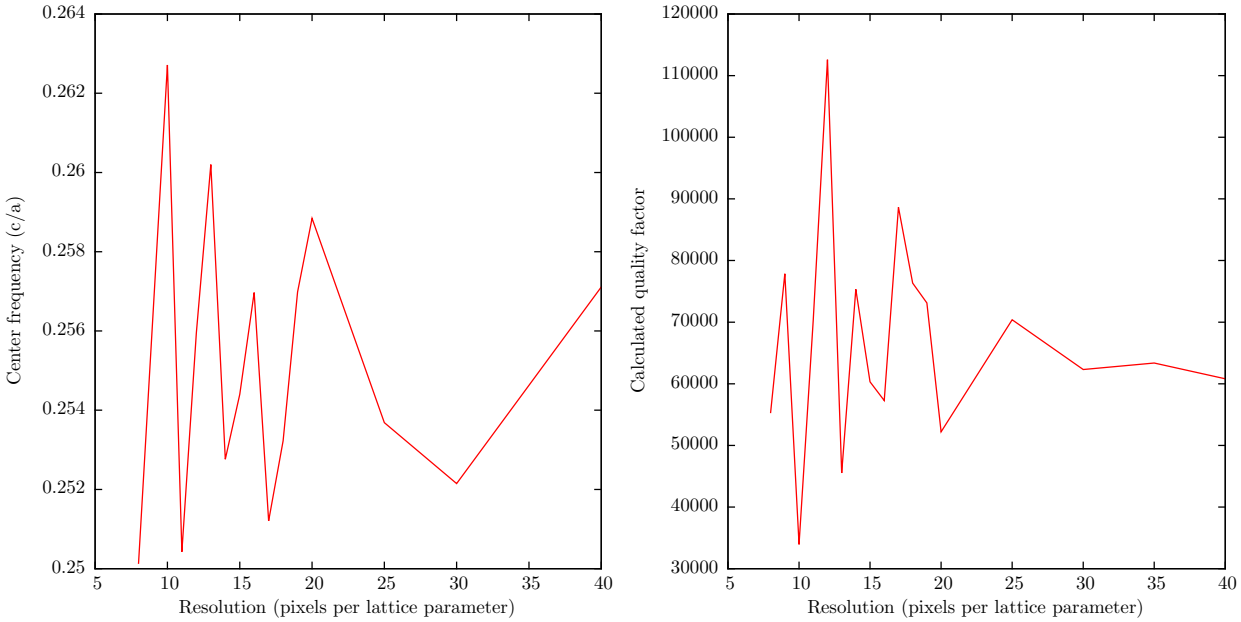

Figure A.5: Calculated cavity frequency and quality factor as a function of FDTD resolution.

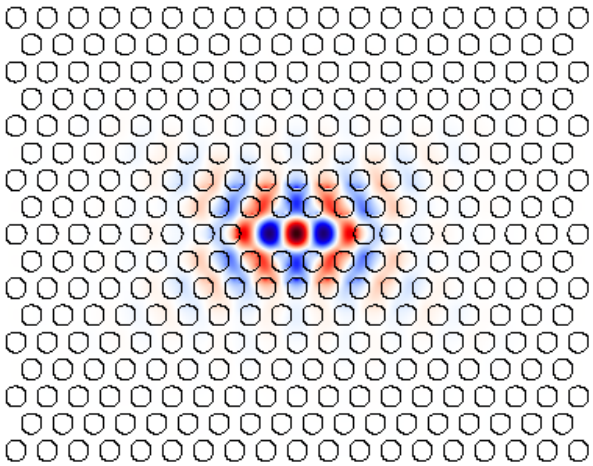

$f(c/a)$	Quality	Amplitude	Rel. error
0.259	52147	2.745	9.05e-11

Figure A.6 & Table A.3: Final L3 cavity mode profile and harmonic analysis high resolution, narrow input pulse simulation.

Appendix B

Controlling laboratory equipment

This appendix serves to aid future researchers in building or modifying software for controlling laboratory equipment. All code listed herein is written in the LabVIEW programming language. Design principles are based primarily on the LabVIEW Style Book [12].

The goal of our equipment control is to utilize all the resources necessary to complete an experiment in the most efficient method possible. For an experiment that will only be used one time, a very quick "just get the job done" approach is often best. However many times we find that certain equipment must be used in multiple experiments and in a variety of configurations. For these cases it would be best to write control software for the equipment in question once and then use a high level virtual instrument (VI) in our experiment. This ultimately simplifies the experiment's code and makes for a more easy to understand interface.

To do this we employ a server-client architecture. We expect both client and server to exist on the same computer. To move the client to a separate computer will take some expansion of the code. For our applications, the server provides a direct interface to the equipment in question. Then we have client VI's that interact with the server to manipulate the equipment. It is important that the client VI in no way directly interfaces with the equipment. This allows us to isolate problems/errors at the level of the hardware, server,

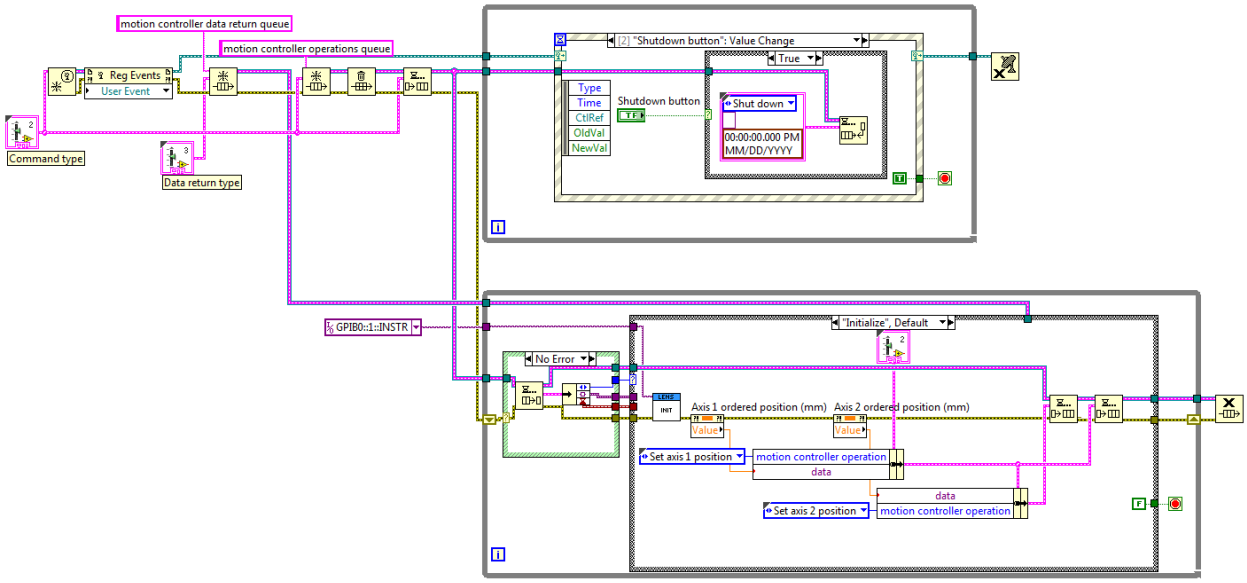

Figure B.1: Typical server architecture.

client VI, or experiment program.

B.1 Server layers of abstraction

When operating any equipment we wish to work at three levels of abstraction. The idea is to isolate what exactly we're trying to accomplish and confine that to a single layer. The application layer is the highest, which is where the user interacts with their program. Next lower is the component layer, where the logic of how to control the instrument lies. Below that is the instrument layer, where we actually interact with the equipment.

When implementing these abstraction layers, it is best to do so in a manner that visually relates to the code operation. In Figure B.1 there are clearly three main sections of code. On the top right section we have our event driven state machine that runs the user interface. The bottom right contains the component layer, which is implemented using a queued state machine. On the far left are startup procedures necessary for the program to execute correctly.

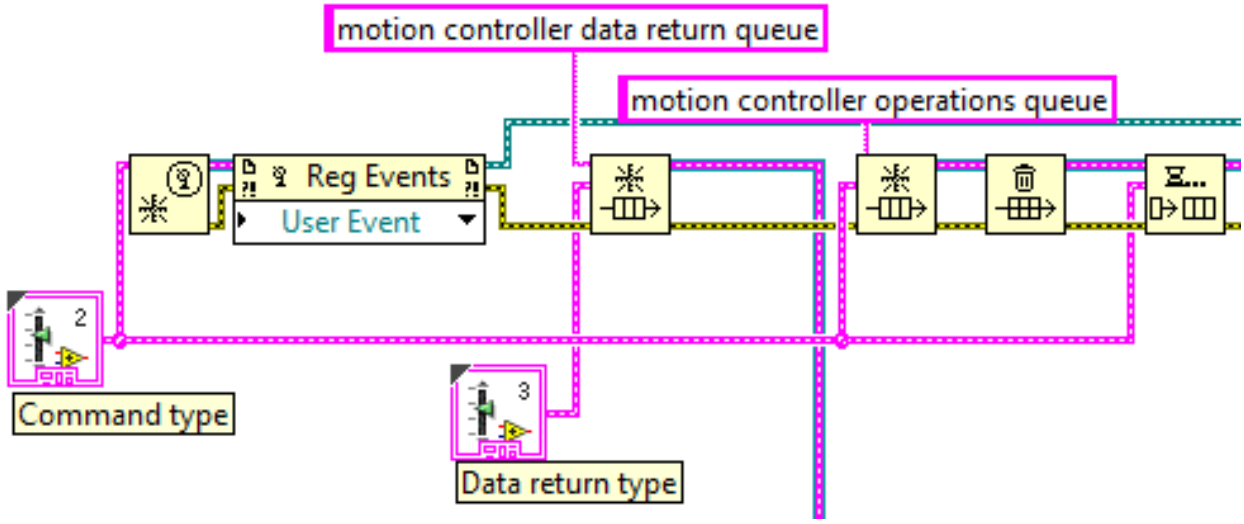

Figure B.2: Server startup routines.

The startup routines in Figure B.2 prepare both the application layer and component layer. First we create a user defined event structure. This will allow us to pass commands from the component layer to the application layer if necessary. Then we have two queues. The first is the data return queue. This is a cluster with a data component (void type) and timestamp. When an operation is completed by the component layer, this is where it will put the return data. The other queue is the command queue where we will tell the component layer to execute certain commands from a separate VI or from the front panel. This cluster contains a data component (void type also), timestamp, and an enumerated command. After initializing we flush the command queue and then pass it the initialization command. This structure is useful since any VI running on this same computer can access both the command and data queues, which we exploit later on.

B.1.1 Application layer

This is the level at which the user operates. It *always* includes the front panel(s) that the user interacts with. It may also include queues or other devices for interacting with client

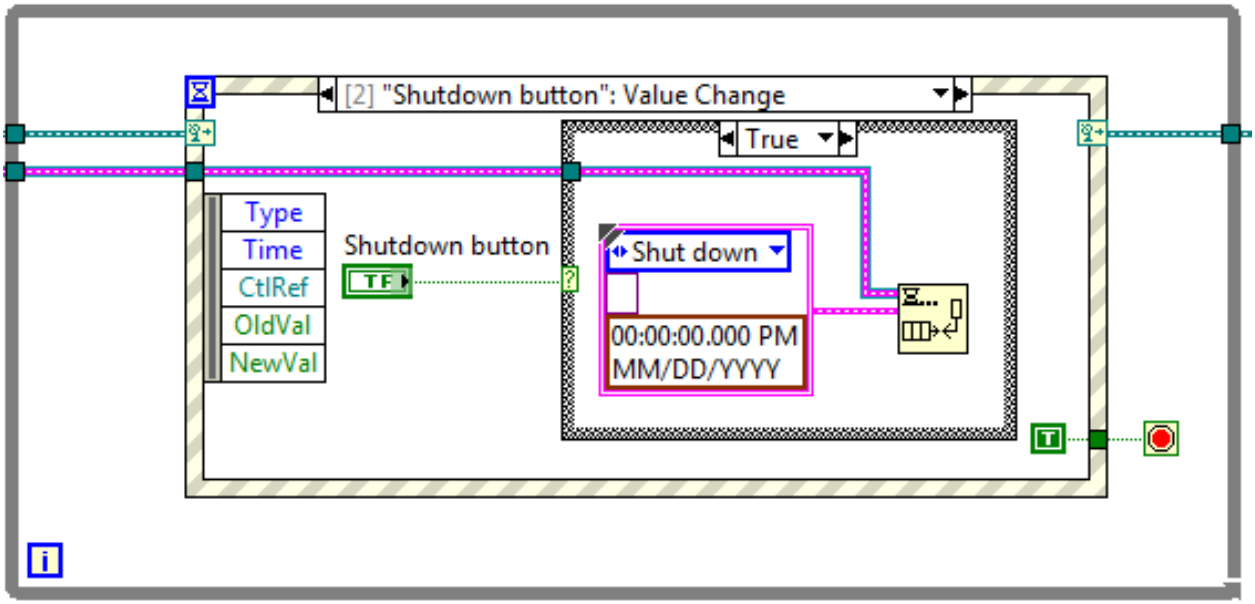

Figure B.3: Application layer event driven state machine.

programs. We consider client programs to be just another instance of a user interface (so far as the equipment's server is concerned). The application layer sends commands to the component layer about what the user intends to happen. In our server the application layer is typically an event driven state machine for the user interface and a queued state machine for receiving client commands.

Figure B.3 is one example of this architecture. When the user interacts with the front panel it will generate an event. This event tells the system to go into a specific "state." In this example pressing the "Shutdown button" causes the application layer to go into the state in which it sends a command to the component layer to shut down via the command queue. It then exits the outer while loop. In any other state the while loop is told to continue executing. One advantage of this setup is that the event structure uses minimal computer resources while waiting between events. When we have many different instruments operating simultaneously this can have huge time advantages over simpler methods.

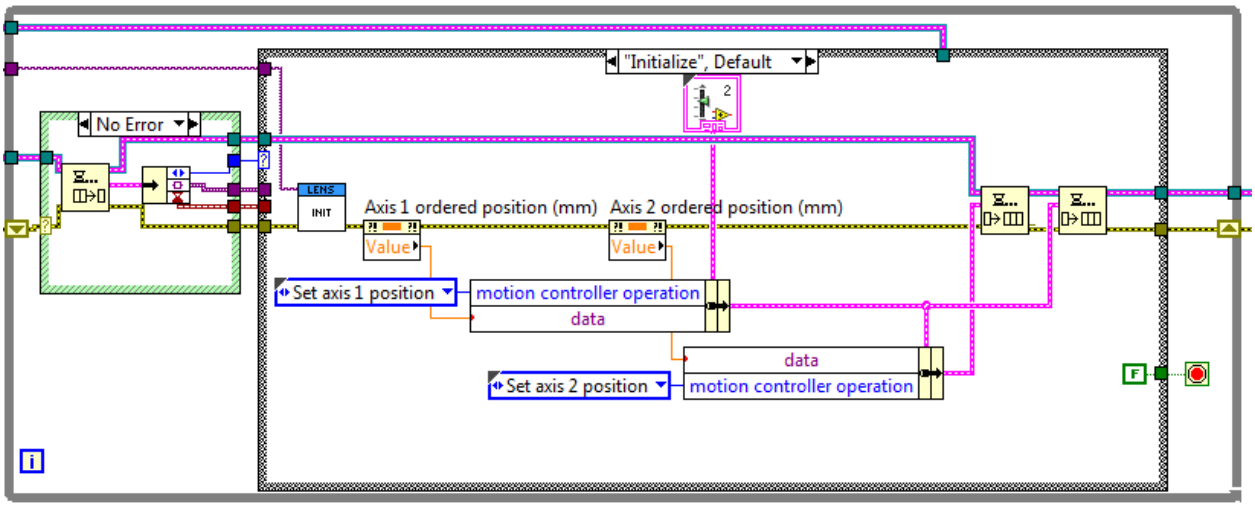

Figure B.4: Component layer queued state machine.

B.1.2 Component layer

The purpose of the component layer is to receive instructions from the application layer and send specific commands to the instrument layer. The component layer may be the most important layer because it contains *all* of the logic of the program. If we need to expand the server to include functionality, we must always consider how the different states of the equipment interact. For example, if we tell the server to store the data from the camera it needs to first decide if the camera is in single exposure or continuous exposure mode. That will determine if we need to open the shutter and take an exposure or just store data currently in the camera's circular buffer. The component layer performs its logic operations and then sends specific commands to the instrument via the instrument layer. In our server the component layer is typically a queued state machine.

In this example the while loop is fed two inputs, the command queue and a error cluster connected via shift register. This is extremely important because we want the program to shut down in case of an error in any state. So we first parse the error cluster. If no error exists, then we proceed to dequeue the next command. This will go into an idle state which again uses minimal computer resources much like the event driven state machine. Whenever

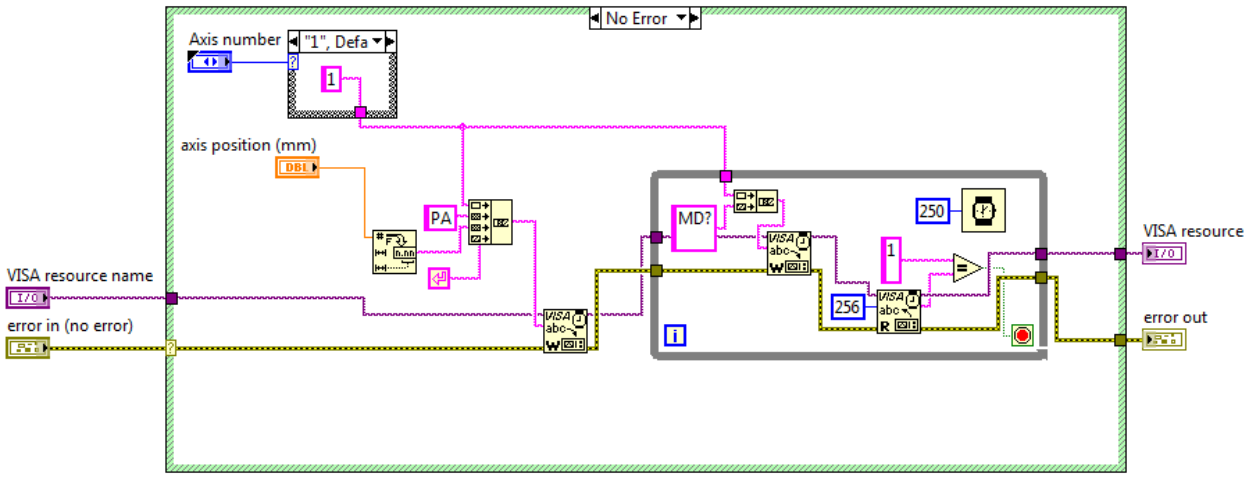

Figure B.5: Instrument layer sub-VI.

a command is put into the command queue, it is broken up into the command, the data, and a timestamp. Not all command states will require all of these inputs. For the example shown, there is no data needed for initialization. Likewise, we are not going to pass any data back via the data queue, so we do not use the timestamp. After performing the instrument level initialization (shown as a sub-VI labelled "INIT") we must apply the logic necessary to correctly operate this instrument. For example, after the hardware is initialized we want to tell it to go to the positions listed on the front panel. This is a simple matter of putting the command clusters into the command queue.

B.1.3 Instrument layer

The instrument layer contains the direct interaction with the equipment. These are very low level commands and may incorporate external libraries. This is typically done through sub-VI's from the main server.

When writing these sub-VI's our goal is to have a fully self contained program. It is best to always include error cluster inputs and outputs and to bypass all code execution if an error is fed into the VI. This is demonstrated as the case structure outlining the code in

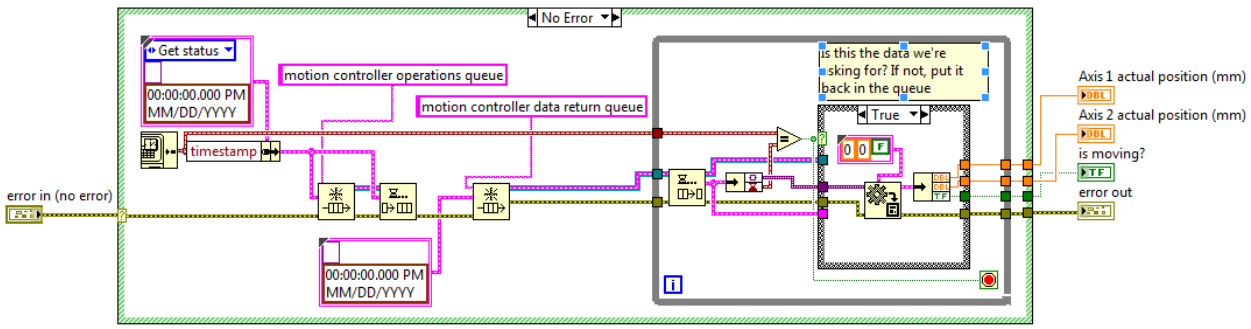

Figure B.6: Client VI interacting with server.

Figure B.5. The details of this code are relatively unimportant, since they are just specific commands for this instrument.

B.2 Client/Server interaction

Having developed the server in this efficient manner, the next task is to write very simple VI's that allow an overarching experiment's VI to interact with the server. The approach is to place the desired command into the command queue and then wait for data to be returned from the data queue, if appropriate. It is important to send in the computer's current time as a time stamp, since that will inform the server that data should be placed into the data queue. That is, if the timestamp is left at the default no data will be returned to prevent filling the data queue unnecessarily. Then we check the data queue for our time stamp. If the entry we find has our time stamp, we return the appropriate data. If not, we place it back into the end of the queue. This will repeat until the correct data has been found.

B.3 Experiment VIs

Having developed a server to control the underlying hardware and client VI's to interact with the server, we are now free to focus on the goal of the experiment. Here we should have a very easy to understand program that controls what data we want to collect and how

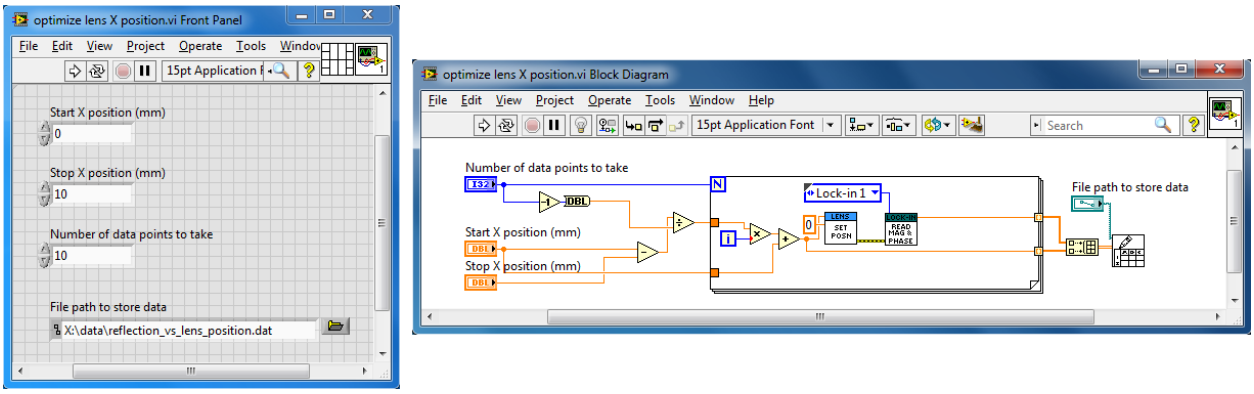

Figure B.7: Example experiment VI.

we wish to go about it. For example, suppose we have two instruments. We have a motor controller that moves a lens position and a lock-in amplifier that reads the electrical signal from a photodiode. We wish to design an experiment that will scan over the range of the lens position, read the corresponding signal from the lock in amplifier, and store the data. An example can be seen in Figure B.7. Following the goal of the experiment is very simple and the purpose of each part can be inferred easily.

Ideally all of the inputs for an experiment will correspond to the relevant parameter of interest. For example, instead of labeling an input as "Axis 1 position" it should be "X axis position." The subtle difference is that one version corresponds to the instrument and the other corresponds to the experiment. Similarly you may want a label such as "reflection intensity" instead of "lock-in X%." This makes it clear exactly what we are attempting to set/measure and has the underlying code convert that into instrument commands. The emphasis of the experiment VI should be the *experiment* not the instrumentation.

Bibliography

[1] H. Abelson, R. Dybvig, C. Haynes, G. Rozas, N. Adams, D. Friedman, E. Kohlbecker, G. Steele, D. Bartley, R. Halstead, D. Oxley, G. Sussman, G. Brooks, C. Hanson, K. Pitman, and M. Wand, *Revised report on the algorithmic language scheme*, Higher-Order and Symbolic Computation, 11 (1998), p. 7. doi:10.1023/A:1010051815785.

[2] Y. Akahane, T. Asano, B.-S. Song, and S. Noda, *Fine-tuned high-Q photonic-crystal nanocavity*, Opt. Express, 13 (2005), p. 1202. doi:10.1364/OPEX.13.001202.

[3] R. L. Anderson, *Germanium-gallium arsenide heterojunction*, IBM J. Res. Dev., 4 (1960), pp. 283–287. doi:10.1147/rd.43.0283.

[4] G. B. Arfken and H. J. Weber, *Mathematical Methods for Physicists*, Academic Press, 5th ed., 2001.

[5] P. Atkinson, S. Kiravittaya, M. Benyoucef, A. Rastelli, and O. G. Schmidt, *Site-controlled growth and luminescence of InAs quantum dots using* in situ *Ga-assisted deoxidation of patterned substrates*, Appl. Phys. Lett., 93 (2008), p. 101908. doi:10.1063/1.2980445.

[6] P. E. Barclay, K. Srinivasan, and O. Painter, *Design of photonic crystal waveguides for evanescent coupling to optical fiber tapers and integration with high-Q cavities*, J. Opt. Soc. Am. B, 20 (2003), p. 2274. doi:10.1364/JOSAB.20.002274.

[7] B. Barney, *Message passing interface (MPI)*. `https://computing.llnl.gov/tutorials/mpi/`, Aug. 2013.

[8] J.-P. Berenger, *A perfectly matched layer for the absorption of electromagnetic waves*, J. Comput. Physics, 114 (1994), p. 185. doi:10.1006/jcph.1994.1159.

[9] P. Bhattacharya, *Semiconductor Optoelectronic Devices*, Prentice Hall, 2nd ed., 1996.

[10] D. Bimberg, M. Grundmann, and N. N. Ledentsov, *Quantum Dot Heterostructures*, Wiley, 1999.

[11] D. Bimberg and U. W. Pohl, *Quantum dots: promises and accomplishments*, Mat. Today, 14 (2011), p. 388. doi:10.1016/S1369-7021(11)70183-3.

[12] P. A. Blume, *The LabVIEW Style Book*, Prentice Hall, 2007.

[13] B. W. Carroll and D. A. Ostlie, *An Introduction to Modern Astrophysics*, Addison-Wesley, 2nd ed., 2006.

[14] J. Claudon, J. Bleuse, N. S. Malik, M. Bazin, P. Jaffrennou, N. Gregersen, C. Sauvan, P. Lalanne, and J.-M. Gérard, *A highly efficient single-photon source based on a quantum dot in a photonic nanowire*, Nature Photonics, 4 (2010), p. 174. doi:10.1038/nphoton.2009.287.

[15] R. Coccioli, M. Boroditsky, K. W. Kim, Y. Rahmat-Samii, and E. Yablonovitch, *Smallest possible electromagnetic mode volume in a dielectric cavity*, IEE Proc. Optoelectron., 145 (1998). doi:10.1049/ip-opt:19982468.

[16] L. Cuadra, A. Martí, and A. Luque, *Type II broken band heterostructure quantum dot to obtain a material for the intermediate band solar cell*, Physica E, 14 (2002), p. 162. doi:10.1016/S1386-9477(02)00370-3.

[17] P. B. Deotare, M. W. McCutcheon, I. W. Frank, M. Khan, and M. Lončar, *High quality factor photonic crystal nanobeam cavities*, Appl. Phys. Lett., 94 (2009), p. 121106. doi:10.1063/1.3107263.

[18] D. P. DiVincenzo, *The physical implementation of quantum computation*, Fortschr. Phys., 48 (2000), p. 771. doi:10.1002/1521-3978(200009)48:9/11<771::AID-PROP771>3.0.CO;2-E.

[19] D. Englund, D. Fattal, E. Waks, G. Solomon, B. Zhang, T. Nakaoka, Y. Arakawa, Y. Yamamoto, and J. Vučković, *Controlling the spontaneous emission rate of single quantum dots in a two-dimensional photonic crystal*, Phys. Rev. Lett., 95 (2005), p. 013904. doi:10.1103/PhysRevLett.95.013904.

[20] ——, *Controlling the spontaneous emission rate of single quantum dots in a two-dimensional photonic crystal*, Phys. Rev. Lett., 95 (2005), p. 013904. doi:10.1103/PhysRevLett.95.013904.

[21] D. Englund, I. Fushman, and J. Vučković, *General recipe for designing photonic crystal cavities*, Opt. Express, 12 (2005), p. 5961. doi:10.1364/OPEX.13.005961.

[22] D. Englund, A. Majumdar, A. Faraon, M. Toishi, N. Stoltz, P. Petroff, and J. Vučković, *Resonant excitation of a quantum dot strongly coupled to a photonic crystal nanocavity*, Phys. Rev. Lett., 104 (2010), p. 073904. doi:10.1103/PhysRevLett.104.073904.

[23] M. Fox, *Optical properties of solids*, Oxford University Press, 2001.

[24] W. R. Frei, H. T. Johnson, and K. D. Choquette, *Optimization of a single defect photonic crystal laser cavity*, J. Appl. Phys., 103 (2008), p. 033102. doi:10.1063/1.2838173.

[25] P. Frigeri, L. Seravalli, G. Trevisi, and S. Franchi, *Comprehensive Semiconductor Science and Technology*, Elsevier Science, 2011.

[26] D. J. Griffiths, *Introduction to Quantum Mechanics*, Pearson Prentice Hall, 2nd ed., 2004.

[27] P. Harrison, *Quantum Wells, Wires and Dots: Theoretical and Computational Physics of Semiconductor Nanostructures*, John Wiley & Sons, Ltd., 2nd ed., 2005.

[28] K. Hennessy, A. Badolato, M. Winger, D. Gerace, M. Atatüre, S. Gulde, S. Fält, E. L. Hu, and A. Imamoğlu, *Quantum nature of a strongly coupled single quantum dotcavity system*, Nature, 445 (2007), p. 896. doi:10.1038/nature05586.

[29] K. Hoshino, A. Gopal, M. S. Glaz, D. A. V. Bout, and X. Zhang, *Nanoscale fluorescence imaging with quantum dot near-field electroluminescence*, Appl. Phys. Lett., 101 (2012). doi:10.1063/1.4739235.

[30] J. D. Jackson, *Classical Electrodynamics*, Wiley, 3rd ed., 1998.

[31] J. D. Joannopoulos, *Photonic Crystals*, Princeton University Press, 2nd ed., 2008.

[32] J. D. Joannopoulos, P. R. Villeneuve, and S. Fan, *Photonic crystals: putting a new twist on light*, Nature, 386 (1997), p. 143. doi:10.1038/386143a0.

[33] S. John, *Strong localization of photons in certain disordered dielectric superlattices*, Phys. Rev. Lett., 58 (1987), p. 2486. doi:10.1103/PhysRevLett.58.2486.

[34] S. Johnson, *Meep tutorial*. `http://ab-initio.mit.edu/wiki/index.php/Meep_Tutorial`, Aug. 2013.

[35] S. G. Johnson and J. D. Joannopoulos, *Block-iterative frequency-domain methods for Maxwell's equations in a planewave basis*, Opt. Express, 8 (2001), pp. 173–190. doi:10.1364/OE.8.000173.

[36] E. Kapon, M. Walther, J. Christen, M. Grundmann, C. Caneau, D. Hwang, E. Colas, R. Bhat, G. H. Song, and D. Bimberg, *Quantum wire heterostructure for optoelectronic applications*, Superlattice Microst., 12 (1992), p. 491. doi:10.1016/0749-6036(92)90307-Q.

[37] S. Kiravittaya, H. Heidemeyer, and O. G. Schmidt, *Growth of three-dimensional quantum dot crystals on patterned GaAs (001) substrates*, Physica E, 23 (2004), p. 253. doi:10.1016/j.physe.2003.10.013.

[38] C. Kittel, *Introduction to Solid State Physics*, Wiley, 8th ed., 2004.

[39] Y. Kobayashi and K. Yamaguchi, *Control of photoluminescence wavelength from uniform InAs quantum dots by annealing*, Appl. Surf. Sci., 244 (2005), p. 88. doi:10.1016/j.apsusc.2004.09.131.

[40] E. C. Le Ru, J. Fack, and R. Murray, *Temperature and excitation density dependence of the photoluminescence from annealed InAs/GaAs quantum dots*, Phys. Rev. B, 67 (2003), p. 245318. doi:10.1103/PhysRevB.67.245318.

[41] N. N. Ledentsov, V. M. Ustinov, V. A. Shchukin, P. S. Kop'ev, Z. I. Alferov, and D. Bimberg, *Quantum dot heterostructures: Fabrication, properties, lasers*, Semiconductors, 32 (1998), p. 343. doi:10.1134/1.1187396.

[42] J. Lee, T. W. Saucer, A. J. Martin, J. M. Millunchick, and V. Sih, *Time-resolved two-pulse excitation of quantum dots coupled to a photonic crystal cavity in the purcell regime*, Phys. Rev. Lett., 110 (2013), p. 013602. doi:10.1103/PhysRevLett.110.013602.

[43] J. E. Lee, T. W. Saucer, A. J. Martin, D. Tien, J. M. Millunchick, and V. Sih, *Photoluminescence imaging of focused ion beam induced individual quantum dots*, Nano Lett., 11 (2011), p. 1040. doi:10.1021/nl1038902.

[44] ——, *Ground-state exciton emission of InAs quantum dots produced by focused-ion-beam-directed nucleation*, J. Lumin., 133 (2013), p. 117. doi:10.1016/j.jlumin.2011.10.008.

[45] J. Y. Lee, M. J. Noordhoek, P. Smereka, H. McKay, and J. M. Millunchick, *Filling of hole arrays with InAs quantum dots*, Nanotechnology, 20 (2009), p. 285305. doi:10.1088/0957-4484/20/28/285305.

[46] M. Luengo-Kovac, T. W. Saucer, A. J. Martin, J. M. Millunchick, and V. Sih, *Analyzing pattern retention for multilayer focused ion beam induced quantum dot structures*, J. Vac. Sci. Technol. B, 31 (2013), p. 031208. doi:10.1116/1.4804278.

[47] A. Luque and A. Martí, *Increasing the efficiency of ideal solar cells by photon induced transitions at intermediate levels*, Phys. Rev. Lett., 78 (1997), p. 5014. doi:10.1103/PhysRevLett.78.5014.

[48] A. J. Martin, T. W. Saucer, G. V. Rodriguez, V. Sih, and J. M. Millunchick, *Lateral patterning of multilayer InAs/GaAs(001) quantum dot structures by* in vacuo *focused ion beam*, Nanotechnology, 23 (2012), p. 135401. doi:10.1088/0957-4484/23/13/135401.

[49] A. J. Martin, T. W. Saucer, V. Sih, and J. M. Millunchick, *Effects of predetermined lateral separation on quantum dot size and dissolution*, Appl. Phys. Lett., 102 (2013), p. 182105. doi:10.1063/1.4804605.

[50] A. J. Martin, T. W. Saucer, K. Sun, S. J. Kim, G. Ran, G. V. Rodriguez, X. Pan, V. Sih, and J. Millunchick, *Analysis of defect-free GaSb/GaAs*(001) *quantum dots grown on the Sb-terminated* (2×8) *surface*, J. Vac. Sci. Technol. B, 30 (2012), p. 02B112. doi:10.1116/1.3675455.

[51] M. Mashita, T. Numata, H. Nakazawa, Y. Kajikawa, B.-H. Koo, H. Makino, and T. Yao, *Photoluminescence from ultrathin InAs/GaAs single quantum wells grown on GaAs (111)A substrates*, Jpn. J. Appl. Phys., 42 (2003), p. L807. doi:10.1143/jjap.42.l807.

[52] B. G. Orr, D. Kessler, C. W. Snyder, and L. Sander, *A model for strain-induced roughening and coherent island growth*, Europhys. Lett., 19 (1992), p. 33. doi:10.1209/0295-5075/19/1/006.

[53] A. F. Oskooi, D. Roundy, M. Ibanescu, P. Bermel, J. D. Joannopoulos, and S. G. Johnson, *MEEP: A flexible free-software package for electromagnetic simulations by the FDTD method*, Comput. Phys. Commun., 181 (2010), pp. 687–702. doi:10.1016/j.cpc.2009.11.008.

[54] K. Oura, V. G. Lifshits, A. A. Saranin, A. V. Zotov, and M. Katayama, *Surface Science: An Introduction*, Springer, 2003.

[55] J. Pamulapati, P. K. Bhattacharya, J. Singh, P. R. Berger, C. W. Snyder, B. G. Orr, and R. L. Tober, *Realization of in-situ sub two-dimensional quantum structures by strained layer growth phenomena in the* $In_xGa_{1-x}as/gaas$ *system*, J Electron. Mat., 25 (1996), p. 479. doi:10.1007/BF02666623.

[56] R. Paschotta, *Encyclopedia of Laser Physics and Technology*, John Wiley & Sons, Inc., 2008.

[57] F. Patella, F. Arciprete, M. Fanfoni, A. Balzarotti, and E. Placidi, *Apparent critical thickness versus temperature for InAs quantum dot growth on GaAs(001)*, Appl. Phys. Lett., 88 (2006), p. 161903. doi:10.1063/1.2189915.

[58] J. B. Pawley, *Handbook of biological confocal microscopy*, Plenum Press, revised ed. ed., 1990.

[59] A. Pimpinelli and J. Villain, *Physics of Crystal Growth*, Cambridge University Press, 1999.

[60] S. L. Portalupi, M. Galli, C. Reardon, T. F. Krauss, L. OFaolain, L. C. Andreani, and D. Gerace, *Planar photonic crystal cavities with far-field optimization for high coupling efficiency and quality factor*, Opt. Express, 18 (2010), p. 16064. doi:10.1364/OE.18.016064.

[61] D. Press, S. Götzinger, S. Reitzenstein, C. Hofmann, A. Lofer, M. Kamp, A. Forchel, and Y. Yamamoto, *Photon antibunching from a single quantum-dot-microcavity system in the strong coupling regime*, Phys. Rev. Lett., 98 (2007), p. 117402. doi:10.1103/PhysRevLett.98.117402.

[62] E. Rashedi, H. Nezamabadipour, and S. Saryazdi, *GSA: A gravitational search algorithm*, Info. Science, 179 (2009), p. 2232. doi:10.1016/j.ins.2009.03.004.

[63] K. Rivoire, S. Buckley, and J. Vučković, *Multiply resonant photonic crystal nanocavities for nonlinear frequency conversion*, Opt. Express, 19 (2011), p. 2198. doi:10.1364/OE.19.022198.

[64] P. Russell, *Photonic crystal fibers*, Science, 299 (2003), p. 358. doi:10.1126/science.1079280.

[65] S. Russell and P. Norvig, *Artificial Intelligence: A Modern Approach*, Prentice Hall, 3rd ed., 2009.

[66] K. Sakoda, *Optical Properties of Photonic Crystals*, Springer, 2nd ed., 2005.

[67] T. W. Saucer, J. E. Lee, A. J. Martin, D. Tien, J. M. Millunchick, and V. Sih, *Photoluminescence of patterned arrays of vertically stacked InAs/GaAs quantum dots*, Solid State Commun., 151 (2011), pp. 269–271. doi:10.1016/j.ssc.2010.12.020.

[68] T. W. Saucer and V. Sih, *Optimizing nanophotonic cavity designs with the gravitational search algorithm*, Opt. Express, 18 (2013), p. 20831. doi:10.1364/OE.21.020831.

[69] C. Schneider, M. Strauss, T. Sünner, A. Huggenberger, D. Wiener, S. Reitzenstein, M. Kamp, S. Höfling, and A. Forchel, *Lithographic alignment to site-controlled quantum dots for device integration*, Appl. Phys. Lett., 92 (2008), p. 183101. doi:10.1063/1.2920189.

[70] T. Schwarz-Selinger, Y. L. Foo, D. G. Cahill, and J. E. Greene, *Surface mass transport and island nucleation during growth of ge on laser textured Si(001)*, Phys. Rev. B, 53 (2002), p. 125317. doi:10.1103/PhysRevB.65.125317.

[71] C. J. R. Sheppard, *Approximate calculation of the reflection coefficient from a stratified medium*, Pure Appl. Opt., 4 (1995), p. 664. doi:10.1088/0963-9659/4/5/018.

[72] K. Srinivasan, P. E. Barclay, and O. Painter, *Fabrication-tolerant high quality factor photonic crystal microcavities*, Opt. Express, 12 (2004), p. 1458. doi:10.1364/OPEX.12.001458.

[73] S. Tonomura and K. Yamaguchi, *Uniform formation of high-density InAs quantum dots by InGaAs capping growth*, J. Appl. Phys., 104 (2008), p. 054909. doi:10.1063/1.2975366.

[74] J. Vaillancourt, P. Vasinajindakaw, and X. Ju, *A high operating temperature (HOT) middle ave infrared (MWIR) quantum-dot photodetector*, Opt. Photonic Lett., 4 (2011), p. 57. doi:10.1142/S1793528811000196.

[75] J. Vučković, M. Lončar, H. Mabuchi, and A. Scherer, *Design of photonic crystal microcavities for cavity QED*, Phys. Rev. E, 65 (2001), p. 016608. doi:10.1103/PhysRevE.65.016608.

[76] M. A. Wallingemail, J. A. Novakemail, and J. R. E. Shepard, *Quantum dots for live cell and* in vivo *imaging*, Int. J. Mol. Sci., 10 (2009), p. 441. doi:10.3390/ijms10020441.

[77] E. Yablonovitch, *Inhibited spontaneous emission in solid-state physics and electronics*, Phys. Rev. Lett., 58 (1987), p. 2059. doi:10.1103/PhysRevLett.58.2059.

[78] T. Yoshie, A. Scherer, J. Hendrickson, G. Khitrova, H. M. Gibbs, G. Rupper, C. Ell, O. B. Shchekin, and D. G. Deppe, *Vacuum rabi splitting with a single quantum dot in a photonic crystal nanocavity*, Nature, 432 (2004), p. 200. doi:10.1038/nature03119.

[79] D. K. Young, L. Zhang, D. D. Awschalom, and E. L. Hu, *Coherent coupling dynamics in a quantum-dot microdisk laser*, Phys. Rev. B, 66 (2002), p. 081307(R). doi:10.1103/PhysRevB.66.081307.

[80] B. V. Zeghbroeck, *Principles of Semiconductor Devices*, Colorado University, 2006.